How much inundation occurs in the Amazon River basin?

Ayan Santos Fleischmann, Fabrice Papa, Alice César Fassoni-Andrade, John Melack, Sly Wongchuig, Rodrigo Cauduro Dias Paiva, Stephen K. Hamilton, Etienne Fluet-Chouinard, Rafael Barbedo, Filipe Aires, et al.

Accepted refereed manuscript of: Fleischmann AS, Papa F, Fassoni-Andrade A, Melack JM, Wongchuig S, Paiva RCD, Hamilton SK, Fluet-Chouinard E, Barbedo R, Aires F, Al Bitar A, Bonnet M, Coe M, Ferreira-Ferreira J & Silva TSF (2022) How much inundation occurs in the Amazon River basin?. *Remote Sensing of Environment*, 278, Art. No.: 113099.
https://doi.org/10.1016/j.rse.2022.113099

How much inundation occurs in the Amazon River basin?

Ayan Santos Fleischmann[1,2], Fabrice Papa[3,4], Alice Fassoni-Andrade[3,4], John M. Melack[5], Sly Wongchuig[6], Rodrigo Cauduro Dias de Paiva[2], Stephen K. Hamilton[7], Etienne Fluet-Chouinard[8], Rafael Barbedo[2], Filipe Aires[9], Ahmad Al Bitar[10], Marie-Paule Bonnet[11], Michael Coe[12], Jefferson Ferreira-Ferreira[1], Laura Hess[5], Katherine Jensen[13,14], Kyle McDonald[13,14], Alex Ovando[15], Edward Park[16], Marie Parrens[17,18], Sébastien Pinel[19], Catherine Prigent[20], Angélica F. Resende[21], Menaka Revel[22], Ake Rosenqvist[23], Jessica Rosenqvist[23], Conrado Rudorff[15], Thiago S. F. Silva[24], Dai Yamazaki[22], Walter Collischonn[2]

1 Mamirauá Institute for Sustainable Development, Tefé, AM, Brazil

2 Institute of Hydraulic Research, Universidade Federal do Rio Grande do Sul (UFRGS), Porto Alegre, RS, Brazil

3 Laboratoire d'Etudes en Géophysique et Océanographie Spatiales (LEGOS), Université de Toulouse, IRD, CNRS, CNES, USP, Toulouse, France

4 Institut de Recherche pour le Développement (IRD), Universidade de Brasília (UnB), Institute of Geosciences, Campus Universitário Darcy Ribeiro, 70910-900, Brasilia, Brazil

5 Earth Research Institute, University of California, Santa Barbara

6 Univ. Grenoble Alpes, IRD, CNRS, Grenoble INP, Institut des Géosciences de l'Environnement (IGE, UMR 5001), 38000, Grenoble, France

7 Kellogg Biological Station, Michigan State University, Hickory Corners, MI 49060, USA and Cary Institute of Ecosystem Studies, Millbrook, NY 12545 USA

8 Department of Earth System Science, Stanford University, Stanford, California, CA

9 Laboratoire d'Etudes du Rayonnement et de la Matière en Astrophysique et Atmosphères, Observatoire de Paris, UMR 8112, Paris, France.

10 Centre d'Etudes Spatiales de la Biosphère (CESBIO), Toulouse University (CNES, CNRS, INRAe, IRD, UPS), Toulouse, France

11 Espace-DEV, Univ Montpellier, Institute of Research for Development, Univ Guyane, Univ Reunion, Montpellier, France

12 Woodwell Climate Research Center, Falmouth, MA

13 Department of Earth and Atmospheric Sciences, City College of New York, City University of New York, New York, NY 10031, USA

14 Department of Earth and Environmental Science, The Graduate Center, City University of New York, New York, NY 10031, USA

[15] Centro Nacional de Monitoramento de Desastres Naturais (CEMADEN), São José dos Campos, São Paulo, Brazil

[16] National Institute of Education, Earth Observatory of Singapore and Asian School of the Environment, Nanyang Technological University, Singapore

[17] Centre d'Etudes Spatiales de la Bioshpère (CESBIO), CNES, Université de Toulouse (UPS), France

[18] Dynafor, Université de Toulouse, INRAE, INPT, INP-PURPAN, Castanet-Tolosan, France

[19] CEFREM, University of Perpignan Via Domitia, Perpignan, France

[20] CNRS, Sorbonne Université, Observatoire de Paris, Université PSL, Lerma, Paris, France

[21] Universidade de São Paulo, Departamento de Ciências Florestais (ESALQ), Piracicaba, SP, Brazil

[22] Institute of Industrial Science, The University of Tokyo, Tokyo, Japan.

[23] solo Earth Observation (soloEO), Tokyo 104-0054, Japan

[24] Biological and Environmental Sciences, Faculty of Natural Sciences, University of Stirling, Stirling, UK Fk9 4LA.

Corresponding author: Ayan Santos Fleischmann (ayan.fleischmann@gmail.com)

Abstract

The Amazon River basin harbors some of the world's largest wetland complexes, which are of major importance for biodiversity, the water cycle and climate, and human activities. Accurate estimates of inundation extent and its variations across spatial and temporal scales are therefore fundamental to understand and manage the basin's resources. More than fifty inundation estimates have been generated for this region, yet major differences exist among the datasets, and a comprehensive assessment of them is lacking. Here we present an intercomparison of 29 inundation datasets for the Amazon basin, based on remote sensing only, hydrological modeling, or multi-source datasets, with 18 covering the lowland Amazon basin (elevation < 500 m, which includes most Amazon wetlands), and 11 covering individual wetland complexes (subregional datasets). Spatial resolutions range from 12.5 m to 25 km, and temporal resolution from static to monthly, spanning up to a few decades. Overall, 31% of the lowland basin is

estimated as subject to inundation by at least one dataset. The long-term maximum inundated area across the lowland basin is estimated at 599,700 ± 81,800 km² if considering the three higher quality SAR-based datasets, and 490,300 ± 204,800 km² if considering all 18 datasets. However, even the highest resolution SAR-based dataset underestimates the maximum values for individual wetland complexes, suggesting a basin-scale underestimation of ~10%. The minimum inundation extent shows greater disagreements among datasets than the maximum extent: 139,300 ± 127,800 km² for SAR-based ones and 112,392 ± 79,300 km² for all datasets. Discrepancies arise from differences among sensors, time periods, dates of acquisition, spatial resolution, and data processing algorithms. The median total area subject to inundation in medium to large river floodplains (drainage area > 1,000 km²) is 323,700 km². The highest spatial agreement is observed for floodplains dominated by open water such as along the lower Amazon River, whereas intermediate agreement is found along major vegetated floodplains fringing larger rivers (e.g., Amazon mainstem floodplain). Especially large disagreements exist among estimates for interfluvial wetlands (Llanos de Moxos, Pacaya-Samiria, Negro, Roraima), where inundation tends to be shallower and more variable in time. Our data intercomparison helps identify the current major knowledge gaps regarding inundation mapping in the Amazon and their implications for multiple applications. In the context of forthcoming hydrology-oriented satellite missions, we make recommendations for future developments of inundation estimates in the Amazon and present a WebGIS application (https://amazon-inundation.herokuapp.com/) we developed to provide user-friendly visualization and data acquisition of current Amazon inundation datasets.

Key words: flooding, surface water, floodplains, interfluvial wetlands

1. Introduction

Aquatic ecosystems cover extensive areas of the Amazon basin, and are associated with temporally and spatially dynamic habitats such as floodable forests, savannas, grasslands, large and small rivers, and lakes (Hess et al., 2015; Junk et al., 2011; Melack and Coe, 2021; Reis et al., 2019a). These systems, hereafter called wetlands, support plants and animals that are adapted to the flood pulse (Junk et al., 1989), play key roles in regional and global biogeochemical cycles, especially the carbon cycle (Richey et al 1990; Dunne et al., 1998; Abril et al., 2014; Melack et al., 2004; Pangala et al., 2017; Martínez-Espinosa et al., 2020), and regulate the riverine transport of dissolved and particulate material, including sediment and organic matter (Armijos et al., 2020; Fassoni-Andrade and Paiva, 2019; Melack and Forsberg, 2001; Ward et al., 2017). Additionally, human settlements along Amazon wetlands (Blatrix et al., 2018; Denevan, 1996) benefit from ecosystem services, including food provision from native plants and animals as well as crop and livestock production (Coomes et al., 2016; Jardim et al., 2020).

Many of the wetlands of the Amazon basin are considered floodplain because they are subject to seasonal or periodic inundation by river overflow (i.e., the flood pulse; Junk et al., 1989). The region also hosts large interfluvial wetlands, which unlike fringing floodplains along large rivers, are flooded mainly by local rainfall and runoff and characterized by shallow water (Belger et al., 2011; Bourrel et al., 2009; Junk et al., 2011). Water sources, inundation patterns, and geomorphology interact to determine the structure and function of these biodiverse ecosystems (Junk et al., 2011; Latrubesse, 2012; Park and Latrubesse, 2017).

The extent of inundated land (also called flooded land or surface water extent), and its temporal variation, are core variables to understand wetland processes and are of interest for multiple scientific disciplines, including ecology (Silva et al., 2013; Hawes et al., 2012; Luize et al. 2015), land-atmosphere interactions (Prigent et al., 2011; Santos et al., 2019; Taylor et al., 2018), carbon

cycling and greenhouse gas emissions (Guilhen et al., 2020; Melack et al., 2004; Richey et al., 2002), and natural hazard management (Restrepo et al., 2020; Trigg et al., 2016). The Amazon basin has been a focus for remote sensing developments and applications in hydrology (Fassoni-Andrade et al., 2021), especially for inundation estimation, given the basin's large scale and global environmental relevance, relatively pristine landscape, and technical challenges posed by persistent cloud cover (Asner, 2001) and dense vegetation. This resulted in the development of more than 50 inundation maps and datasets for this region in recent decades. Tables 1 (datasets used in this study) and S1 (datasets not used due to redundancy or unavailability) summarize most of the datasets developed for mapping inundation in the Amazon basin.

Digital wetland maps were first produced for the Amazon basin by Matthews and Fung (1987) from aeronautical charts. Optical remote sensing systems in the visible or thermal spectral range, such as Landsat, are of limited value for most Amazon wetlands, since inundation under persistent cloud cover and dense vegetation canopies can be difficult to detect. Because of this, microwave systems have been employed. Large-scale inundation mapping was pioneered in the region through analysis of Scanning Multi-channel Microwave Radiometer (SMMR) and Special Sensor Microwave/Imager (SSM/I) passive microwave observations, which provided all-weather capability and sensitivity to inundation even in the presence of partial vegetative cover (Hamilton et al., 2002; Prigent et al., 2001; Sippel et al., 1998). Meanwhile, research demonstrated the all-weather capability and superior spatial resolution of synthetic aperture radar (SAR) systems. L-band SAR that can penetrate forest canopies and reveal underlying water through the "double bounce" effect was shown to be promising for mapping inundation in the Amazon (Hess et al., 2003). More specifically, the high-resolution, dual-season classification of the Japanese Earth Resources Satellite-1 (JERS-1) L-band SAR data for the entire lowland Amazon basin by Hess et

al. (2015), validated with airborne videography images, has been used as a benchmark for the inundation extent of Amazon wetlands. Since these initial studies, and with the availability of other imagery (e.g., Advanced Land Observing Satellite (ALOS) 1 and 2 missions), the remote sensing community seeking to map and characterize inundation employed various combinations of active and passive microwave data to benefit from the higher spatial resolution of the former and the higher temporal resolution of the latter (Aires et al., 2013; Jensen and McDonald, 2019; Papa et al., 2010; Parrens et al., 2019, 2017; Prigent et al., 2007, 2020; Schroeder et al., 2015).

Besides the basin-scale mappings (which, in our context, refer to both basin-scale datasets and those that cover only the lowland areas below 500 m.a.s.l. elevation) of annual maximum and minimum inundation (Chapman et al., 2015; Hess et al., 2015; Rosenqvist et al., 2020), dynamic datasets with high spatial and temporal resolution are mainly based on satellite passive microwave observations of coarse spatial resolution (Global Inundation Extent Multi-Satellite – GIEMS), Surface Water Microwave Product Series (SWAMPS), Surface Water Fraction (SWAF), Wetland Area and Dynamics for Methane Modeling (WAD2M) datasets; see Table 1), which can be downscaled using ancillary data (Aires et al., 2017, 2013; Parrens et al., 2019). Basin-scale, dynamic inundation estimates based on the ALOS satellite are limited given its low temporal resolution (repeat cycle of 46 days). Thus, some studies have analyzed time series of ALOS-Phased Array L-band Synthetic Aperture Radar (PALSAR) (Arnesen et al., 2013; Ferreira-Ferreira et al., 2015) and ALOS-2 PALSAR-2 backscatter retrievals (Jensen et al., 2018) for subsets of Amazon wetlands. However, with a few exceptions using subregional datasets (Arnesen et al., 2013; Ferreira-Ferreira et al., 2015; Hess et al., 2003; Jensen et al., 2018; Resende et al., 2019), in situ validation of the basin-scale estimates has seldom been performed, given the remoteness of

much of the Amazon basin and the often dense forest cover, which hampers airborne monitoring of below-canopy inundation.

Complementary to the remotely sensed datasets, process-based hydrological models estimating variables such as river discharge and flood extent have been developed and assessed from basin to local scales in the major rivers of the basin (Beighley et al., 2009; Coe et al., 2008; Getirana et al., 2017, 2012; Hoch et al., 2017; Luo et al., 2017; Miguez-Macho and Fan, 2012; Paiva et al., 2013; Yamazaki et al., 2011), thanks to the advent of new computational and modeling capabilities. Local-scale hydraulic models with coarse (Trigg et al., 2009; Wilson et al., 2007; Fleischmann et al., 2020) and detailed input data (Ji et al., 2019; Pinel et al., 2019; Rudorff et al., 2014; Fassoni-Andrade, 2020) have further developed model capabilities for mapping inundation dynamics, especially for the floodplains fringing the Amazon mainstem. These models complement satellite-based flood mapping due to their higher temporal and spatial resolution, and capability to estimate long-term time series, for both past and future (e.g., due to climate change) scenarios. The understanding of their uncertainties can lead to optimal data fusion with satellite-based estimates, such as considering multiple constraints within the water cycle representation (Pellet et al., 2021).

Among these numerous inundation datasets for the Amazon basin (Tables 1 and S1), divergences can be substantial due to the differences in sensor systems, timing, and data processing algorithms (Aires et al., 2018; Fleischmann et al., 2020; Parrens et al., 2019; Pham-Duc et al., 2017; Rosenqvist et al., 2020), and a comprehensive assessment of inundation estimates for the Amazon is lacking. The need to compare different hydrological datasets for the Amazon has been recently highlighted in the context of river discharge (Towner et al., 2019), precipitation (Wongchuig et al., 2017; Zubieta et al., 2019) and evapotranspiration (Paca et al., 2019; Wu et al., 2020). Meanwhile, rapid environmental changes in the basin underscore the urgency for a better understanding of

Amazon water resources (Fassoni-Andrade et al., 2021), for which management and planning can be hindered by the discrepancies among datasets. These questions regarding current data limitations in the largest basin in the world are also timely in anticipation of forthcoming hydrological satellite missions such as Surface Water and Ocean Topography (SWOT) and NASA-ISRO SAR (NISAR).

To better understand and quantify the state of understanding of inundation patterns in the Amazon wetlands, we address the following questions: 1) How much Amazon land area is subject to seasonal or permanent flooding, and how accurate are the estimates? 2) Which areas are in particular disagreement and thus deserve further attention? 3) How do basin-scale estimates with coarser resolution and less calibrated classification methods differ from those for individual wetland complexes, with independent validation? 4) How do the various inundation estimation approaches (optical imagery, SAR, passive microwave, hydrologic models) differ in terms of inundation mapping and for different wetland types (e.g., floodplains and interfluvial areas)? In order to answer these questions, we gathered 29 inundation datasets for the Amazon basin, spanning a wide range of spatial (12.5 m to 25 km) and temporal (static, dual-season, monthly, daily) resolutions, and coverages from the whole basin to individual wetland complexes (Table 1), into a framework that provides a comprehensive assessment of current knowledge of Amazon inundation.

Table 1. List of 29 studies that mapped inundation over areas ranging from the entire Amazon basin to individual wetland complexes. These data sources were selected based on data availability and relevance for this intercomparison. In the case of hydrological models, time resolutions are the values assessed or provided by the models, which can be provided at finer time resolution if necessary, since many of them compute flood maps at daily or sub-daily time steps

and report time-integrated results. The column "Data type" refers to: OS: optical sensor; SAR: synthetic aperture radar; HM: hydrological model; HR: multiple datasets at high resolution; CR: multiple datasets at coarse resolution. The column "Type of inundation estimated" has three classes: "All", meaning both open water and vegetated wetlands, "Open water", and "Wetland only (no open water)".

Data type	Dataset name and main mission/ model associated (if applicable)	Spatial resolution	Temporal resolution	Time period	Region	Type of inundation estimated	Reference
CR	GIEMS-2	25 km	Monthly	1992-2015	Basin	All	Prigent et al., 2020
CR	SWAMPS	25 km	Monthly	1992-2020	Basin	All	Jensen and McDonald, 2019
CR	WAD2M	25 km	Monthly	2000-2018	Basin	Wetland only (no open water)	Zhang et al., 2020
HR	GIEMS-D3	90 m	Monthly	1993-2007	Basin	All	Aires et al., 2017
HR	CIFOR	232 m	Static (max inundation)	1950-2000	Basin	All	Gumbricht et al., 2017
HR	ESA-CCI	300 m	Annual	1992-2015	Basin	All	Bontemps et al., 2013
HR	GIEMS-D15	500 m	Monthly climatology	1993-2004	Basin	All	Fluet-Chouinard et al., 2015
HR	GLWD	1 km	Static	1992-2004	Basin	All	Lehner and Döll, 2004

HR	SWAF-HR / SMOS mission	1 km	Weekly to monthly	2010-2020	Basin	All	Parrens et al., 2019
HM	THMB model	5-min	Monthly	1961-2010	Basin	All	Coe et al., 2008
HM	CaMa-Flood model	500 m	Monthly	1980-2014	Basin	All	Yamazaki et al., 2011
HM	MGB model	500 m	Monthly	1980-2015	Basin	All	Siqueira et al., 2018
HM	Bonnet model	180 m	Monthly	2006-2019	Janauacá	All	Bonnet et al., 2017
HM	TELEMAC-2D model	30 m	Monthly	2006-2015	Janauacá	All	Pinel et al., 2019
HM	LISFLOOD-FP model	90 m	Monthly	1994-2015	Curuai	All	Rudorff et al., 2014
OS	G3WBM / Landsat mission	30 m	Static (open water areas)	1990-2010	Basin	Open water	Yamazaki et al., 2015
OS	GLAD / Landsat mission	30 m	Annual and monthly climatology	1999-2018	Basin	Open water	Pickens et al., 2020
OS	GSWO / Landsat mission	30 m	Monthly (cloud cover may occur)	1984-2019	Basin	Open water	Pekel et al., 2016
OS	Ovando / MODIS mission	500 m	8 days	2001-2014	Llanos de Moxos	Open water	Ovando et al., 2016
OS	Park / MODIS mission	230 m	Monthly climatology	2000-2015	Amazon River down-	Open water	Park and Latrubesse, 2019

					stream of Manaus		
SAR	Hess / JERS-1 mission	90 m	Max. and min. annual inundation (dual season)	1995-1996	Basin (lowlands)	All	Hess et al., 2003, 2015
SAR	Chapman / ALOS-PALSAR mission	90 m	Monthly	2006-2011	Basin	All	Chapman et al., 2015
SAR	Rosenqvist / ALOS-2 PALSAR-2	50 m	Max. and min. annual inundation (dual season)	2014-2017	Basin	All	Rosenqvist et al., 2020
SAR	Jensen / ALOS-2 PALSAR-2 mission	50 m	Irregular (26 images)	2014-2018	Pacaya-Samiria	All	Jensen et al., 2018
SAR	Arnesen / ALOS-PALSAR mission	90 m	Irregular (12 images)	2006-2010	Curuai	All	Arnesen et al., 2013
SAR	Ferreira-Ferreira / ALOS-PALSAR mission	12.5 m	Flood frequency only	2007-2010	Mamirauá	All	Ferreira-Ferreira et al., 2015
SAR	Ovando-2 / ALOS-PALSAR mission	100 m	Irregular (6 images)	2006-2010	Llanos de Moxos	All	Ovando et al., 2016
SAR	Pinel-2 / ALOS-PALSAR mission	30 m	Irregular (16 images)	2007-2011	Janauacá	All	Pinel et al., 2019
SAR	Resende / ALOS-PALSAR mission	25 m	Static (max inundation)	2006-2011	Uatumã	All	Resende et al., 2019

2. Methodology

2.1 Study area

The Amazon basin spans around 6 million km² in nine South American countries (Figure 1), with high annual rainfall (~2,200 mm year^{-1}), and the Amazon River discharge makes a major contribution to global freshwater and sediment exports to the ocean (Fassoni-Andrade et al., 2021). We delineated the catchment area upstream from Gurupá city, within the tidal river ~390 km from the ocean; hence not including the Tocantins-Araguaia basin and parts of the Amazon estuary and Marajó Island. We selected the 5.11 x 10^6 km² of Amazon lowlands defined as areas lower than 500 m elevation based on the Shuttle Radar Topography Mission Digital Elevation Model (SRTM DEM) for the area of dataset comparisons in our study. This decision is consistent with several studies limited to lowlands because of the limitations of certain methods in estimating flooding in mountainous terrain (Hess et al., 2015).

In addition to basin-scale datasets, estimates of inundated areas for 11 individual wetland complexes (also referred to as "subregional") in the Amazon basin were analyzed, including seven areas for which more detailed estimates were available. This was performed to understand how the basin-scale datasets may vary in accuracy across different wetland types (Figure 1): Curuai floodplain lake (Arnesen et al., 2013; Rudorff et al., 2014), Janauacá floodplain lake (Bonnet et al., 2017; Pinel et al., 2019), Uatumã river floodplain (Resende et al., 2019), Mamirauá Reserve (Ferreira-Ferreira et al., 2015), Pacaya-Samiria wetlands (Jensen et al., 2018), Llanos de Moxos

wetlands (Ovando et al., 2016), lower Amazon floodplain (Park and Latrubesse, 2019), Amazon mainstem floodplain (from Iquitos to Gurupá), Purus floodplain, Roraima savannas, and Negro savannas. A brief summary of these wetlands is provided in supplementary Table S2, and their main features are summarized in the following. Curuai is representative of the shallow lakes in the lower Amazon floodplain. It is separated from the river by narrow levees (Rudorff et al., 2014) and has a high suspended sediment concentration. Janauacá is typical of the middle Amazon River floodplain, and is composed of a ria lake (i.e., a blocked valley lake with relatively sediment-free waters; Latrubesse (2012)) and "várzea" environments (white-water floodplains) in its northern part (Pinel et al., 2019). Uatumã River is an Amazon tributary with black-water floodplain ("igapó"), and includes the Balbina hydroelectric reservoir, operating since 1987, which affects the river's hydrological regime (Schöngart et al., 2021). The Uatumã floodplain reach assessed here is the 300-km reach between Balbina dam and the confluence with the Amazon River. The Mamirauá Sustainable Development Reserve is located in the confluence between Solimões and Japurá rivers, and is characterized by a mosaic of "chavascal", herbaceous, and low and high várzea vegetation (Ferreira-Ferreira et al., 2015). The Purus River is a major tributary, and its floodplain was chosen because of its large floodplain to river width ratio. Pacaya-Samiria wetlands are composed of flooded forests, palm swamps and peatlands in the upper Solimões River (Draper et al., 2014; Lähteenoja et al., 2012). The Llanos de Moxos floodable savannas occupy the interfluvial areas between the Beni, Mamoré and Madre de Dios rivers in the upper Madeira basin (Hamilton et al., 2004). The Negro savannas, locally known as "campina wetlands" and "campinarana wetlands", depending on the vegetation density, are thought to have formed from regional neotectonic depressions and were called the "Septentrional Pantanal" given their large area (Rossetti et al., 2017a, 2017b; Santos et al., 1993). The Roraima floodable savannas extend

from Roraima State in Brazil to the Rupununi savannas in Guyana, and comprise mainly smaller river floodplains interspersed with poorly drained interfluvial savannas subject to flooding by local rainfall (Hamilton et al., 2002); here we only considered the Roraima wetlands in the upper Branco River basin, which is within the Amazon basin.

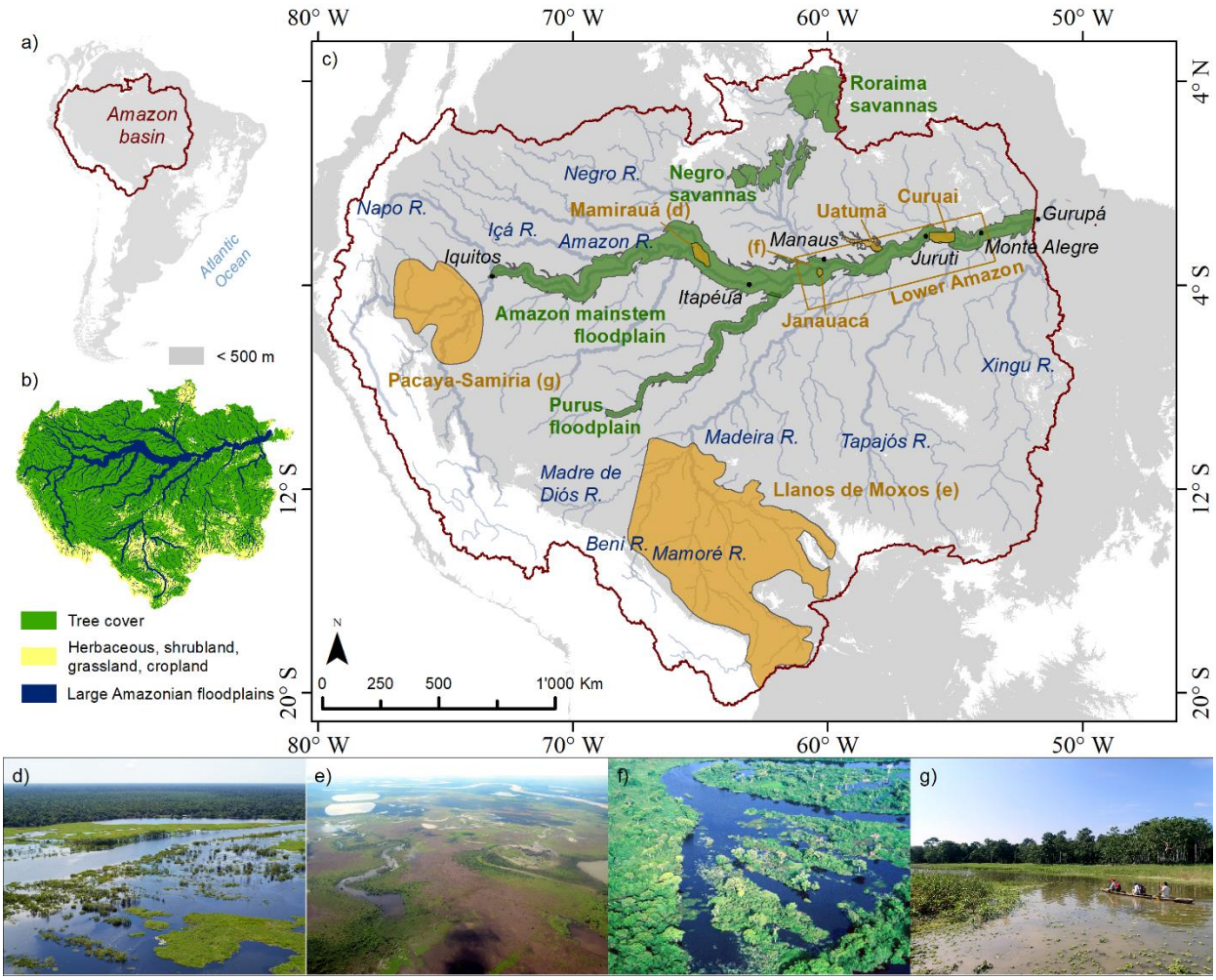

Figure 1. The Amazon basin and its major wetland systems: (a) Amazon basin delineation (red lines) over the countries of South America (black lines). (b) Land cover based on a 2010 map from the European Space Agency Climate Change Initiative (ESA-CCI) (Bontemps et al., 2013), showing the distribution of forest and savanna across the basin, as well as large floodplains (see methodology section 2.3). (c) Basin distribution of major wetland systems showing locations

of interest for this study. Elevations lower than 500 m are shown in grey (based on SRTM DEM). The orange polygons show the areas for which a subregional dataset was available for this study (Figure 4), and the green ones show wetland areas of interest that do not have datasets specifically designed for these subregions. Photos depicting different wetland complexes for (d) Mamirauá (courtesy of João Paulo Borges Pedro), (e) Llanos de Moxos (courtesy of Alex Ovando), (f) Cabaliana floodplain lake close to Manacapuru (courtesy of Stephen Hamilton), and (g) Pacaya-Samiria (courtesy of Katherine Jensen) regions, respectively.

2.2 Datasets

Twenty-nine inundation datasets covering areas ranging from the whole-basin scale to individual wetland complexes, based on multiple data sources and spatiotemporal resolutions, were assembled for our comparison (Table 1). Most of these datasets are recent, with 18 out of the 29 published since 2016, and 27 since 2011. They were chosen due to data availability and representativeness; other datasets that were either unavailable or methodologically redundant to those in our comparison were not used but are catalogued in Table S1. Overall, there are eight dynamic (weekly to monthly; Figure 2) and 10 static (which include long-term maximum, annual or dual-season categories; Figure 3) basin-scale datasets.

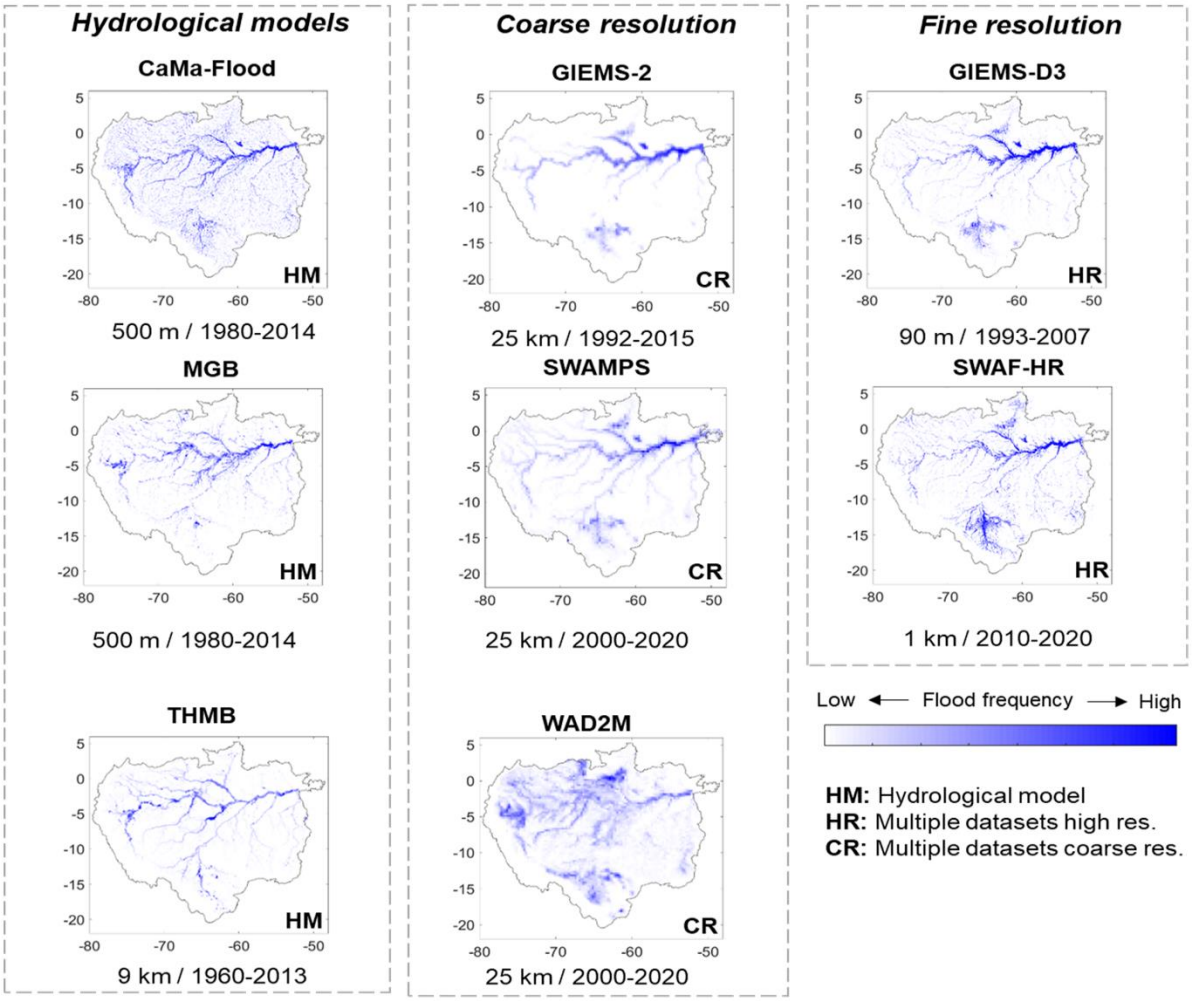

Figure 2. Basin-scale, dynamic inundation datasets used in this study, divided into three classes (hydrological models; merging of multiple datasets at high resolution; merging of multiple datasets at coarse resolution). Long-term flood frequency maps are provided for each dataset, calculated as the percentages of observations labelled as flooded throughout the entire time-series.

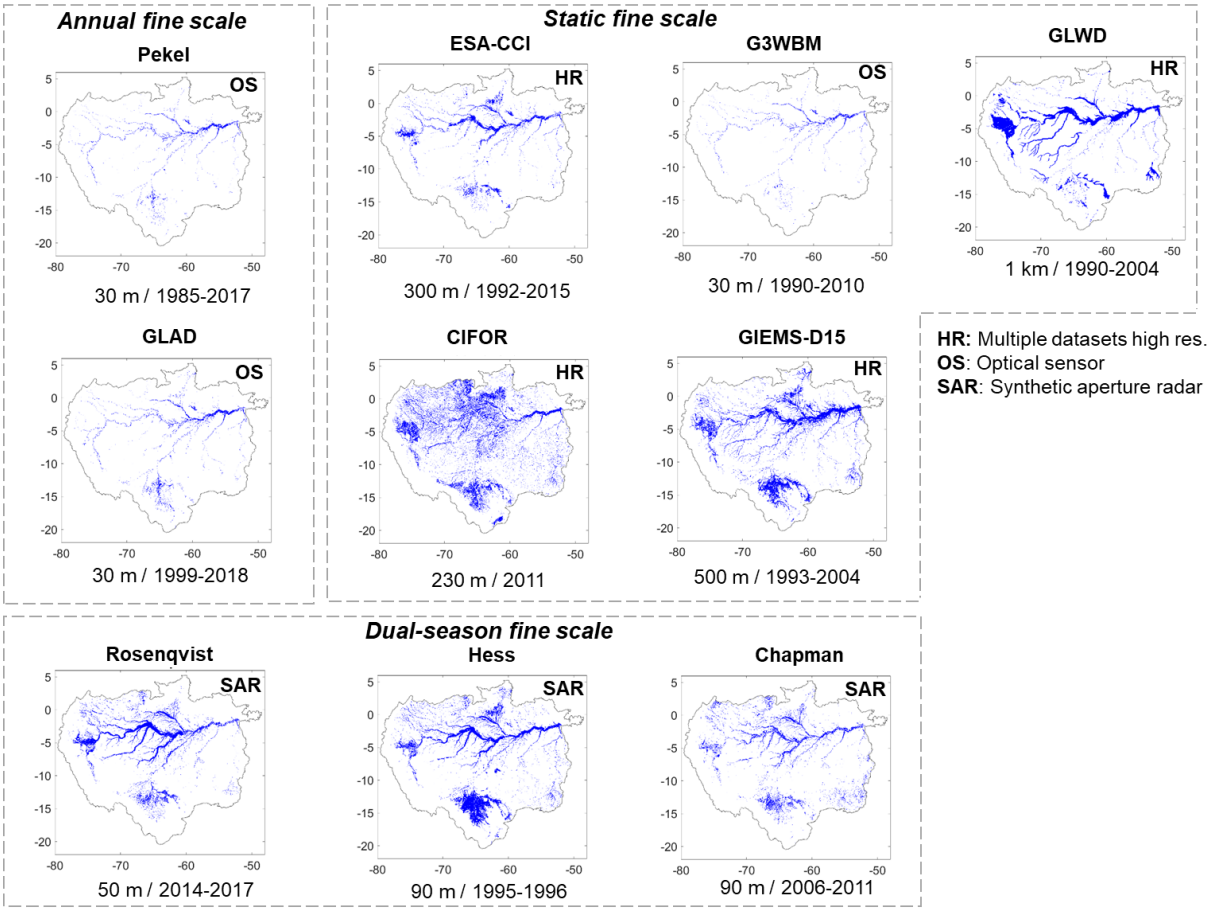

Figure 3. Basin-scale, static or dual-season inundation datasets used in this study, divided into three classes (merging of multiple datasets at high resolution; based on optical sensors; and based on SAR data). Flood frequency maps are not provided because the datasets are mainly static or annual-based.

Passive microwave (PM) data are the basis of SWAF-HR, GIEMS family (GIEMS-D15, GIEMS-D3, GIEMS-2), and SWAMPS, while ancillary data (i.e., optical imagery and microwave scatterometry) are used to complement the PM signal. SWAF-HR data result from the disaggregation of water surface fraction in a dataset at coarser spatial resolution (SWAF), based on L-band passive microwave observations from the Soil Moisture and Ocean Salinity (SMOS) satellite (Parrens et al. 2017). The disaggregation of SWAF relies on water occurrence maps from

GSWO and the Digital Elevation Model (DEM) Multi-Error-Removed-Improved-Terrain (MERIT) (Parrens et al., 2019). A global implementation of SWAF based on multi-angular and multi-polarization information has also been implemented (Al Bitar et al. 2020). GIEMS merges multiple satellite passive and active microwave observations, along with the optically-derived NDVI (Normalized Difference Vegetation Index), to detect the surface water and estimate the vegetation attenuation, for a monthly quantification of the surface water extent at ~25 km spatial resolution (Prigent et al., 2001, 2007, 2020; Papa et al., 2010). It is further disaggregated at 90-m resolution (GIEMS-D3) using a topographical downscaling methodology (Aires et al. 2017).

Three basin-scale datasets are based mainly on SAR data from JERS-1 (Hess et al., 2003, 2015), and its successor missions ALOS-PALSAR (Chapman et al., 2015) and ALOS-2 PALSAR-2 (Rosenqvist et al., 2020). These three datasets cover different decades of observation but are methodologically similar.

Three of the optical-based datasets are based on Landsat data: GSWO (Pekel et al., 2016), G3WBM (Yamazaki et al., 2015) and GLAD (Pickens et al., 2020). Although GSWO and GLAD can provide monthly estimates for the Landsat archive (1984-today), given the inability of optical data to estimate flooding under cloud cover or dense vegetation canopies, only annual maximum and minimum values are used. For GLAD and GSWO, we consider a threshold of occurrence of surface water of 95% to estimate the minimum inundation (i.e., for the permanently inundated areas; Aires et al., 2018); otherwise, only a few isolated open water areas would be considered for the minimum extent.

The European Space Agency Climate Change Initiative dataset (ESA-CCI) is based on surface reflectance from MERIS, the Advanced Very High-Resolution Radiometer (AVHRR) and

PROBA-V data and Global Water Bodies from the Envisat Advanced Synthetic Aperture Radar (ASAR) (Bontemps et al., 2013). Since the wetland pixels in ESA-CCI varied negligibly throughout the years of observations, we use only the 2010 dataset as the ESA-CCI estimate for maximum inundation.

Another set of data is based on the merging of multiple global datasets: GLWD, GIEMS-D15 and WAD2M. GLWD is one of the first globally consistent databases of wetlands, which was based on a collection of wetland estimates from diverse institutions worldwide (Lehner and Döll, 2004). GIEMS-D15 combines GLWD, the Hydrosheds drainage network, and Global Land Cover 2000. WAD2M is based on SWAMPS and CIFOR within its merging framework. WAD2M is the only dataset to exclude open water areas (removal based on GSWO) due to its goal of estimating wetland methane emissions. SWAF-HR (Parrens et al., 2019) and GIEMS-D3 (Aires et al., 2017) use additional data and methodologies to downscale the original 25-km passive microwave-based SWAF (Parrens et al., 2017) and GIEMS (Papa et al., 2010; Prigent et al., 2007) datasets to 1 km and 90 m, respectively. While GIEMS-D3 has a different inundation magnitude than the original GIEMS due to merging with ancillary data, SWAF-HR conserves the same inundation magnitude across scales.

Among hydrological models, we selected representative datasets from each of the following broad modeling types: 1) process-based hydrologic models that use flood routing to represent inundation processes (i.e., from a simple kinematic wave model coupled to an inundation method to more complex flow routing methods); or 2) hydraulic (or hydrodynamic) models that consider the shallow water equations (or its simplifications) at any dimension (1D, 2D or 3D). For our analysis, we adopted two basin-scale models – one hydrologic (THMB; Coe et al. (2008)) and one hydrologic-hydrodynamic (MGB, Siqueira et al. (2018)), as well as a global-scale hydrodynamic

model (CaMa-Flood, Yamazaki et al. (2011)), in the Earth2Observe version available at <http://www.earth2observe.eu/>). The inundated area estimation is largely affected by the DEMs. The DEMs adopted in the model runs were: Bare-Earth (O'Loughlin et al., 2016) for MGB, MERIT (Yamazaki et al., 2017) for CaMa-Flood, and SRTM (Farr et al., 2007) for THMB. The rainfall/runoff input data are MSWEP v.1.1 daily precipitation (Beck et al., 2017) for MGB, HTESSEL daily runoff (Balsamo et al., 2009) for CaMa-Flood, and CRU TS v.3.2.1 monthly precipitation (Harris et al. 2014) for THMB. Although other hydrologic models have been applied to the Amazon basin (Tables 1 and S1), the models chosen here were selected as representative of global to local models, for having been well validated and applied over the Amazon basin, and for representing state-of-the-art Amazon hydrologic modeling. All basin-scale models represent one-dimensional (1D) flows only (i.e., floodplains are represented as storage units without active flow), and thus do not represent 2D surface flows that occur in wetlands (Alsdorf et al., 2007; Fleischmann et al., 2020). A detailed comparison of model capabilities and structural uncertainties is beyond our current scope. Hydrologic models have different temporal resolution depending on their numerical stability and forcing data. For instance, MGB and CaMa-Flood models run at an adaptive time step (sub-minute timestep in the case of MGB), but are assessed at daily resolution given their daily precipitation forcing. We aggregated the models' estimates to monthly averages to make them comparable to the remote sensing dynamic datasets.

The datasets available for individual wetland complexes are presented in Figure 4. ALOS-2 PALSAR-2 data were used for the Pacaya-Samiria region (Jensen et al., 2018), and the ScanSAR mode of ALOS/PALSAR for the following datasets: Curuai floodplain lake (Arnesen et al., 2013), Mamirauá Reserve (Ferreira-Ferreira et al., 2015), Uatumã river floodplain (Resende et al., 2019), and Janauacá floodplain lake (Pinel et al., 2019). MODIS optical data were used for the Llanos de

Moxos savannas in the upper Madeira River basin (Ovando et al., 2016) and the lower Amazon floodplain (Park and Latrubesse, 2019). Two local-scale 2D hydraulic models (LISFLOOD-FP for Curuai lake, Rudorff et al. (2014), and TELEMAC-2D for Janauacá lake, Pinel et al. (2019)), and one local-scale hydrologic model (for Janauacá lake; Bonnet et al. (2017)) were considered; together, these are representative of the state-of-the-art of hydrological modeling in Amazon wetlands.

The datasets were stored in various formats (i.e., raster and polygon shapefiles) and projections (mainly projected UTM and geographic coordinate system with WGS84 datum), and were converted to the WGS84 geographic coordinate system to compute areas. SWAMPS was provided at the Equal-Area Scalable Earth (EASE) Grid, which was used to estimate its flooded areas. Hydrologic model outputs were provided as either binary inundation maps or flood depth raster files, which were then converted into binary maps by assuming depth > 0 m as inundated pixels.

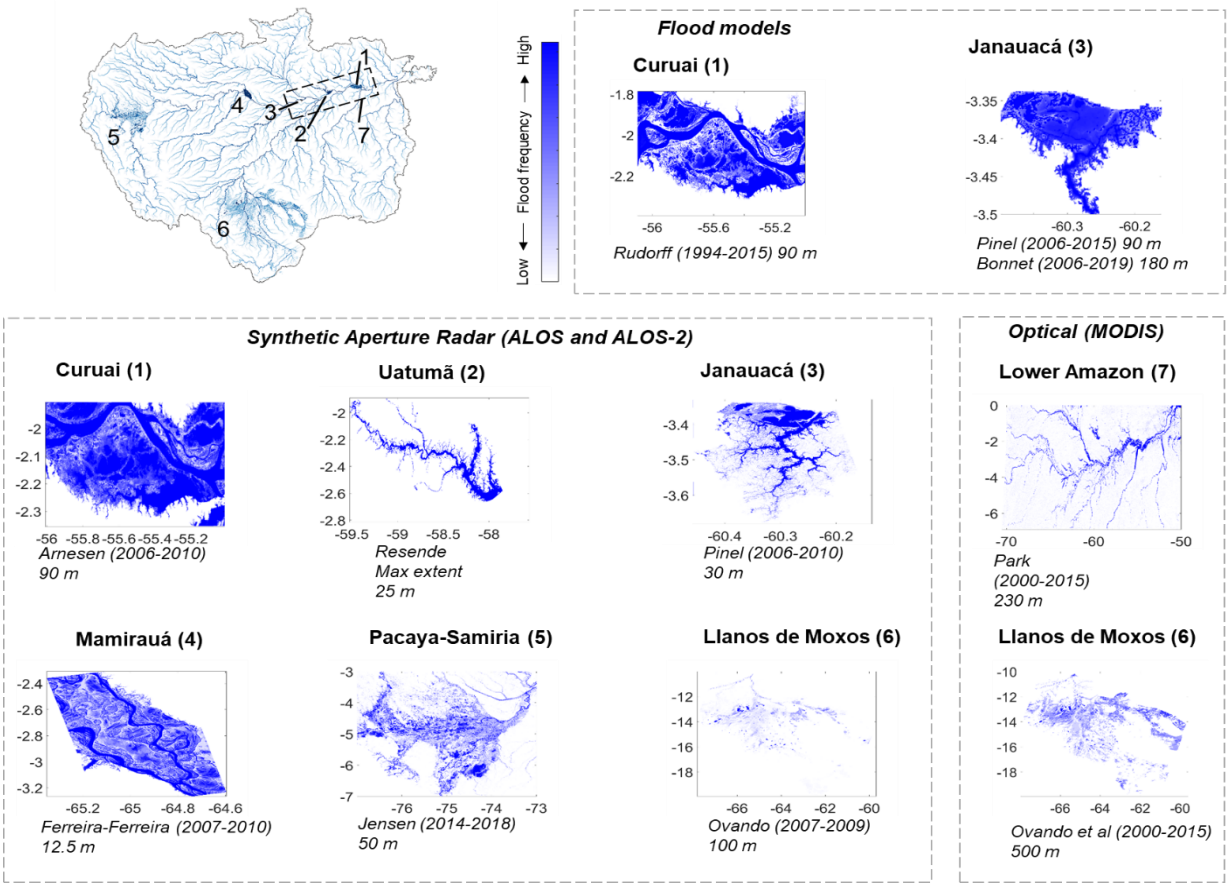

Figure 4. Long-term flood frequency maps from subregional inundation datasets (i.e., for individual wetland complexes) used in this study. The Uatumã dataset (2) is static and is displayed as the maximum extent. Flood frequency maps are produced by computing the long-term average of all inundation maps available for each dataset.

2.3 Comparison framework

The comparison framework involved the following analyses, considering the entire basin and 11 wetland complexes (seven areas with available subregional estimates, and four additional areas of interest without subregional estimates; Figure 1):

- Annual maximum and minimum inundation estimates for each of the 18 basin-scale datasets (section 3.1);
- Basin-scale, long-term maximum and minimum inundation estimates for each of the 18 basin-scale datasets (section 3.1);
- Long-term maximum and minimum inundation estimates for each of the 18 basin-scale and 11 subregional datasets (section 3.2);
- Comparison between basin-scale and subregional datasets with temporal (nRMSD and Pearson correlation) and spatial (Fit metric) assessment (section 3.2);
- Assessment of spatial agreement among the 18 basin-scale datasets at 1 km, for both long-term maximum and minimum inundation maps (section 3.3);
- Estimation of long-term maximum inundation for two classes of wetlands for the entire basin: (i) medium to large river floodplains and (ii) interfluvial wetlands and small floodplains (section 3.4).

The long-term maximum and minimum inundation extents were computed for each dataset as the area of all pixels that were inundated at least once in the whole monthly time series, for the maximum, and as those pixels that were always inundated, for the minimum. We stress that analyzing long-term changes in inundation patterns is beyond the scope of this study, and thus we assumed stationarity in our comparisons of long-term maximum and minimum inundation extents from different time-periods.

The agreement of all basin-scale, high-resolution datasets (i.e., all basin-scale ones except for THMB, GIEMS-2, SWAMPS and WAD2M, which have a coarse resolution between 9 and 25

391 km) was assessed for long-term maximum and minimum inundation at 1 km resolution, which is
392 the resolution of SWAF-HR, the coarsest resolution among the high-resolution datasets. For each
393 1 km pixel, the total number of datasets agreeing that it was inundated (either for maximum or
394 minimum extent) was computed, following Trigg et al. (2016). Given the size of the Amazon basin,
395 a 1 km resolution was considered adequate for the analysis. The analysis was done by aggregating
396 all datasets to 1 km, and considering that a 1 km pixel is flooded if more than 50% of its area is
397 flooded (following Hamilton et al., 2002). A sensitivity test was performed using a 25% threshold
398 and led to similar conclusions at the whole basin scale (Figure S1).

399 The basin-scale and four additional subregional datasets were compared to seven subregional ones,
400 which were used as independent validation datasets, and cover the following sites: Curuai
401 (Arnesen et al., 2013), Uatumã (Resende et al., 2019), Janauacá (Pinel et al., 2019), Mamirauá
402 (Ferreira-Ferreira et al., 2015), Pacaya-Samiria (Jensen et al., 2018), Llanos de Moxos MODIS
403 (Ovando et al., 2016) and lower Amazon River (Park and Latrubesse, 2019). Varying degrees of
404 validation exercises were performed for these validation datasets, with some being extensively
405 validated with airborne videography (Hess et al., 2003) or local surveys (Arnesen et al., 2013;
406 Ferreira-Ferreira et al., 2015; Jensen et al., 2018; Resende et al., 2019), while others were assessed
407 through comparisons with other datasets (Pinel et al., 2019), or visually inspected, as in the large
408 domains of the Llanos de Moxos (Ovando et al., 2016) and lower Amazon River (Park and
409 Latrubesse, 2019) subregional datasets. The four additional subregional datasets are: Curuai
410 LISFLOOD-FP model (Rudorff et al., 2014), Janauacá hydrological model (Bonnet et al., 2017),
411 Janauacá TELEMAC-2D model (Pinel et al., 2019), and Llanos de Moxos ALOS-PALSAR
412 (Ovando et al., 2016).

To use the subregional studies to assess the accuracy of the datasets covering broader areas, the basin-scale and four additional subregional datasets were compared to the subregional validation datasets at monthly temporal resolution, considering the total inundated area per wetland area (i.e., the whole Curuai Lake domain, the whole Uatumã floodplain, and so forth). The polygons of each wetland area, which were used to extract the information from the basin-scale datasets, were delineated as a 1-km buffer around the maximum inundated area, according to each subregional dataset. For the four areas of interest without subregional datasets (Amazon mainstem and Purus floodplains, and Roraima and Negro wetlands), the polygons were created considering the maximum lateral extent in accordance with the MERIT DEM (Yamazaki et al., 2017) and ESA-CCI land cover for savannas. The time series were compared with Pearson linear correlation (R) and the normalized root mean square deviation (nRMSD), computed as the RMSD between a given inundation map and the subregional validation map (i.e., the individual wetland complexes) divided by the subregional long-term average inundation. The term 'deviation' was preferred over 'error' to stress the uncertainties inherent to all datasets, for both basin and subregional scales, although those derived for an individual wetland complex are considered as superior in accuracy for having a more dedicated data processing for that particular area, and being validated with ground surveys in some cases.

The ability of a particular dataset to estimate the local spatial patterns at maximum inundation was assessed with the Fit metric (Bates and De Roo, 2000), which has been successfully applied to compare inundation datasets (Bernhofen et al., 2018), and is computed as:

$$Fit = 100\% * \frac{A \cap B}{A \cup B} (1)$$

Where A and B are the subregional validation dataset estimates (e.g., the subregional map that corresponds to maximum inundation) and the basin-scale maximum inundation maps.

To assess different wetland environments, we differentiate medium to large river floodplains from interfluvial wetlands and small floodplains. An estimation of the total flooded area of large river floodplains was computed, considering river reaches with upstream drainage area larger than 1,000 km², and a buffer mask around the river reaches (mask presented in Figure 1). The buffer was defined based on the Hydrosheds drainage network (Lehner and Grill, 2013), segmented into 15 km-long reaches as in Siqueira et al. (2018). The buffer was proportional to the local reach drainage area and further manually adjusted to include the maximum floodplain lateral extent, as estimated from a visual inspection of the MERIT DEM (Yamazaki et al., 2017) and the three basin-scale SAR-based datasets (Hess, Chapman and Rosenqvist datasets). Buffer values varied from 4 km in upper reaches to 150 km on the Amazon mainstem close to the Mamirauá Reserve. Estimating floodplain total inundated area is relevant to differentiate the Amazon riverine fringing floodplains from non-floodplain wetlands (here referred to as interfluvial wetlands).

Finally, in order to assess the current capabilities of basin-scale mapping of inundation dynamics at high spatial and temporal resolution, a further assessment of the four high-resolution dynamic datasets (GIEMS-D3, CaMa-Flood, SWAF-HR and MGB) at their native resolutions was performed by computing their long-term flood frequency for the entire basin.

3. Results and Discussion

3.1 How much inundation is estimated to occur in the Amazon basin?

3.1.1 Overall assessment

Comparisons among the various estimates of inundation area can begin with the maximum and minimum inundated area across the entire Amazon basin. We found wide variation in the annual maximum and minimum inundation estimates for the entire basin scale (Figure 5), as well as the long-term maxima and minima (Figure 6 and Table 2). The annual maximum inundation area represents the total area subject to inundation at some point over the year, whereas the annual minimum inundation area represents the area that remained inundated all year. SAR estimates, especially those based on L-band sensors and those having undergone validation (i.e., the Hess et al. (2003) dataset), are assumed to be the most accurate given their high spatial resolution and capability of mapping flooded areas under dense vegetation canopies and cloud cover. Given the lack of ground validation for most basin-scale datasets, we assess their accuracy by comparing them to subregional validation datasets in section 3.2.

By computing means and standard deviations of the long-term maximum area subject to inundation by type of data (Table 2), we obtain the following values: 138,200 ± 45,300 km² (mean ± S.D.) for optical, 533,500 ± 217,800 km² for multiple datasets at high resolution, 579,100 ± 108,900 km² for those at coarse resolution, 542,800 ± 80,600 km² for hydrological models, and 599,700 ± 81,800 km² for SAR. The mean area for optical-based datasets is thus around 23% of the SAR-based estimate. If we assume that the ensemble of datasets could be a proxy of inundation uncertainty in the Amazon basin, and neglecting the optical and land cover-based data (G3WBM, GLAD, GSWO and ESA-CCI) and CIFOR datasets, given their lower capability to map inundation as discussed below, 13 datasets are left, yielding an estimation for the long-term maximum inundation of 559,300 ± 81,100 km². This value is around 40,000 km² lower than the mean of the maximum inundation area from the three SAR datasets. The mean of the maximum inundation

478 area considering all 18 datasets is 490,300 ± 204,800 km². Compared to the maximum inundation
479 area, the relative deviation among available estimates is higher for the long-term minimum area
480 inundated —125,900 ± 77,600 km² (mean ± S.D.), with a coefficient of variation of 0.62, for the
481 12 basin-scale datasets that provide minimum area, and 139,300 ± 127,800 km² for the three SAR-
482 based datasets, with a coefficient of variation of 0.92.

483 None of the datasets can map small, narrow floodplains or riparian zones, for which only simple
484 calculations are currently available (e.g., Junk et al., 1993), and whose total area can only be
485 estimated through statistical extrapolation of observable rivers. These small zones contribute to
486 the overall uncertainties of the inundation estimates. For instance, a wetland mask developed by
487 Hess et al. (2015) for SAR-based wetland classification yielded a basin-scale estimation of wetland
488 area including the smallest floodplains of 840,000 km². This estimate is much larger than the
489 largest long-term maximum inundated area obtained with SAR data (659,100 km² with
490 Rosenqvist's dataset). In section 3.2, it will be shown that almost all datasets tend to underestimate
491 the maximum inundation, when compared to subregional ones. The two SAR-based datasets with
492 highest accuracy underestimate maximum inundation by 9% (Rosenqvist) and 13% (Hess), based
493 on the average difference between these and the subregional estimates for the seven locations with
494 available data. If this holds true for the whole basin, the basin-scale maximum inundation would
495 be around 10% higher.

496

497 ***3.1.2 Estimates based on SAR datasets***

498 At the basin scale, SAR-based estimates of maximum annual inundation range from 424,600 km²
499 (Rosenqvist) to 633,500 km² (Hess), and minimum inundation from 53,900 km² (Rosenqvist) to

284,200 km² (Hess), as shown in Figure 5. By considering long-term maximum inundation (i.e., all pixels that were inundated at least once in the entire available time series), instead of annual maxima, the SAR-based estimates range from 506,400 km² (Chapman) to 659,100 km² (Rosenqvist) for the entire basin (Table 2). The minima vary from 42,400 km² (Rosenqvist) to 284,200 km² (Hess). This highlights the large differences that exist, especially for the minima, usually referred to as the "low-water period." Chapman's dataset, based on the 2006-2011 ALOS-PALSAR archive, has a smaller total maximum inundation area than the other two SAR datasets, as well as a smaller estimate for minimum inundation in relation to Hess' estimate, which in turn was developed from SAR mosaics at two seasons spanning only one year (1995–1996). Differences among the three datasets may originate from differences in acquisition dates, interannual and seasonal inundation variability, algorithms, spatial resolutions, or inconsistencies regarding the data processing. For example, Chapman estimates long-term maxima and minima based on multiple years, while Hess and Rosenqvist provide annual values. The calibration uncertainty was also higher for the JERS-1 data used in Hess' mapping than in the subsequent satellites (ALOS-PALSAR and ALOS-2 PALSAR-2) (Hess et al., 2003). For long-term minimum inundation, the interannual variability seems to be a minor factor since the Hess dataset, which estimated a larger figure than the other ones, was developed for a year with minimum water levels higher than those during Chapman's acquisition dates, but lower than those during Rosenqvist's ones (see Fig. 8 in Rosenqvist et al., 2020). Thus, the larger minimum inundation extent by Hess et al. (2015) seems to be more related to algorithm differences (Figure S2). For the maximum water levels, Hess' period was associated with an average year, below the water levels in Chapman and Rosenqvist, and this may explain the relatively higher long-term maximum inundation by Rosenqvist, while Chapman's smaller values are likely due to algorithm differences. For the

western basin, Hess' estimate is based on JERS-1 data mostly from June 1996 (Hess et al., 2015), which likely missed some of the inundation in this region as in the Pacaya-Samiria region, and may partly explain the larger value by Rosenqvist (see section 3.2.2). Spatial resolution is also an important factor: Rosenqvist's resolution is 50 m, and it is capable of representing smaller floodplains than the other two (Figure S3), as will be discussed in section 3.2.2.

3.1.3 Assessment of other datasets

The coarse-resolution datasets and hydrologic models generally estimate smaller annual maximum inundation areas in comparison to the SAR datasets, with the exception of SWAF-HR, WAD2M and CaMa-Flood that yield similar annual maximum inundation. This results from the low sensitivity of the passive microwave signal, which underlies most coarse-resolution datasets, to detect small fractional flooded areas within the grid cells, flooding under particularly dense vegetation, and flooding of short duration (i.e., less than one month of consecutive inundation) (Hamilton et al., 2002). The higher sensitivity of the SWAF-HR may be associated with the use of L-band passive microwave emission. Given the long-term data availability from dynamic, coarse-resolution datasets, their long-term mean estimates are closer to the SAR ones, varying from 450,800 km² (THMB) to 630,900 km² (SWAF-HR), when compared to the annual scale analysis. Therefore, no clear relationship between long-term minimum or maximum inundation and the spatial resolution of the datasets is observed (Figure 6), which could be expected when analyzing the annual values (Figure 5).

As expected, the optical-based datasets (GSWO, G3WBM, GLAD) cannot map inundation under dense vegetation canopies and thus lead to much lower estimates of basin-wide inundation area

(Aires et al., 2018; Parrens et al. 2017). Similarly, ESA-CCI, which is based on land cover classification of optical imagery with the addition of SAR inputs for delineation of wetland areas, yields low basin-wide inundation areas, although relatively higher than the purely optical-based estimates. In contrast, the multi-satellite-based CIFOR provides an unrealistically large estimate of maximum inundation area (872,700 km^2), which may be due to overestimation of soil moisture by the topographic index used. This method is sensitive to rainfall overestimation, which may have occurred in 2011, the year for which CIFOR was developed (Gumbricht et al., 2017). While the dataset does represent well the spatial extent of peatlands across the Pacaya-Samiria region (Gumbricht et al., 2017), its estimation of widespread inundation across the basin has limitations to represent the large Amazon river floodplains, especially the forested ones, which are classified as "swamps (including bogs)" by this dataset together with extensive interfluvial areas (Figure S4).

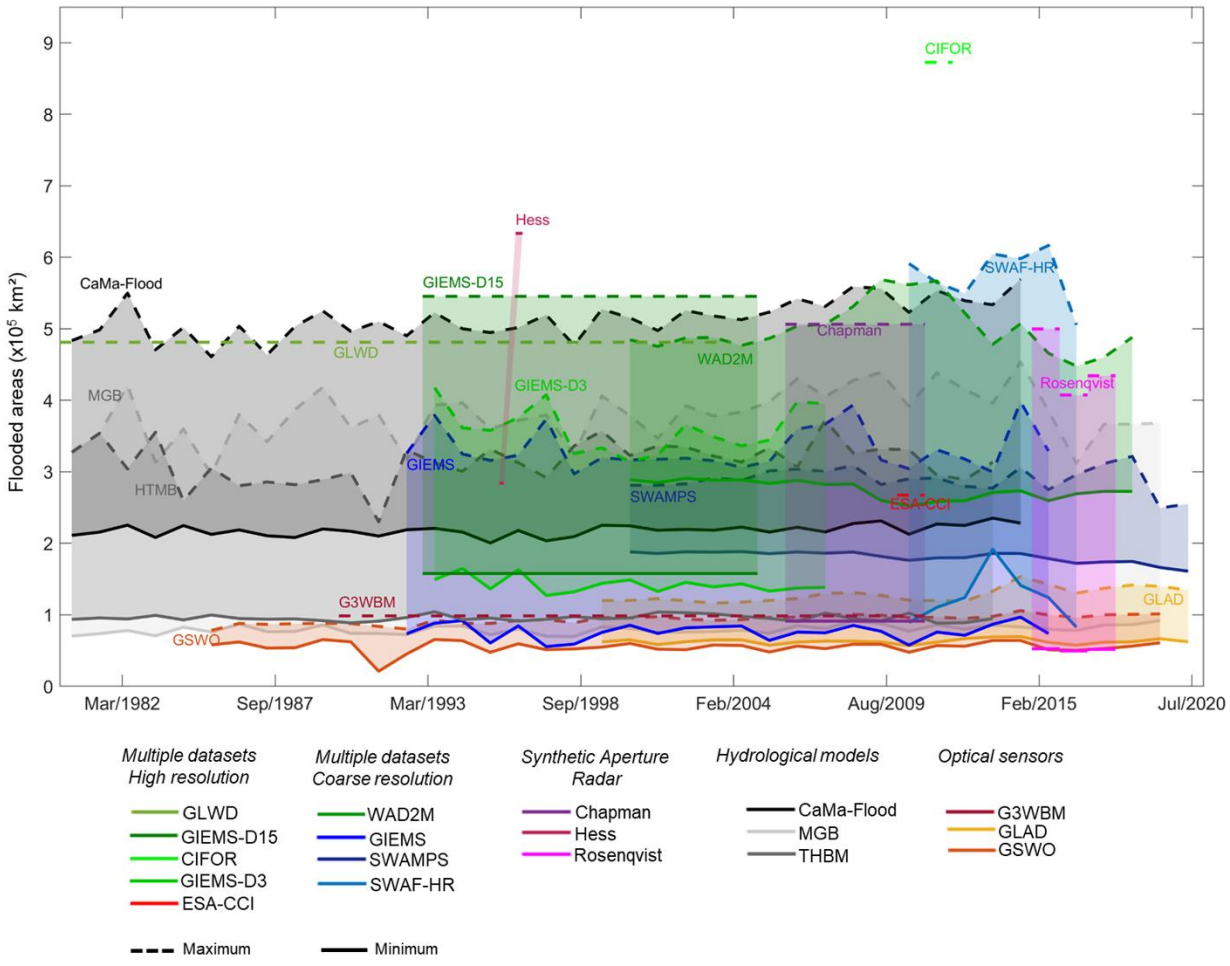

Figure 5. (a) Annual maximum and minimum flooded areas for the Amazon basin (< 500 m in elevation) for 18 basin-scale datasets over their respective observation time periods. Note that some datasets provide only average estimates based on multiple years of observation (e.g., GLWD, Chapman, G3WBM), and are marked as horizontal lines for the period of observation.

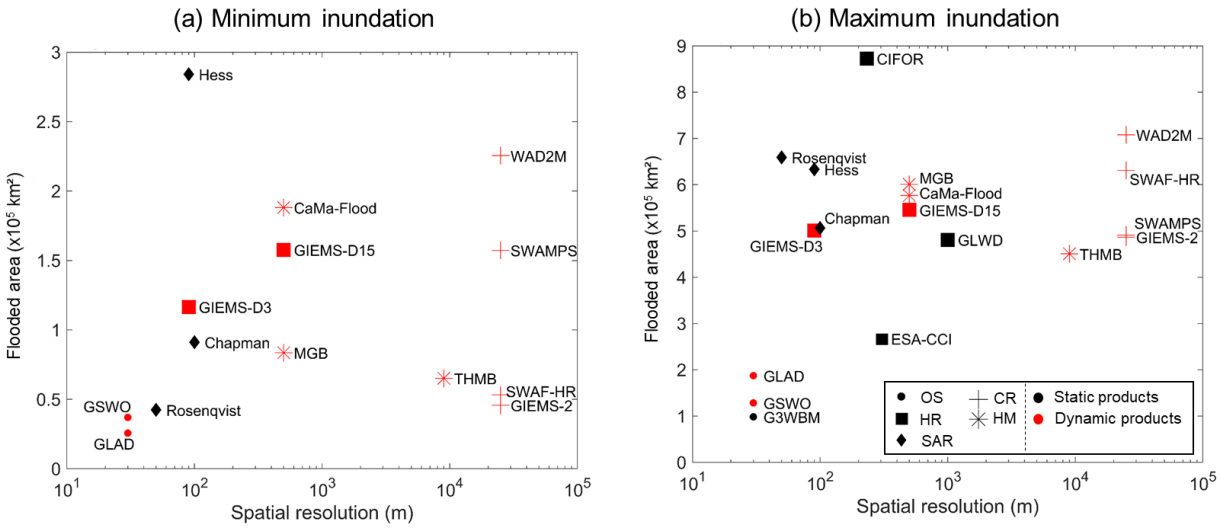

564

565 Figure 6. Summary of long-term (a) minimum and (b) maximum inundation for the 18 basin-scale datasets, which are
566 categorized into five types (optical data; combination of datasets at high resolution; combination of datasets at low
567 resolution; synthetic aperture radar; and hydrological models). Estimates by dynamic datasets are not directly
568 comparable to the static ones; thus, each is colored differently: red (dynamic) and black (static). Legend for dataset
569 types: OS: Optical Sensor; SAR: Synthetic Aperture Radar; HM: Hydrological Model; HR: multiple datasets at High
570 Resolution; CR: multiple datasets at Coarse Resolution.

571 Table 2. Basin-scale, long-term minimum and maximum inundation estimates for 18 datasets.

	Dataset	Minimum (km²)	Maximum (km²)
Multiple datasets at coarse resolution	GIEMS-2	45,800	486,600
	SWAMPS	157,400	491,100
	WAD2M	225,500	707,900
Multiple datasets at high resolution	GIEMS-D3	116,600	500,700
	CIFOR	-	872,700
	ESA-CCI	-	267,400
	GIEMS-D15	157,700	545,400
	GLWD	-	481,200

	SWAF-HR	53,200	630,900
Hydrological model	THMB	65,200	450,800
	CaMa-Flood	188,100	576,700
	MGB	83,600	600,900
Optical sensor	G3WBM	-	98,500
	GLAD	25,700	187,600
	GSWO	37,000	128,500
Synthetic Aperture Radar	Hess	284,200	633,500
	Chapman	91,200	506,400
	Rosenqvist	42,400	659,100

572

573 **3.2 How much inundation is estimated to occur in individual wetland regions?**

574 ***3.2.1 Overall assessment***

575 The 18 basin-scale inundation datasets were compared with the 11 subregional ones through
576 analysis of long-term means of annual maximum inundated areas (Table 3), long-term means of
577 annual minimum areas (Supplementary Table S3), and multiple comparison metrics
578 (Supplementary Table S4). The subregional datasets, covering individual wetland complexes, are
579 considered as independent validation datasets, given the ground validation performed for most of
580 them, as well as the use of a region-specific classification, and the often higher spatial resolution
581 (e.g., 12.5 m for some based on ALOS-PALSAR imagery).

582 The Amazon River floodplains (from Iquitos to Gurupá) and the Llanos de Moxos regions are the
583 largest Amazon wetland complexes: 106,800 ± 25,800 km² and 113,500 ± 53,400 km², respectively
584 when considering the three SAR-based datasets, and 94,100 ± 32,500 km² and 85,300 ± 52,400

585 km² when considering all 18 basin-scale datasets. Besides these two areas, the third largest
586 Amazon wetland region is Pacaya-Samiria, with 29,700 ± 20,600 km² (all datasets) and 40,000 ±
587 4,200 km² (SAR datasets).

588 The comparison of the long-term means of annual maximum and minimum observed inundation
589 over the available time periods indicates differences between basin-scale datasets and the
590 subregional validation datasets. Overall, the subregional datasets had a larger maximum inundation
591 extent than that estimated for the subregion from the basin-scale datasets. The underestimation by
592 the basin-scale ones varied from 49% for the Pacaya-Samiria region to 5% for the lower Amazon
593 River floodplain. Only three datasets overestimated the maximum extent of inundation: GIEMS-
594 D3, GIEMS-D15 and GLWD. The basin-scale, SAR-based ones (Hess, Chapman and Rosenqvist)
595 underestimated the maximum extent in the regions represented by all subregional datasets, except
596 Rosenqvist for Janauacá Lake, and Hess for the Llanos de Moxos region. This is likely related to
597 the higher resolution of many of the subregional datasets (e.g., 12.5 m original and 25 m final
598 resolution for the Uatumã ALOS-PALSAR classification by Resende et al., 2019), differences in
599 image acquisition period, and fine-tuning that may occur with dedicated processing for a particular
600 region.

601 To investigate the depiction seasonal patterns of inundation by the various datasets, we assessed
602 the correlation between the time series of absolute inundated areas from the dynamic ones and the
603 estimates for individual wetland complexes (Table S3). Overall, all datasets agreed well (average
604 Pearson correlation larger than 0.63 for the four wetland complexes with available time series),
605 showing a similar depiction of the inundation seasonality. However, their ability to monitor high-
606 resolution flood frequency is limited, as will be further discussed in section 4. A visual comparison
607 of the time series (Figure S6) shows agreement on seasonal timing of flooding and drainage, but

608 disagreement in the extent of inundation. In particular, two datasets have a small overall annual
609 amplitude (SWAMPS and WAD2M).

610 Overall, four datasets had the best overall representation of spatial patterns in inundation (Fit
611 metric; see Equation 1), as analyzed at 1 km pixel resolution, in comparison to the subregional
612 validation datasets: Hess, GLWD and the two hydrodynamic models (MGB and CaMa-Flood),
613 which were associated with average Fit metric between 0.64 and 0.67 (Table S3). While hydrologic
614 models such as MGB, CaMa-Flood and THMB have a satisfactory agreement basin wide, they are
615 unable to represent wetlands not primarily inundated by rivers (Fleischmann et al., 2020; Zhou et
616 al., 2021). For example, the Llanos de Moxos inundation is underestimated by both CaMa-Flood
617 and MGB with low Fit metric values (0.19-0.28; Table S3). This is expected for interfluvial
618 wetlands such as Llanos de Moxos and Roraima, where much of the flooding is caused by poor
619 drainage of local rainfall and tends to be shallower, as opposed to overflow of large rivers onto
620 adjacent floodplains. The four alternative subregional datasets assessed here - three hydrological
621 models (one for Curuai and two for Janauacá) and one classification of ALOS-PALSAR data for
622 the Llanos de Moxos area - were generally better or similar to some of the best-performing basin-
623 scale ones, as could be expected given their fine tuning for the specific areas, which often includes
624 local topographic surveys.

625 Some of the datasets merging multiple data sources overestimated the inundation area of individual
626 wetland complexes the most, especially GIEMS-D15, GIEMS-D3 and GLWD. Furthermore,
627 CIFOR was originally designed for peatland mapping in the tropics, and generally overestimates
628 inundation, suggesting a widespread distribution of wetlands along interfluvial terraces across the
629 whole basin that may include areas of poorly drained soils lacking surface water. For the individual
630 wetland complexes, however, CIFOR generally underestimated inundation and had a poor

representation of spatial patterns of inundation (low Fit metric). WAD2M underestimated the maximum inundation the most, which is understandable given its removal of open water areas and because its main inputs (CIFOR and SWAMPS) also underestimated inundated areas as indicated by the subregional validation datasets.

3.2.2 Individual inundation patterns based on SAR data

Regarding the maximum inundation extent, the Janauacá case provides a representative example to understand the differences among multiple L-band SAR datasets: these estimated total inundated area as 209 km², 184 km² and 446 km² for Hess, Chapman and Rosenqvist, respectively, in contrast to 404 km² with the subregional ALOS-PALSAR-based dataset (12.5 m resolution; Pinel et al., 2019). Part of these differences occur because of interannual variability, but other factors such as spatial resolution and algorithm differences seem relevant. Rosenqvist led to a more consistent estimation of the spatial inundation extent in terms of maximum inundation (Table 3) and inundation spatial patterns (Fit metric; Table S3), which can be a consequence of its higher spatial resolution (50 m) in contrast to the other two (90 m; Figure S3). Overall, Rosenqvist provided the largest inundation extent among SAR datasets across all areas along the Amazon mainstem floodplain, except for the Curuai floodplain and the savanna wetlands, as well as the closest agreement with subregional validation datasets (-9% ± 13%; average ± S.D.). Hess estimated the largest inundation area in the savanna wetlands (Llanos de Moxos, Roraima and Negro). However, Hess' estimate is 39% larger than the subregional validation dataset for Llanos de Moxos, while the other two SAR estimates are lower (-26% and -41% for Chapman and Rosenqvist, respectively).

One important question remains about the low-water period, as discussed in the previous section for the basin-scale analysis. Hess suggests much more inundation for this period for the Amazon mainstem floodplains (54,500 km²), mainly for the upstream forested reaches, and for the whole basin in general (284,200 km²), than recent estimates with ALOS (28,500 and 91,200 km²) and ALOS-2 data (19,500 and 42,400 km²). An assessment with the subregional datasets along the Amazon floodplain suggests that Hess overestimates the minimum extent for Curuai, Mamirauá and lower Amazon River, and is accurate for the Janauacá floodplain lake. Rosenqvist generally underestimates the minimum inundation. For instance, for the Mamirauá dataset, the minimum extent (i.e., permanently flooded areas) sums up to 715 km², which is increased to 1545 km² if considering all pixels flooded for more than 295 days per year. For this area, the SAR estimates are 1756 km² (Hess), 866 km² (Chapman) and 422 km² (Rosenqvist). Overall, this suggests that the actual value of minimum inundation across the central Amazon floodplains is somewhere between the Hess and Rosenqvist estimates.

3.2.3 Challenges over floodable savannas

Large discrepancies are observed for the Roraima and Negro floodable savannas. Roraima wetlands are small river floodplains interspersed with open savannas subject to flooding, which can be identified by optical data. In addition, the typical timing of high and low water in the Roraima region coincides approximately with the JERS-1 dual-season mosaics that were designed to reflect the seasonality of the central Amazon River floodplain (Hamilton et al. 2002). For these reasons, the JERS-1-based dataset by Hess et al. (2015) seems to satisfactorily represent most of the Roraima wetlands. However, it misses some small-scale riparian forests, given its 90 m spatial resolution and snapshot coverage that likely missed flooding events on smaller, flashier rivers

(Figure S5). Thus, the maximum inundation is likely higher than the Hess estimate (8,900 km²), which in turn is larger than the other ones based on SAR (1,900 - 4,100 km²). The only dataset to estimate a higher value is the coarse SWAF-HR (18,100 km²), which is similar to the value previously estimated by Hamilton et al. (2002) (16,500 km²), also with coarse data (SMMR passive microwave), though a part of the discrepancy may be due to interannual variability. More studies are necessary for this area to understand its actual inundation extent and dynamics. Similarly, the inundation estimates in the Negro interfluvial savannas are subject to large uncertainty, with the long-term maximum inundation varying between 95 (GLWD) and 20,700 km² (CIFOR), considering all basin-scale datasets. SAR-based estimates were between 5,900 and 15,800 km². In contrast, for the Pacaya-Samiria interfluvial area, which includes a large complex of forested wetlands, peatlands and palm swamps, the discrepancies are smaller than for the savanna interfluvial regions, although still considerable. The basin-scale SAR ranged between 24,000 km² (Chapman) and 56,200 km² (Rosenqvist), with the subregional validation dataset yielding 57,900 km². The good agreement between Rosenqvist and the subregional dataset was already reported by Rosenqvist et al. (2020).

Table 3. Long-term maximum inundation areas (km²) for the 11 wetland complexes (up to three subregional datasets per complex) and the 18 basin-scale datasets. The subregional values refer to the following datasets, in this order (comma-separated values relate to areas with more than one dataset available): Curuai - ALOS (Arnesen et al., 2013) and LISFLOOD-FP model (Rudorff et al., 2014); Uatumã - ALOS (Resende et al., 2019); Janauacá - ALOS (Pinel et al,. 2019), hydrologic model (Bonnet et al., 2017) and TELEMAC-2D model (Pinel et al., 2019); Mamirauá - ALOS (Ferreira-Ferreira et al., 2015); Pacaya-Samiria - ALOS-2 PALSAR-2 (Jensen et al., 2020); Llanos de Moxos - MODIS (Ovando et al., 2016) and ALOS (Ovando et al., 2016); and Lower Amazon River - MODIS (Park et al.,

2019). Average, standard deviation (S.D.) and coefficient of variation (CV) are presented for each area in the last rows.

	Dataset	Curuai	Uatumã	Janauacá	Mamirauá	Pacaya-Samiria	Llanos de Moxos	Lower Amazon	Amazon mainstem	Purus	Roraima savannas	Negro savannas
	Subregional	4162, 3720	1471	404, 336, 176	4476	57913	125422, 133470	56722	-	-	-	-
Multiple datasets at coarse resolution	GIEMS-2	3080	984	623	3344	23344	156176	79871	116379	7208	7173	12237
	SWAMPS	3359	722	280	1131	9929	88753	58626	72468	5618	4970	8819
	WAD2M	681	243	166	888	42635	102780	29276	49261	6698	3173	15450
Multiple datasets at high resolution	GIEMS-D3	4643	2732	505	3569	11562	150285	92908	127552	9045	12355	15123
	CIFOR	3796	994	177	1714	52590	116201	43509	86301	10844	3728	20712
	ESA-CCI	3236	855	260	3045	28727	39795	37475	84803	8883	510	12623
	GIEMS-D15	4635	2681	416	2444	44536	117979	86123	127150	11186	8129	14854
	GLWD	4275	2267	535	4259	79124	40661	67746	140921	14840	1048	95
	SWAF-HR	4439	2199	388	3205	16900	159712	69539	110468	10785	18146	15375
Hydrological model	THMB	2883	554	164	2840	27748	52693	39193	89658	19733	4307	3640
	CaMa-Flood	4246	1613	534	3208	34096	80725	63963	118577	20947	3454	6560
	MGB	4098	1549	474	3750	33344	21757	61997	115047	20394	240	3224
Optical sensors	G3WBM	2732	628	135	795	2694	9564	27451	37718	2351	352	1238
	GLAD	3479	832	204	1141	4196	38897	36930	53121	3903	3495	3885
	GSWO	3163	675	150	962	3637	19240	31191	44731	2982	1442	1880
Synthetic Aperture Radar	Chapman	2796	934	184	2694	24001	73710	39677	77632	12499	4077	5935
	Hess	3996	1045	209	3985	39741	174198	52156	115822	15155	8950	15758
	Rosenqvist	3055	1238	446	4362	56160	92693	55262	126806	20738	1867	9935
	Average	3477	1264	325	2630	29720	85323	54050	94134	11323	4856	9297
	S.D.	949	748	163	1226	20591	52387	19956	32503	6185	4666	6201
	CV	27%	59%	50%	47%	69%	61%	37%	35%	55%	96%	67%

3.3 How much do the datasets agree on the spatial distribution of inundation?

Agreement maps of the high resolution datasets (≤ 1 km spatial resolution) were developed for both long-term maximum (14 datasets available) and minimum inundation areas (10 datasets), based on the number of inundation datasets coinciding over a 1 km pixel (Figures 7 and 8 and their categorization for specific regions in Figure 9). Overall, 31% of the Amazon lowlands area (i.e.,

707 1.59 x 10^6 km² out of 5.11 x 10^6 km²) has been estimated as subject to inundation by at least one
708 dataset (bottom left panel, Figure 7). Based on the agreement between two datasets, this value
709 decreases to 948,300 km², which is larger than the value estimated when there is agreement among
710 four datasets (553,200 km²). This latter estimate is more similar to the average maximum
711 inundation as estimated by the ensemble of datasets (559,300 km²) and the three SAR-based ones
712 (599,700 km²). Furthermore, there is a lower agreement for the minimum inundation than for the
713 maximum inundation among individual regions (Figure 9).

714 For specific regions, a high degree of agreement for floodplains dominated by open water areas is
715 evident for the lower Amazon River reaches, followed by the forested floodplains fringing large
716 rivers, especially along the Amazon mainstem, Purus and Negro rivers. The generally higher
717 accuracies over central Amazon floodplains may also be related to the attention that dataset
718 developers have devoted to it, in contrast to other regions. Furthermore, the maximum floodplain
719 extent can be somewhat delineated with terrain elevation data (i.e., DEMs) using algorithms such
720 as HAND (Rennó et al., 2008), which helps to explain the relatively small disagreement for
721 floodplains fringing the largest rivers, and is particularly effective with vegetation bias-removed
722 DEMs (O'Loughlin et al., 2016; Yamazaki et al., 2017). The best agreement (for both maximum
723 and minimum inundation extent) occurred over the Curuai floodplain along the lower Amazon
724 mainstem, with 37% of its area being estimated as subject to inundation by all 14 datasets (Figure
725 9a). An agreement among all 14 datasets occurred, in part (i.e., more than 10% of the wetland
726 area), for the central Amazon floodplains (Curuai, Uatumã, Janauacá and lower Amazon River)
727 because of their relatively large fractions of open water areas.

728 In the interfluvial wetlands (Negro and Roraima savannas, Pacaya-Samiria and Llanos de Moxos),
729 the inundation patterns are less dependent on riverine overflow and more dependent on local

730 rainfall, making them less predictable (Hess et al., 2003). The disagreement for both maximum
731 and minimum inundation area is the largest across all regions, e.g., 65–78% of their flooded areas
732 were mapped by only one model for the minimum inundation (Figure 9b). The Llanos de Moxos
733 is conspicuous as a region of particular disagreement, perhaps because flooding is mainly shallow
734 and in vegetated areas (mainly savannas/grasslands), and is highly variable from year to year. In
735 general, the smaller the flooded patches the higher the challenge to map them, not only because of
736 resolution but also due to small-scale variation in topography. Similar disagreement occurred in
737 other interfluvial wetlands such as the Negro and Roraima savannas, and would be expected
738 elsewhere in savanna floodplains of South America (e.g., Pantanal, Llanos de Orinoco and Bananal
739 Island; Hamilton et al., 2002). The poor agreement over interfluvial areas, however, may also
740 partly reflect the longer history of study of Amazon mainstem floodplains, for which there are
741 river gage records that reflect floodplain water levels and inundation, while more remote areas
742 such as the Negro savannas and Pacaya-Samiria regions are more challenging to represent with a
743 few gages, and have received less attention. The challenges in estimating inundation over
744 interfluvial areas also affect the SAR-based datasets, which disagreed the most over these regions
745 (see section 3.5 and discussion in Rosenqvist et al., 2020).

746

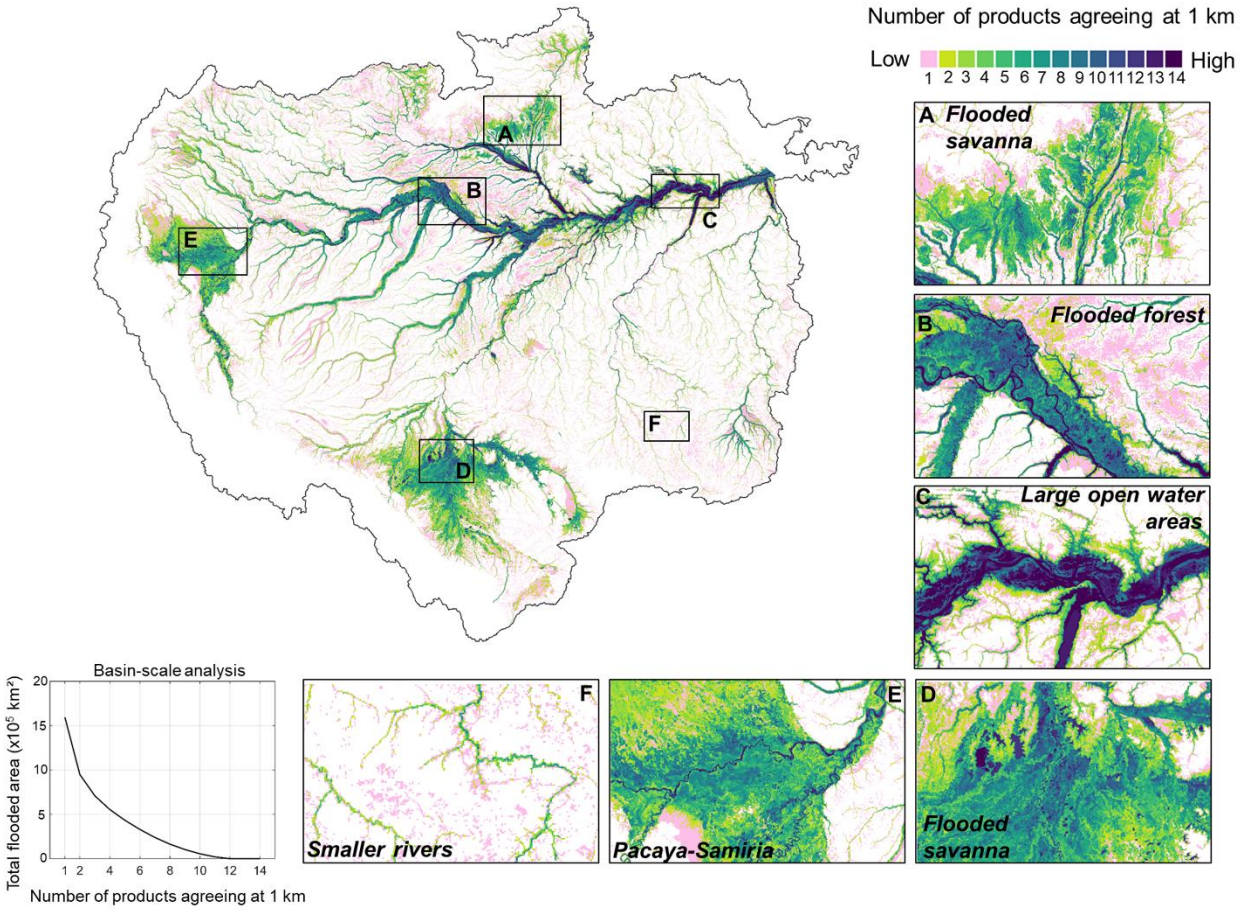

747

748 Figure 7. Agreement for maximum inundation area among 14 basin-scale datasets at high resolution (≤1 km spatial
749 resolution): G3WBM, ESA-CCI, GLAD, GSWO, GLWD, CIFOR, GIEMS-D15, GIEMS-D3, Chapman, Hess,
750 Rosenqvist, SWAF-HR, CaMa-Flood and MGB. A given pixel of a dataset with resolution higher than 1 km that had
751 more than 50% of flooding at the maximum inundation extent is classified as inundated.

752

753

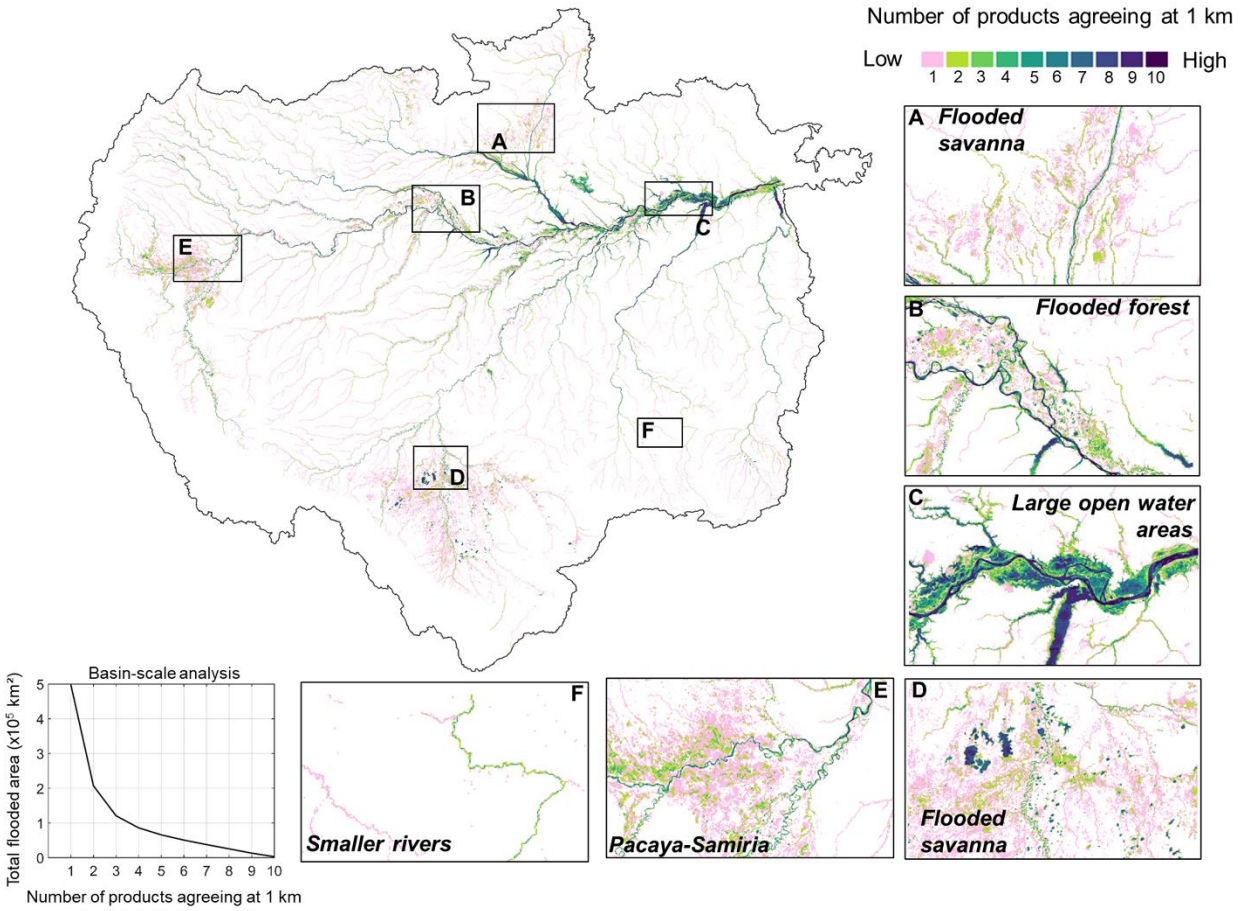

Figure 8. Agreement for minimum inundation area among 10 basin-scale datasets at high resolution (≤1 km spatial resolution): GIEMS-D15, Chapman, Hess, Rosenqvist, SWAF-HR, CaMa-Flood, MGB, GIEMS-D3, GSWO and GLAD. A given pixel of a dataset with resolution higher than 1 km that had more than 50% of flooding at the minimum inundation extent is classified as inundated.

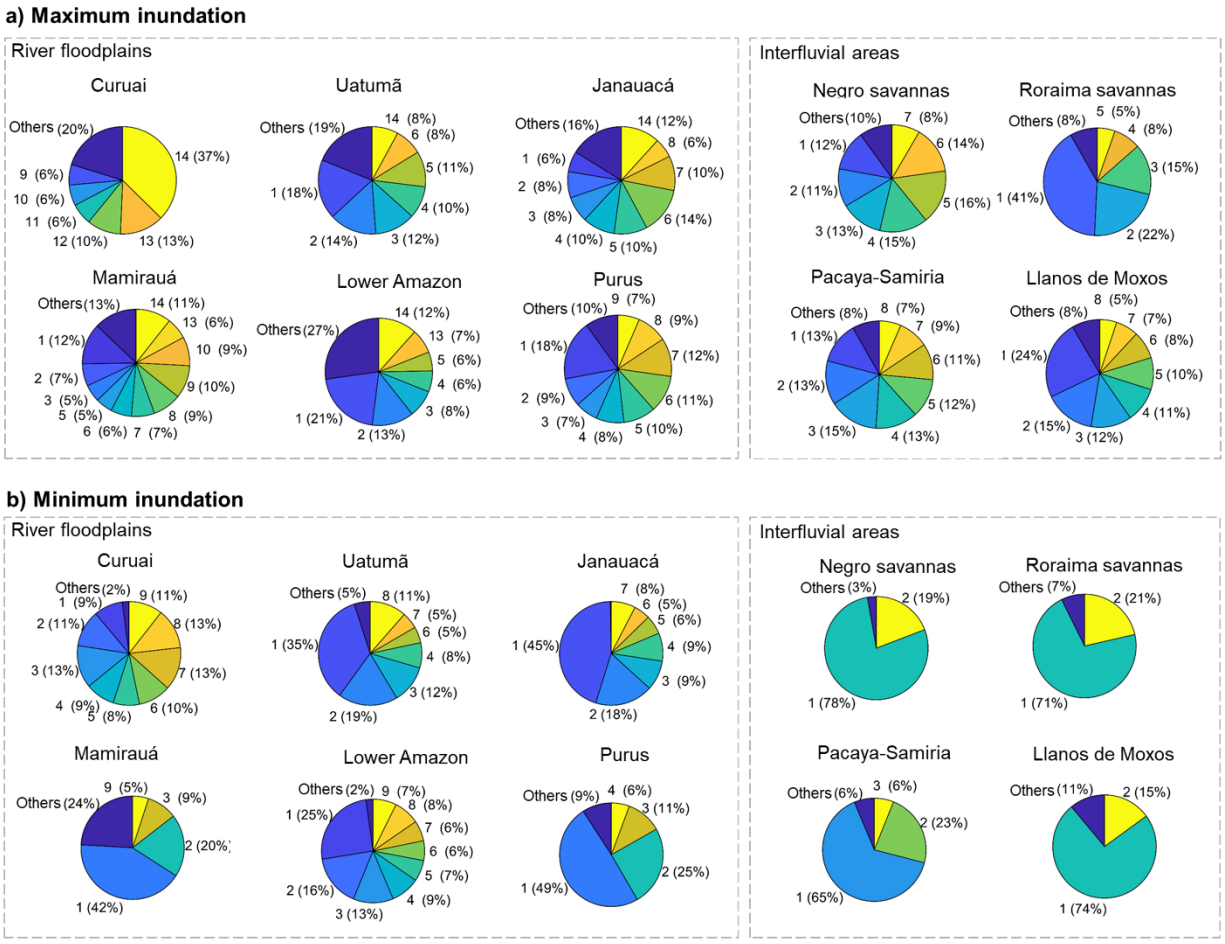

761

762 Figure 9. Degree of agreement for (a) maximum and (b) minimum inundation area for 10 individual wetland
763 complexes, based on the 1 km agreement map (Figures 7 and 8). The percentage values indicate the fraction of each
764 area where a given number of datasets agreed that it was flooded, e.g., 14 models agreed that 37% of the Curuai area
765 was flooded in the maximum inundation extent. The class with number 1 indicates the fraction of the area that only
766 one dataset estimated as being inundated. The class "others" refers to all classes that had less than 5% of pixels
767 estimated as being inundated.

768

769 **3.4 Quantifying the inundation extent of different wetland types**

Amazon wetlands include a myriad of ecosystems varying in geomorphology, hydrology, and vegetation cover. The classification system proposed by Junk et al. (2011) differentiated Amazon wetlands according to amplitude and range of water level change. Wetland types ranged from the forested swamps with stable water levels to river floodplains with oscillating water levels, and to interfluvial areas with small seasonal water level amplitude due to the main contribution of local rainfall and runoff (Fleischmann et al., 2020; Junk et al., 2011; Ovando et al., 2018).

A simpler yet hydrologically meaningful classification is the categorization into river floodplains and interfluvial wetlands adopted here, since the former typically have a greater hydrological connection to the main river and thus are subject to a different control of inundation area by river levels (Reis et al., 2019a). We performed a quantitative analysis of the inundation area in these two main hydrological classes. All pixels considered flooded by at least two datasets, based on the 1 km agreement map for maximum inundation extent (Figure 7), are presented in Figure 10. Overall, the medium to large river floodplains (upstream drainage area > 1000 km²) have a larger inundation extent than the category with small floodplains and interfluvial areas. An average total area subject to inundation of 317,800 ± 84,400 km² (average ± S.D.; median equal to 323,700 km²) was obtained for the medium to large floodplains, not including the optical and land cover datasets (G3WBM, GLAD, GSWO and ESA-CCI). A greater area for large floodplains was estimated by all except for CIFOR, SWAMPS and WAD2M. Two datasets estimated a similar value between the two classes (Chapman and GIEMS-2), which may be related to an overestimation of basin-scale isolated flooded patches.

Large floodplains fringing the main rivers, especially along the Amazon River, have been largely addressed by previous studies (Table 1 and Table S1). However, large river floodplains are also present in less studied reaches, e.g., in the upper Napo and Içá rivers in northwest Amazon basin,

and upper Xingu in the southeastern portion (see location in Figure 1). These upper reaches are subject to more sporadic, flashy river hydrological regimes (Hamilton et al., 2007), which make their inundation area difficult to map with current datasets of relatively low temporal resolution. In our analysis, the non-floodplain areas include mainly the large interfluvial areas (black rectangles in Figure 10), small river floodplains that are challenging to detect with currently available datasets, and some reservoirs, such as Balbina reservoir on the Uatumã River.

Besides the central Amazon floodplains, which have been widely studied, other wetland complexes require more attention, such as the Negro and Roraima savannas; the latter was only assessed by a single study to our knowledge (Hamilton et al., 2002). The inundation mapping of the Pacaya-Samiria region in the upper Amazon has received scientific attention recently (Jensen et al., 2018; Rodriguez-Alvarez et al., 2019), partially because of the region's role as a carbon sink via formation of peat (Draper et al., 2014; Lähteenoja et al., 2012). Regarding open water areas, Melack (2016) reported values ranging from 64,800 km² (Melack and Hess, 2010) to 72,000 km² (SRTM Water Body Data) and 92,000 km² (Hansen et al., 2013) for the Amazon basin (< 500 m in elevation). The three Landsat-based datasets assessed here, which are mainly capable of detecting open water areas, estimate 98,500 km² (G3WBM), 128,500 km (GSWO) and 187,600 km² (GLAD).

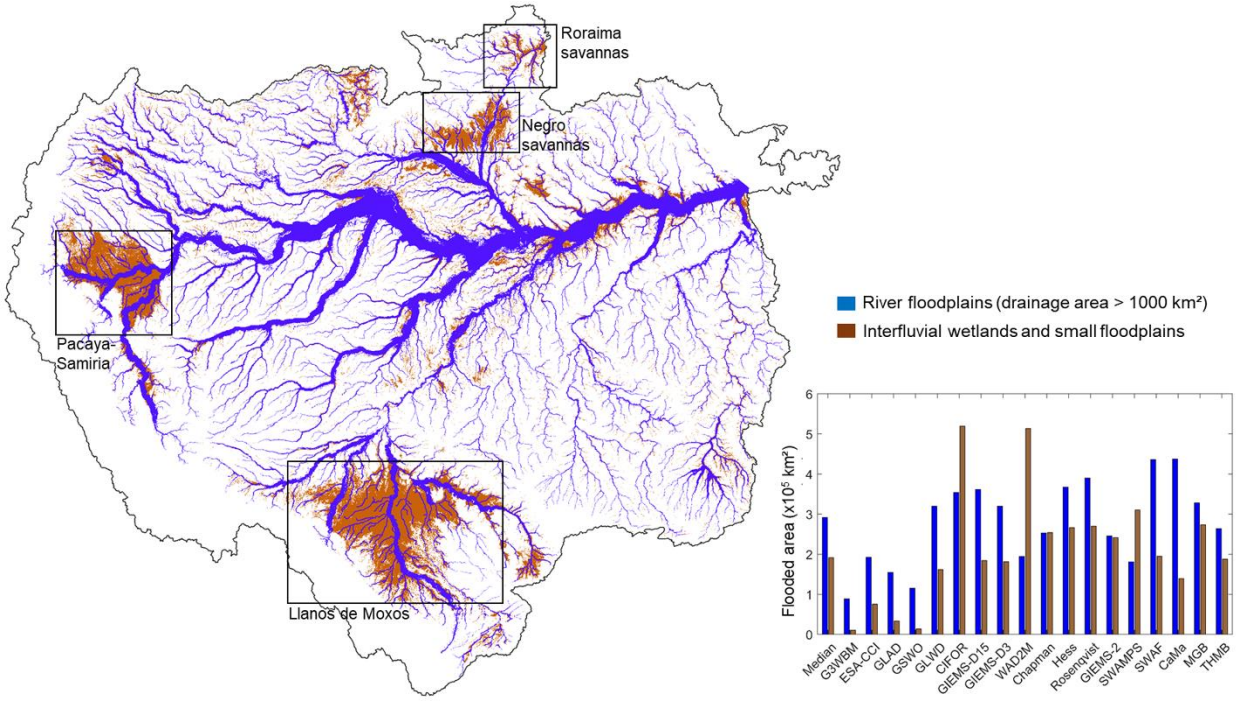

811

812 Figure 10. Quantification of maximum inundated areas over river floodplains with drainage area larger than 1,000
813 km², and interfluvial wetlands and small floodplains (area < 1,000 km²) within the Amazon basin. The maximum
814 inundation map depicts all 1 km pixels with at least two datasets agreeing (i.e., a reclassification of Fig. 7), in order to
815 avoid overestimation caused by pixels with only one dataset classifying them as subject to inundation. The four large
816 areas of interfluvial wetlands are highlighted with black rectangles (Pacaya-Samiria, Llanos de Moxos, Negro and
817 Roraima savannas).

818

819 **3.5 Limitations in comparing the inundation area datasets**

820 Some of the differences in large-scale inundation mapping highlighted by our comparison occur
821 because distinct datasets map temporal variation in inundation in different ways, varying for
822 example in sensor type, post processing, and spatial resolution. Figure 11 shows the agreement
823 maps for maximum inundation for four classes of datasets, considering the 14 basin-scale high-

resolution datasets. Those based on multiple datasets (GLWD, CIFOR, GIEMS-D3, GIEMS-D15, SWAF-HR) have the best agreement for the Llanos de Moxos area, and to a smaller degree, for Pacaya-Samiria, Negro and Roraima wetlands. The L-band SAR datasets have less overall agreement (Figure 11c), while the optical data are mainly applicable to open water areas in the Amazon mainstem floodplain (Figure 11b). The 1D hydrological models cannot represent interfluvial wetlands where flooding is not controlled by river level and discharge (Figure 11d).

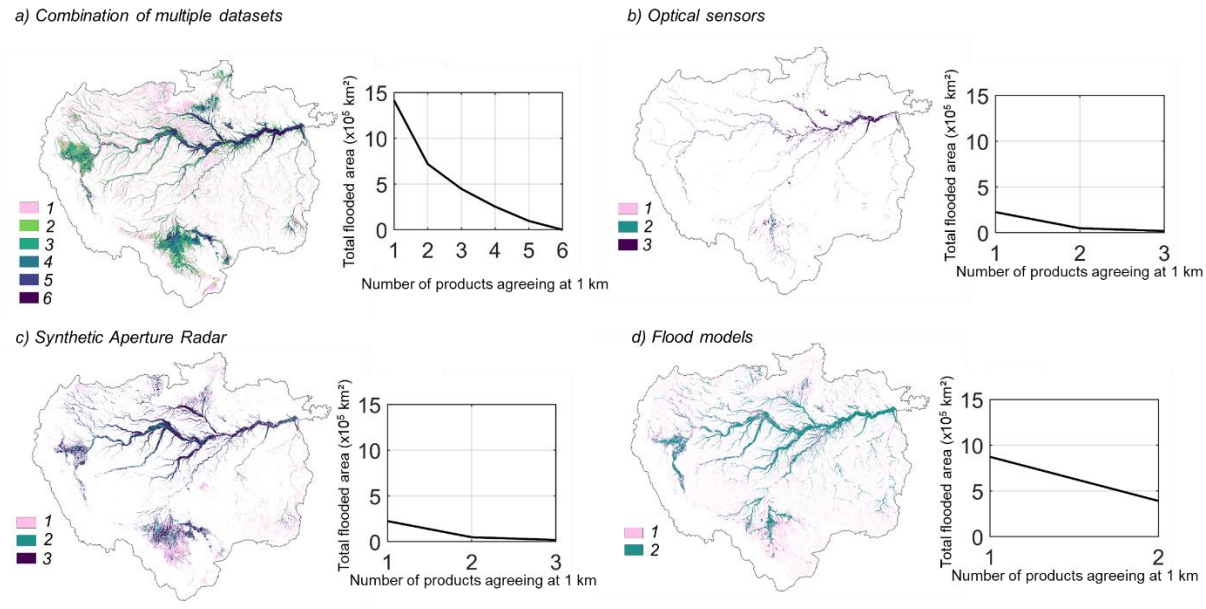

Figure 11. Amazon basin (< 500 m elevation) agreement maps at 1 km resolution, for maximum inundation and for each type of dataset, considering only the high-resolution datasets (≤ 1 km spatial resolution): (a) six datasets based on merging of multiple datasets (GLWD, CIFOR, GIEMS-D3, GIEMS-D15, SWAF-HR, ESA-CCI), (b) three datasets based on optical sensors (G3WBM, GLAD, GSWO), (c) three datasets based on synthetic aperture radar (Hess, Chapman, Rosenqvist), and (d) two hydrological models (MGB and CaMa-Flood). The right column graphs present the total inundation area in the Amazon basin for a given number of datasets agreeing, e.g., the basin area where the two hydrological models (Fig. d) agree to be flooded is 390,900 km².

The different methodologies used to produce each dataset complicate their direct comparison (Rosenqvist et al., 2020), and some methodological differences produce systematic differences and bias among the data sources included in our comparison. Here we used datasets covering long-term dynamics (e.g., GIEMS or hydrologic models), short-term dual-season (e.g., Rosenqvist, spanning four years), and a particular year (e.g., Hess). Some datasets use alternative approaches to derive long-term maximum inundation area, such as GIEMS-D15, which generated estimates by merging 3-year moving-window maximum values of GIEMS with the GLWD dataset. Therefore, a comparison of all these datasets must be performed with consideration of their methodology. For instance, the comparison of dual-season datasets against monthly datasets can yield erroneous conclusions, although it has been a common practice to directly compare such datasets. Some datasets also consider a "high-water assumption" (Ferreira-Ferreira et al., 2015; Hess et al., 2003), whereby the high-water maps are forced to contain all flooded pixels from the low-water map.

In addition to methodological differences, each dataset was developed for different periods (Table 1), and thus interannual and seasonal variability accounts for some of the differences among them. To address this, we performed an annual analysis (Figure 5), which suggests that the long-term inundation estimate is fairly stable for each dataset despite some interannual differences. In fact, the temporal variability of each dataset is generally smaller than the differences in comparison with the other estimates. However, the Amazon hydrological cycle has been shifting over decades (Barichivich et al., 2018; Gloor et al., 2013), and a recent increase in maximum water levels in the central Amazon suggests a new hydroclimatic state (Espinoza et al., 2019). Some wetlands have also been subject to forest loss, and so the detectability of inundation by remote sensing may have increased over time, e.g., major deforestation has occurred along the lower Amazon River

floodplain (Renó et al., 2011). Similarly, widespread burning might be converting black-water floodplain forests into savanna vegetation (Flores and Holmgren, 2021). In addition, in some regions, such as the southern Amazon, an increase in the dry-season length has been observed, which is a major climatic constraint for forest sustainability (Fu et al. 2013; Staver et al., 2011). However, analyzing long-term change in inundation patterns is beyond the scope of this study, and thus we assumed stationarity in our comparison framework.

Another important challenge is to find a common definition of wetlands among datasets. Here we focused on inundation extent, however some datasets (e.g., CIFOR) represent peatland locations instead of inundated areas, although their areas of peat formation often include inundated areas. Estimates based on SAR or passive microwave emission may also be sensitive to saturated soil without standing water above it, and thus the observed inundation estimates can have some ambiguity. Hydrologic models provide simulated surface water extent, and we mapped inundation accounting for pixels with water depth greater than zero. While hydrologic models have uncertainties related to model structure (e.g., inadequate representation of inundation processes), input data (e.g., DEM and climate forcing) and parameterization (e.g., soil water capacity and river channel width and depth; assumptions of level water surfaces between rivers and their floodplains), remote sensing-based datasets have uncertainties related to spatial and temporal resolutions (e.g., coarse spatial resolution not capable of detecting small patches), and detection uncertainty (e.g., dense vegetation canopies can obscure passive microwave emission from underlying surfaces). Thus, a comparative framework provides an opportunity to highlight and stress the uncertainties and limitations of each dataset.

Hydrologic models currently available at the Amazon basin scale are one-dimensional, and thus are capable of simulating flooding mainly along river floodplains, as corroborated by various

validation exercises in the Amazon that have relied on the Hess, GIEMS and SWAF-HR datasets (Fleischmann et al., 2020; Luo et al., 2017; Paiva et al., 2013; Zhou et al., 2021). These models are also largely dependent upon accurate DEMs, which are still challenging to obtain over tropical forested floodplains. Furthermore, given that a 500 m elevation mask (Amazon lowlands) has been used for some SAR datasets (Hess et al., 2015), and the difficulty of some radar and passive microwave ones to detect inundation at high elevations due to slope and snow effects, for instance (Parrens et al., 2017), we have adopted the same 500 m threshold in our lowland mask to improve the comparability among datasets. However, even though higher elevation wetlands amount to much less total area compared to lowland wetlands, understanding their flooding dynamics is important for some parts of the Amazon basin. Although some datasets, especially the hydrological models (MGB, CaMa-Flood and THMB), are capable of estimating inundation in higher elevation parts of the basin, in this case uncertainties may also be large given errors in precipitation (low density of in situ gauges and high rainfall spatial heterogeneity) and thus runoff fields over mountainous areas, as well as the tendency for river flows to vary over short time scales (Espinoza Villar et al., 2009; Zubieta et al., 2015). Furthermore, the availability of in situ river discharge measurements for model calibration and validation is lower in the Andean Amazon (Feng et al., 2020; Wongchuig et al., 2019; Zubieta et al., 2017).

Our analyses were performed at 1 km resolution and at regional scales, which avoids geolocation problems that affect analyses at higher resolutions (e.g., 30 or 90 m). Small disagreements among our estimates and the values presented in the original publications may also arise from the use of the WGS84 datum with a geographical coordinate system for all datasets (except for SWAMPS which was provided in the EASE-Grid format). Also, the coarse-resolution datasets, especially GIEMS-2 and SWAMPS with 25 km spatial resolution, can be difficult to compare with estimates

for individual wetland complexes (e.g., Curuai and Janauacá), since only a few 25-km pixels may be located within the wetland boundaries.

The quantification of inundation over larger river floodplains (Figure 10) is also subject to uncertainties. The maximum floodplain lateral extent was estimated based on an automatic buffer procedure around the Hydrosheds drainage network, further manually edited by considering the three SAR-based, basin-scale datasets and the MERIT DEM-based topography. Although it captures the basin-scale geomorphological differences along major floodplains, some uncertainties remain regarding the true lateral extent for areas where rain-fed savanna floodplains are present (e.g., Llanos de Moxos, Roraima), and where flooding extend far from the main rivers (e.g., Pacaya-Samiria). For these areas in particular, we assumed buffer values similar to adjacent upstream and downstream floodplains (e.g., the Amazon River downstream of Pacaya-Samiria), which is reasonable but should undergo future scrutiny, including local ground-based surveys.

4. Perspectives and recommendations

Considerable advances have been achieved in recent decades in the mapping of inundation extent across the Amazon basin. Here, we have presented an analysis of 29 inundation datasets for the basin, covering multiple scales, spatial and temporal resolutions, and data sources. We showed that large discrepancies persist, and this is especially true at local scales. Below we present some perspectives and recommendations for future development of inundation mapping in the world's largest river basin.

4.1 Which are the most reliable data sources for inundation mapping in the Amazon River basin?

At basin scale, the Rosenqvist ALOS-2 PALSAR-2 dataset is available at 50 m, and shows a good overall agreement with the 90 m Hess one over the large river floodplains, while the latter seems more accurate for interfluvial savanna floodplains (e.g., Negro and Roraima). The high agreement is observed mainly for the maximum inundation estimates, while for the minimum inundation area, important disagreements persist and more studies should be performed to understand them. Overall, the Hess' dataset has been the Amazon inundation benchmark for many years, and still provides satisfactory estimates. Detection of inundation by L-band SAR has a sound theoretical and empirical basis that has been validated for the Amazon (Rosenqvist et al., 2002; Hess et al., 2003). Optical datasets with resolution higher than 30 m are available, but detection of inundation is restricted to non-vegetated wetlands and clear-sky periods, and is most applicable in the lower Amazon River floodplains. ALOS-PALSAR at 12.5 m resolution and Sentinel SAR at 10 m resolution (with C-band and limited vegetation penetration) can be applied to specific regions. Time series of these datasets can estimate seasonal variations in inundation, but are limited by the length of the acquisitions. Weekly to monthly, spatially coarser data (25 km) are available from passive microwave-based datasets such as GIEMS, SWAF and SWAMPS. Downscaling techniques have improved their spatial resolution to 90 m (GIEMS-D3) and 1 km (SWAF-HR). Hydrological models (e.g., CaMa-Flood and MGB) are capable of accurately estimating inundation over river floodplains, and at high temporal resolution depending on the input rainfall data (e.g., hourly to daily). However, they are still limited over interfluvial wetlands with less

950 connection with rivers, unless they are upgraded for simulating 2D inundation processes and
951 complex floodplain flow paths (Fleischmann et al., 2020; Yamazaki et al., 2014).

952

953 ***4.2 What are the current capabilities of flood frequency mapping?***

954 At the basin scale, high-resolution, long-term average flood frequency can be estimated by four of
955 the datasets analyzed here (GIEMS-D3, SWAF-HR, MGB and CaMa-Flood), with spatial
956 resolutions ranging from 90 m to 1 km. Although multiple SAR data are currently available (e.g.,
957 Sentinel-1, ALOS-PALSAR and ALOS-2 PALSAR-2), they have a limited temporal resolution,
958 and we still do not have a flood frequency dataset of higher spatial resolution (i.e., better than 90
959 m) for the whole basin based on SAR. The discrepancies among the available datasets are notable
960 (Figure 12). The average of the basin-scale flood frequency shows a higher agreement for areas
961 with high flood frequency along the lower Amazon River (Figure 12a). These are associated with
962 a high proportion of open water areas, and have lower uncertainty (Figure 12b). Generally, there
963 is a smaller variation along floodplains bordering the major rivers (except for their fringes) than in
964 interfluvial areas, especially in the Negro and Roraima wetlands (Figure 12b). Detailed inundation
965 mapping for the Mamirauá Sustainable Development Reserve in the Amazon mainstem floodplain
966 (Figure 12c) reinforces the challenges for mapping local spatio-temporal inundation dynamics.
967 The northern part of the Mamirauá reserve has a shorter flood frequency in all datasets, while three
968 of them (SWAF-HR, GIEMS-D3, CaMa-Flood) estimate that large portions are never flooded. For
969 the southern part, there is some convergence for areas that are frequently flooded.

970

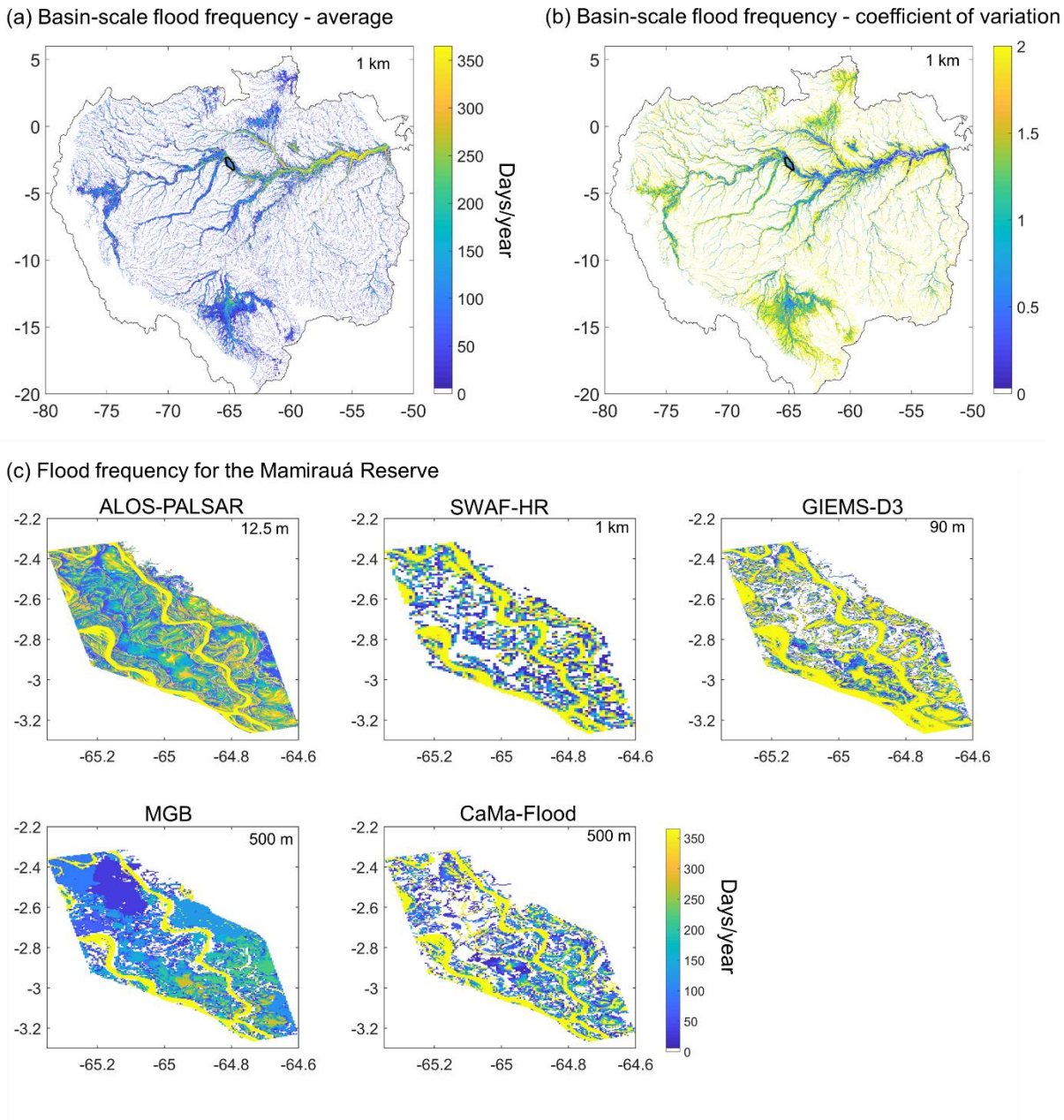

971

972 Figure 12. Analysis of flood frequency for (a) basin-scale average and (b) coefficient of variation of the long-term
973 flood frequency estimated from four high-resolution dynamic datasets (GIEMS-D3, SWAF-HR, CaMa-Flood and
974 MGB). (c) The four basin-scale datasets are compared to a subregional validation dataset (i.e., the ALOS-PALSAR-
975 based classification by Ferreira-Ferreira et al. (2015), displayed in the top left panel) for the Mamirauá Sustainable
976 Development Reserve along the central Amazon River mainstem (location shown by black outline in figure a).

977

4.3 Implications for biogeochemistry, ecology and flood management

The divergent estimates of Amazon inundation extent have major implications for the quantification of the role of wetlands in global biogeochemical cycles, ecosystem processes and natural disaster management.

First, different datasets have been used to quantify the role of Amazon wetlands in the carbon cycle (Guilhen et al., 2020; Melack et al., 2004; Richey et al., 2002; Saunois et al., 2020). An intercomparison assessment of global models forced with different inundation datasets for the Amazon could provide insights into their sensitivity to the estimated inundation. This would be particularly important for modeled estimates of methane flux, given the region's significant contribution to global methane emissions from natural wetlands (Basso et al., 2021). Furthermore, for a proper estimation of methane and carbon dioxide fluxes, dynamic inundation estimates are necessary; this study shows that most coarse-resolution dynamic datasets capture relatively well the seasonality (i.e., the timing of high and low water periods) of annual flooding at a large scale (but not at the local scales), but the magnitude of inundation area over time is still associated with significant errors (Fig. S6).

The understanding of the ecology of Amazon freshwaters has benefited from advances in remote sensing-based mapping of inundation. Hydrological variables of interest in relation to wildlife (Alvarenga et al., 2018; Bodmer et al., 2018) and vegetation distribution (Hess et al., 2015, 2003) include hydroperiod, floodplain water depth (Arantes et al., 2013; Fassoni-Andrade et al., 2020), and (lateral) surface water connectivity (Castello, 2008; Duponchelle et al., 2021; Reis et al., 2019a, 2019b), and should be better estimated by future datasets. In addition, many wetland ecosystem studies are performed at the tree stand level (e.g., floristic inventories) and require high

spatial resolution inundation estimates to perform meaningful spatial analyses accounting for spatial heterogeneity of wetland vegetation. Furthermore, besides a simple interfluvial/floodplain categorization of wetlands as performed here (section 3.4), which is reasonable from a hydrologic perspective, improving our understanding of the ecology of Amazon freshwater systems requires accurate mapping of habitats and their diverse vegetation types (e.g., grasslands, particular monodominant tree species, herbaceous plants). For instance, floodplain forest cover has been positively correlated to fishery yields (Arantes et al., 2018) and fish abundance (Lobón-Cerviá et al., 2015). While this wetland habitat mapping has already been done by some initiatives at the basin (Hess et al., 2015, 2003) and subregional scales (Ferreira-Ferreira et al., 2015; Silva et al., 2013), there is still a need for higher resolution and dynamic datasets.

Regarding flood monitoring in the context of natural hazard management, the flood warning systems of regional water authorities in the basin provide information based on river discharge and water level at monitoring stations (e.g., Brazil's Geological Survey SACE system; <http://sace.cprm.gov.br/amazonas/#>). In addition, there are other available monitoring and forecasting services that have been developed for the global scale, such as the Global Flood Detection System (https://www.gdacs.org/flooddetection/), based on remote sensing, and the Global Flood Monitoring System (http://flood.umd.edu/) and the Global Flood Awareness System (https://www.globalfloods.eu/), based on hydrological modeling. The currently available, basin-scale inundation datasets are unable to map flood hazard at the detailed resolution required for flood management applications, especially concerning urban areas (Almeida et al., 2018). High-resolution flood mapping has been achieved using hydraulic modeling based on local surveys of river bathymetry and floodplain LiDAR DTM, but only for a few specific sites such as the lower Madeira River (Fleischmann et al., 2021).

4.4 Future opportunities and recommendations

Future satellite missions will provide opportunities for improved inundation mapping in the Amazon, especially the polarimetric and interferometric L-band SAR data from the upcoming NASA/ISRO mission (NISAR), the P-Band BIOMASS mission from ESA, and the Ka-band Radar Interferometer (KaRIn) swath observations from the forthcoming SWOT mission (Biancamaria et al., 2016). New inundation detection technology under development with Global Navigation Satellite System-Reflectometry (GNSS-R), such as the Cyclone GNSS (CYGNSS) constellation of GNSS-R satellites, holds promise to provide higher frequency observations of water level changes (Jensen et al., 2018; Ruf et al., 2018; Rodriguez-Alvarez et al., 2019). Further studies with the ALOS-2 PALSAR-2 data also are promising, in order to achieve new dynamic inundation detection, as well as ongoing assessments of the accuracy of the newly available high temporal resolution inundation datasets (e.g., SWAF-HR with 3-day availability). Consistent and updated validation products of Amazon inundation are required, which could be derived from airborne, satellite, or UAV-based LiDAR surveys along multiple wetlands, in particular for overlooked wetlands such as the Negro and Roraima floodable savannas where measured water levels in rivers may not adequately predict inundation area. This is especially important for the minimum inundation extent, which showed large uncertainties among the multiple datasets.

Comprehensive comparisons among multiple inundation datasets are scarce in the literature, yet are valuable ways to understand benefits and limitations of each of them. A few examples include a continental-scale assessment of flood model hazard maps in Africa (Trigg et al., 2016) and regional assessment of inundation in floodplains of Nigeria and Mozambique (Bernhofen et al., 2018), both based on global hydrological models. Similar initiatives for other areas worldwide

would be welcome, especially for those that lack consistent flood mapping, such as the Congo and other large wetland systems in Africa (Papa et al., 2022). Furthermore, the combination and integration of multiple inundation datasets present a promising and effective approach (Gumbricht et al., 2017; Hu et al., 2017). We recommend that future developments include optimal data merging approaches, e.g., by integrating inundation extent into models accounting for water cycle components with multiple constraints (Meyer Oliveira et al, 2020; Pellet et al., 2021), and by considering new types of datasets (e.g., GNSS-R; Jensen et al., 2018). Bias of different datasets could be corrected based on intercomparisons such as those we present here. For instance, recent studies have performed inundation bias correction using the Hess dataset (Aires et al., 2013; Sorribas et al., 2016). However, merging of different datasets must be performed with caution, in a consistent way, avoiding double counting of surfaces, as well as missing others: its success critically depends upon a good understanding of the limitations and assets of each individual dataset. The optimal combination of hydrological-hydraulic models with satellite flood maps using techniques such as data assimilation is also a promising alternative at the basin scale (Wongchuig et al., 2020).

There is a need for the development of more large-scale 2D hydrological model applications, especially for large wetland complexes such as the Llanos de Moxos and Pacaya-Samiria, to better represent inundation dynamics (Fleischmann et al., 2020). 2D models have been applied mainly to some local-scale areas in the Amazon mainstem floodplain (Pinel et al., 2019; Rudorff et al., 2014; Trigg et al., 2009; Wilson et al., 2007). Furthermore, inundation anomalies are still poorly understood owing to the lack of ground-based inundation observations during extreme floods and droughts. Therefore, validation of estimates for extreme years has usually been performed with river water level data (in situ or from satellite altimetry) (Silva et al., 2018; Wongchuig et al.,

2019). Future works should address which datasets and methodologies are the most suitable for mapping extreme events. Furthermore, besides inundation extent, flood storage (Frappart et al., 2005; Papa et al., 2008; Schumann et al., 2016; Papa and Frappart, 2021) and water velocity (Pinel et al., 2019) are necessary hydraulic variables to properly address multiple environmental studies (e.g., flood monitoring, flood attenuation by floodplains, fish floodplain habitats), but to date have not been well studied in the Amazon.

Finally, there is a need for better-informed usage of the currently available inundation datasets by multiple local and regional stakeholders (e.g., local water authorities, national water agencies), as well as research communities not close to remote sensing groups. This will only be achieved through a two-way interaction with these actors and development of easy-to-access visualization platforms (i.e., investment in hydroinformatics), as well as training of regional/local user communities. To this end, we have developed a WebGIS platform (https://amazon-inundation.herokuapp.com/) to display and provide data acquisition links for the inundation datasets assessed here, which will be continuously updated once new datasets are made available. The interaction with local users would bring important feedback on the large-scale datasets as well, for instance through citizen science initiatives that are ongoing in the Amazon (https://www.amazoniacienciaciudadana.org/).

Acknowledgments

The authors thank Dr. Fernando Jaramillo, Dr. David Kaplan, Dr. David Marques and Dr. Naziano Filizola for fruitful comments in an earlier version of this manuscript. The work was part of the SABERES project financed by the BNPParibas Foundation as part of its "Climate & Biodiversity

Initiative" program 2019. A.S.F. was supported by CNPq (Conselho Nacional de Desenvolvimento Científico e Tecnológico, Brazil) [grant number 141161/2017-5]. F.P., J.F.F., M.P.B. and F.A. received support from CNES (SWOT-ST project SWOT for SOUTH AMERICA, ID: 6018-4500066497). F.P. and M.P.B. also received support from CNES (SWOT-ST project SWOT Wetlands Hydrology Monitoring). F.P. is supported by the IRD Groupement De Recherche International (GDRI) SCaHyLab. J.M.M. received support from NASA IDS grant NNX17AK49G and the US National Science Foundation (Division of Environmental Biology, grant 1753856). E.P. acknowledges Nanyang Technological University (SUG-NAP EP3/19) and Ministry of Education of Singapore (AcRF Tier1 RT 06/19 and AcRF Tier2 RT 11/21). A.F.R. acknowledges the Research Foundation of São Paulo (FAPESP, grant #2019/24049-5). S.W. has been supported by the French AMANECER-MOPGA project funded by ANR and IRD (ref. ANR-18-MPGA-0008). M.C. received funding from NASA IDS grant NNX17AK49G. The SWAF dataset development was financed by the CATDS and the SWOT-AVAL programs by CNES.

References

Abril, G., Martinez, J.M., Artigas, L.F., Moreira-Turcq, P., Benedetti, M.F., Vidal, L., Meziane, T., Kim, J.-H., Bernardes, M.C., Savoye, N., Deborde, J., Souza, E.L., Albéric, P., Landim de Souza, M.F., Roland, F., 2014. Amazon River carbon dioxide outgassing fuelled by wetlands. Nature 505, 395–398. https://doi.org/10.1038/nature12797

Aires, F., Miolane, L., Prigent, C., Pham, B., Fluet-Chouinard, E., Lehner, B., Papa, F., 2017. A Global Dynamic Long-Term Inundation Extent Dataset at High Spatial Resolution Derived through Downscaling of Satellite Observations. J. Hydrometeorol. 18, 1305–1325.

https://doi.org/10.1175/JHM-D-16-0155.1

Aires, F., Papa, F., Prigent, C., 2013. A Long-Term, High-Resolution Wetland Dataset over the Amazon Basin, Downscaled from a Multiwavelength Retrieval Using SAR Data. J. Hydrometeorol. 14, 594–607. https://doi.org/10.1175/JHM-D-12-093.1

Aires, F., Prigent, C., Fluet-Chouinard, E., Yamazaki, D., Papa, F., Lehner, B., 2018. Comparison of visible and multi-satellite global inundation datasets at high-spatial resolution. Remote Sens. Environ. 216, 427–441. https://doi.org/10.1016/j.rse.2018.06.015

Al Bitar, A., Parrens, M., Fatras, C., Luque, S. P., 2020. Global Weekly Inland Surface Water Dynamics from L-Band Microwave. In IGARSS 2020-2020 IEEE International Geoscience and Remote Sensing Symposium, 5089-5092.

Alsdorf, D., Bates, P., Melack, J., Wilson, M., Dunne, T., 2007. Spatial and temporal complexity of the Amazon flood measured from space. Geophys. Res. Lett. 34. https://doi.org/10.1029/2007GL029447

Alvarenga, G.C., Ramalho, E.E., Baccaro, F.B., da Rocha, D.G., Ferreira-Ferreira, J., Dineli Bobrowiec, P.E., 2018. Spatial patterns of medium and large size mammal assemblages in várzea and terra firme forests, Central Amazonia, Brazil. PLoS One 13, 1–19. https://doi.org/10.1371/journal.pone.0198120

Andrade, M.M.N. de, Bandeira, I.C.N., Fonseca, D.D.F., Bezerra, P.E.S., Andrade, Á. de S., Oliveira, R.S. de, 2017. Flood Risk Mapping in the Amazon, in: Flood Risk Management. InTech, p. 13. https://doi.org/10.5772/intechopen.68912

1134 Arantes, C.C., Castello, L., Cetra, M., Schilling, A., 2013. Environmental influences on the
1135 distribution of arapaima in Amazon floodplains. Environ. Biol. Fishes 96, 1257–1267.
1136 https://doi.org/10.1007/s10641-011-9917-9

1137 Arantes, C.C., Winemiller, K.O., Petrere, M., Castello, L., Hess, L.L., Freitas, C.E.C., 2018.
1138 Relationships between forest cover and fish diversity in the Amazon River floodplain. J.
1139 Appl. Ecol. 55, 386–395. https://doi.org/10.1111/1365-2664.12967

1140 Armijos, E., Crave, A., Espinoza, J.C., Filizola, N., Espinoza-Villar, R., Ayes, Fonseca, P.,
1141 Fraizy, P., Gutierrez, O., Vauchel, P., Camenen, B., Martiınez, J.M., Dos Santos, A.,
1142 Santini, W., Cochonneau, G., Guyot, J.L., 2020. Rainfall control on Amazon sediment flux:
1143 synthesis from 20 years of monitoring. Environ. Res. Commun. 2, 051008.
1144 https://doi.org/10.1088/2515-7620/ab9003

1145 Arnesen, A.S., Silva, T.S.F., Hess, L.L., Novo, E.M.L.M., Rudorff, C.M., Chapman, B.D.,
1146 McDonald, K.C., 2013. Monitoring flood extent in the lower Amazon River floodplain
1147 using ALOS/PALSAR ScanSAR images. Remote Sens. Environ. 130, 51–61.
1148 https://doi.org/10.1016/j.rse.2012.10.035

1149 Asner, G.P., 2001. Cloud cover in Landsat observations of the Brazilian Amazon. Int. J. Remote
1150 Sens. 22, 3855–3862. https://doi.org/10.1080/01431160010006926

1151 Balsamo, G., Beljaars, A., Scipal, K., Viterbo, P., van den Hurk, B., Hirschi, M., and Betts, A.
1152 K.: A Revised Hydrology for the ECMWF Model: Verification from Field Site to
1153 Terrestrial Water Storage and Impact in the Integrated Forecast System, J. Hydrometeorol.,
1154 10, 623–643, https://doi.org/10.1175/2008jhm1068.1, 2009.

Barichivich, J., Gloor, E., Peylin, P., Brienen, R.J.W., Schöngart, J., Espinoza, J.C., Pattnayak, K.C., 2018. Recent intensification of Amazon flooding extremes driven by strengthened Walker circulation. Sci. Adv. 4. https://doi.org/10.1126/sciadv.aat8785

Basso, L.S., Marani, L., Gatti, L. V., Miller, J.B., Gloor, M., Melack, J., Cassol, H.L.G., Tejada, G., Domingues, L.G., Arai, E., Sanchez, A.H., Corrêa, S.M., Anderson, L., Aragão, L.E.O.C., Correia, C.S.C., Crispim, S.P., Neves, R.A.L., 2021. Amazon methane budget derived from multi-year airborne observations highlights regional variations in emissions. Commun. Earth Environ. 2, 1–14. https://doi.org/10.1038/s43247-021-00314-4

Batalha, M.A., Cianciaruso, M. V., Silva, I.A., Delitti, W.B.C., 2005. Hyperseasonal cerrado, a new brazilian vegetation form. Brazilian J. Biol. 65, 735–738. https://doi.org/10.1590/S1519-69842005000400021

Bates, P.D., De Roo, A.P.J., 2000. A simple raster-based model for flood inundation simulation. J. Hydrol. https://doi.org/10.1016/S0022-1694(00)00278-X

Beck, H.E., Van Dijk, A.I.J.M., Levizzani, V., Schellekens, J., Miralles, D.G., Martens, B., De Roo, A., 2017. MSWEP: 3-hourly 0.25° global gridded precipitation (1979-2015) by merging gauge, satellite, and reanalysis data. Hydrol. Earth Syst. Sci. https://doi.org/10.5194/hess-21-589-2017

Beighley, R.E., Eggert, K.G., Dunne, T., He, Y., Gummadi, V., Verdin, K.L., 2009. Simulating hydrologic and hydraulic processes throughout the Amazon River Basin. Hydrol. Process. 23, 1221–1235. https://doi.org/10.1002/hyp.7252

Belger, L., Forsberg, B. R. Melack, J. M., 2011. Carbon dioxide and methane emissions from

interfluvial wetlands in the upper Negro River basin, Brazil. Biogeochemistry 105, 171–183. https://doi.org/10.1007/s10533-010-9536-0

Bernhofen, M. V, Whyman, C., Trigg, M.A., Sleigh, P.A., Smith, A.M., Sampson, C.C., Yamazaki, D., Ward, P.J., Rudari, R., Pappenberger, F., Dottori, F., Salamon, P., Winsemius, H.C., 2018. A first collective validation of global fluvial flood models for major floods in Nigeria and Mozambique. Environ. Res. Lett. 13, 104007. https://doi.org/10.1088/1748-9326/aae014

Biancamaria, S., Lettenmaier, D. P., Pavelsky, T. M, 2016. The SWOT Mission and Its Capabilities for Land Hydrology. Surv. Geophys. 37, 307–337. https://doi.org/10.1007/s10712-015-9346-y

Blatrix, R., Roux, B., Béarez, P., Prestes-Carneiro, G., Amaya, M., Aramayo, J.L., Rodrigues, L., Lombardo, U., Iriarte, J., De Souza, J.G., Robinson, M., Bernard, C., Pouilly, M., Durécu, M., Huchzermeyer, C.F., Kalebe, M., Ovando, A., McKey, D., 2018. The unique functioning of a pre-Columbian Amazonian floodplain fishery. Sci. Rep. 8. https://doi.org/10.1038/s41598-018-24454-4

Bodmer, R., Mayor, P., Antunez, M., Chota, K., Fang, T., Puertas, P., Pittet, M., Kirkland, M., Walkey, M., Rios, C., Perez-Peña, P., Henderson, P., Bodmer, W., Bicerra, A., Zegarra, J., Docherty, E., 2018. Major shifts in Amazon wildlife populations from recent intensification of floods and drought. Conserv. Biol. 32, 333–344. https://doi.org/10.1111/cobi.12993

Bonnet, M.P., Barroux, G., Martinez, J.M., Seyler, F., Moreira-Turcq, P., Cochonneau, G., Melack, J.M., Boaventura, G., Maurice-Bourgoin, L., León, J.G., Roux, E., Calmant, S.,

Kosuth, P., Guyot, J.L., Seyler, P., 2008. Floodplain hydrology in an Amazon floodplain lake (Lago Grande de Curuaí). J. Hydrol. 349, 18–30. https://doi.org/10.1016/j.jhydrol.2007.10.055

Bonnet, M.P., Pinel, S., Garnier, J., Bois, J., Resende Boaventura, G., Seyler, P., Motta Marques, D., 2017. Amazonian floodplain water balance based on modelling and analyses of hydrologic and electrical conductivity data. Hydrol. Process. 31, 1702–1718. https://doi.org/10.1002/hyp.11138

Bontemps, S., Defourny, P., Radoux, J., Van Bogaert, E. Lamarche, C., Achard, F., Mayaux, P., Boettcher, M., Brockmann, C., Kirches, G., 2013. Consistent global land cover maps for climate modelling communities: current achievements of the ESA's land cover CCI, in: Proceedings of the ESA Living Planet Symposium. Edinburgh.

Bourgoin, L.M., Bonnet, M.P., Martinez, J.M., Kosuth, P., Cochonneau, G., Moreira-Turcq, P., Guyot, J.L., Vauchel, P., Filizola, N., Seyler, P., 2007. Temporal dynamics of water and sediment exchanges between the Curuaí floodplain and the Amazon River, Brazil. J. Hydrol. 335, 140–156. https://doi.org/10.1016/j.jhydrol.2006.11.023

Canisius, F., Brisco, B., Murnaghan, K., Van Der Kooij, M., Keizer, E., 2019. SAR backscatter and InSAR coherence for monitoring wetland extent, flood pulse and vegetation: A study of the Amazon lowland. Remote Sens. 11, 1–18. https://doi.org/10.3390/RS11060720

Castello, L., 2008. Lateral migration of *Arapaima gigas* in floodplains of the Amazon. Ecol. Freshw. Fish 17, 38–46. https://doi.org/10.1111/j.1600-0633.2007.00255.x

Chapman, B., McDonald, K., Shimada, M., Rosenqvist, A., Schroeder, R., Hess, L., 2015.

Mapping Regional Inundation with Spaceborne L-Band SAR. Remote Sens. 7, 5440–5470. https://doi.org/10.3390/rs70505440

Coe, M.T., Costa, M.H., Howard, E.A., 2008. Simulating the surface waters of the Amazon River basin: impacts of new river geomorphic and flow parameterizations. Hydrol. Process. 22, 2542–2553. https://doi.org/10.1002/hyp.6850

Coomes, O.T., Lapointe, M., Templeton, M., List, G., 2016. Amazon river flow regime and flood recessional agriculture: Flood stage reversals and risk of annual crop loss. J. Hydrol. 539, 214–222. https://doi.org/10.1016/j.jhydrol.2016.05.027

Coomes, O.T., Takasaki, Y., Abizaid, C., Barham, B.L., 2010. Floodplain fisheries as natural insurance for the rural poor in tropical forest environments: Evidence from Amazonia. Fish. Manag. Ecol. 17, 513–521. https://doi.org/10.1111/j.1365-2400.2010.00750.x

Dalmagro, H.J., de A. Lobo, F., Vourlitis, G.L., Dalmolin, Â.C., Antunes, M.Z., Ortíz, C.E.R., de S. Nogueira, J., 2016. Photosynthetic response of a wetland- and an upland-adapted tree species to seasonal variations in hydrology in the Brazilian Cerrado and Pantanal. Acta Physiol. Plant. 38, 107. https://doi.org/10.1007/s11738-016-2125-7

de Almeida, G.A.M., Bates, P., Ozdemir, H., 2018. Modelling urban floods at submetre resolution: challenges or opportunities for flood risk management? J. Flood Risk Manag. 11, S855–S865. https://doi.org/10.1111/jfr3.12276

Denevan, W.M., 1996. A Bluff Model of Riverine Settlement in Prehistoric Amazonia. Ann. Assoc. Am. Geogr. 86, 654–681. https://doi.org/10.1111/j.1467-8306.1996.tb01771.x

Draper, F.C., Roucoux, K.H., Lawson, I.T., Mitchard, E.T.A., Honorio Coronado, E.N., Lähteenoja, O., Montenegro, L.T., Sandoval, E.V., Zaráte, R., Baker, T.R., 2014. The distribution and amount of carbon in the largest peatland complex in Amazonia. Environ. Res. Lett. 9. https://doi.org/10.1088/1748-9326/9/12/124017

Dunne, T., Mertes, L.A.K., Meade, R.H., Richey, J.E., Forsberg, B.R., 1998. Exchanges of sediment between the flood plain and channel of the Amazon River in Brazil. Bull. Geol. Soc. Am. 110, 450–467. https://doi.org/10.1130/0016-7606(1998)110<0450:EOSBTF>2.3.CO;2

Duponchelle, F., Isaac, V.J., Doria, C., Van Damme, P.A., Herrera-R, G.A., Anderson, E.P., Cruz, R.E.A., Hauser, M., Hermann, T.W., Agudelo, E., Bonilla-Castillo, C., Barthem, R., Freitas, C.E.C., García-Dávila, C., García-Vasquez, A., Renno, J., Castello, L., 2021. Conservation of migratory fishes in the Amazon basin. Aquat. Conserv. Mar. Freshw. Ecosyst. aqc.3550. https://doi.org/10.1002/aqc.3550

Espinoza Villar, J.C., Ronchail, J., Guyot, J.L., Cochonneau, G., Naziano, F., Lavado, W., De Oliveira, E., Pombosa, R., Vauchel, P., 2009. Spatio-temporal rainfall variability in the Amazon basin countries (Brazil, Peru, Bolivia, Colombia, and Ecuador). Int. J. Climatol. 29, 1574–1594. https://doi.org/10.1002/joc.1791

Espinoza Villar, J.C., Ronchail, J., Marengo, J.A., Segura, H., 2019. Contrasting North–South changes in Amazon wet-day and dry-day frequency and related atmospheric features (1981–2017). Clim. Dyn. 52, 5413–5430. https://doi.org/10.1007/s00382-018-4462-2

Farr, T.G., Rosen, P.A., Caro, E., Crippen, R., Duren, R., Hensley, S., Kobrick, M., Paller, M., Rodriguez, E., Roth, L., Seal, D., Shaffer, S., Shimada, J., Umland, J., Werner, M., Oskin, M., Burbank, D., Alsdorf, D.E., 2007. The shuttle radar topography mission. Rev. Geophys. 45, 1–25. https://doi.org/10.1029/2005RG000183

Fassoni-Andrade, 2020. PhD thesis. Mapeamento e caracterização do sistema rio-planície da Amazônia central via sensoriamento remoto e modelagem hidráulica. Federal University of Rio Grande do Sul. Available at <https://lume.ufrgs.br/handle/10183/211269>.

Fassoni-Andrade, A.C., Fleischmann, A.S., Papa, F., Paiva, R.C.D. de, Wongchuig, S., Melack, J.M., Moreira, A.A., Paris, A., Ruhoff, A., Barbosa, C., Maciel, D.A., Novo, E., Durand, F., Frappart, F., Aires, F., Abrahão, G.M., Ferreira-Ferreira, J., Espinoza, J.C., Laipelt, L., Costa, M.H., Espinoza-Villar, R., Calmant, S., Pellet, V., 2021. Amazon Hydrology From Space: Scientific Advances and Future Challenges. Rev. Geophys. 59, 1–97. https://doi.org/10.1029/2020RG000728

Fassoni-Andrade, A.C., Paiva, R.C.D. de, 2019. Mapping spatial-temporal sediment dynamics of river-floodplains in the Amazon. Remote Sens. Environ. https://doi.org/10.1016/j.rse.2018.10.038

Fassoni-Andrade, A.C., Paiva, R.C.D. de, Rudorff, C. de M., Barbosa, C.C.F., Novo, E.M.L. de M., 2020. High-resolution mapping of floodplain topography from space: A case study in the Amazon. Remote Sens. Environ. 251, 112065. https://doi.org/10.1016/j.rse.2020.112065

Feng, D., Raoufi, R., Beighley, E., Melack, J.M., Goulding, M., Barthem, R.B., Venticinque, E., Cañas, C., Forsberg, B., Sorribas, M.V., 2020. Future climate impacts on the hydrology of

headwater streams in the Amazon River Basin: Implications for migratory goliath catfishes. Hydrol. Process. hyp.13952. https://doi.org/10.1002/hyp.13952

Ferreira-Ferreira, J., Silva, T.S.F., Streher, A.S., Affonso, A.G., de Almeida Furtado, L.F., Forsberg, B.R., Valsecchi, J., Queiroz, H.L., de Moraes Novo, E.M.L., 2015. Combining ALOS/PALSAR derived vegetation structure and inundation patterns to characterize major vegetation types in the Mamirauá Sustainable Development Reserve, Central Amazon floodplain, Brazil. Wetl. Ecol. Manag. 23, 41–59. https://doi.org/10.1007/s11273-014-9359-1

Fleischmann, A.S., Fialho Brêda, J.P., Rudorff, C., Dias de Paiva, R.C., Collischonn, W., Papa, F., Ravanello, M.M., 2021. River Flood Modeling and Remote Sensing Across Scales: Lessons from Brazil, in: Schumann, G.J.P. (Ed.), Earth Observation for Flood Applications. Elsevier, pp. 61–103. https://doi.org/10.1016/B978-0-12-819412-6.00004-3

Fleischmann, A.S., Paiva, R.C.D., Collischonn, W., Siqueira, V.A., Paris, A., Moreira, D.M., Papa, F., Bitar, A.A., Parrens, M., Aires, F., Garambois, P.A., 2020. Trade-Offs Between 1-D and 2-D Regional River Hydrodynamic Models. Water Resour. Res. 56. https://doi.org/10.1029/2019WR026812

Flores, B.M., Holmgren, M., 2021. White-Sand Savannas Expand at the Core of the Amazon After Forest Wildfires. Ecosystems 24, 1624–1637. https://doi.org/10.1007/s10021-021-00607-x

Fluet-Chouinard, E., Lehner, B., Rebelo, L.M., Papa, F., Hamilton, S.K., 2015. Development of a global inundation map at high spatial resolution from topographic downscaling of coarse-

scale remote sensing data. Remote Sens. Environ. 158, 348–361. https://doi.org/10.1016/j.rse.2014.10.015

Frappart, F., Seyler, F., Martinez, J., León, J.G., Cazenave, A., 2005. Floodplain water storage in the Negro River basin estimated from microwave remote sensing of inundation area and water levels. Remote Sens. Environ. 99, 387–399. https://doi.org/10.1016/j.rse.2005.08.016

Fu, R., Yin, L., Li, W., Arias, P.A., Dickinson, R.E., Huang, L., Chakraborty, S., Fernandes, K., Liebmann, B., Fisher, R., Myneni, R.B., 2013. Increased dry-season length over southern Amazonia in recent decades and its implication for future climate projection. Proc. Natl. Acad. Sci. U. S. A. 110, 18110–18115. https://doi.org/10.1073/pnas.1302584110

Getirana, A., Boone, A., Yamazaki, D., Decharme, B., Papa, F., Mognard, N., 2012. The Hydrological Modeling and Analysis Platform (HyMAP): Evaluation in the Amazon Basin. J. Hydrometeorol. 13, 1641–1665. https://doi.org/10.1175/JHM-D-12-021.1

Getirana, A., Peters-Lidard, C., Rodell, M., Bates, P.D., 2017. Trade-off between cost and accuracy in large-scale surface water dynamic modeling. Water Resour. Res. 53, 4942–4955. https://doi.org/10.1002/2017WR020519

Gloor, M., Brienen, R.J.W., Galbraith, D., Feldpausch, T.R., Schöngart, J., Guyot, J.L., Espinoza, J.C., Lloyd, J., Phillips, O.L., 2013. Intensification of the Amazon hydrological cycle over the last two decades. Geophys. Res. Lett. 40, 1729–1733. https://doi.org/10.1002/grl.50377

Guilhen, J., Al Bitar, A., Sauvage, S., Parrens, M., Martinez, J., Abril, G., Moreira-Turcq, P., Sánchez-Pérez, J.-M., 2020. Denitrification and associated nitrous oxide and carbon dioxide

emissions from the Amazonian wetlands. Biogeosciences 17, 4297–4311. https://doi.org/10.5194/bg-17-4297-2020

Guimberteau, M., Drapeau, G., Ronchail, J., Sultan, B., Polcher, J., Martinez, J.-M., Prigent, C., Guyot, J.-L., Cochonneau, G., Espinoza, J.C., Filizola, N., Fraizy, P., Lavado, W., De Oliveira, E., Pombosa, R., Noriega, L., Vauchel, P., 2012. Discharge simulation in the sub-basins of the Amazon using ORCHIDEE forced by new datasets. Hydrol. Earth Syst. Sci. 16, 911–935. https://doi.org/10.5194/hess-16-911-2012

Gumbricht, T., Roman-Cuesta, R.M., Verchot, L., Herold, M., Wittmann, F., Householder, E., Herold, N., Murdiyarso, D., 2017. An expert system model for mapping tropical wetlands and peatlands reveals South America as the largest contributor. Glob. Chang. Biol. 23, 3581–3599. https://doi.org/10.1111/gcb.13689

Hamilton, S.K., Kellndorfer, J., Lehner, B., Tobler, M., 2007. Remote sensing of floodplain geomorphology as a surrogate for biodiversity in a tropical river system (Madre de Dios, Peru). Geomorphology 89, 23–38. https://doi.org/10.1016/j.geomorph.2006.07.024

Hamilton, S.K., Sippel, S.J., Melack, J.M., 2002. Comparison of inundation patterns among major South American floodplains. Journal of Geophysical Research 107 (D20): Art. No. 8038, 1–14. https://doi.org/. doi 10.1029/2000JD000306107

Hamilton, S.K., Sippel, S.J., Melack, J.M., 2004. Seasonal inundation patterns in two large savanna floodplains of South America: the Llanos de Moxos(Bolivia) and the Llanos del Orinoco(Venezuela and Colombia). Hydrol. Process. 18, 2103–2116. https://doi.org/10.1002/hyp.5559

1342 Hansen, M.C., Potapov, P. V., Moore, R., Hancher, M., Turubanova, S.A., Tyukavina, A., Thau,
1343 D., Stehman, S. V., Goetz, S.J., Loveland, T.R., Kommareddy, A., Egorov, A., Chini, L.,
1344 Justice, C.O., Townshend, J.R.G., 2013. High-Resolution Global Maps of 21st-Century
1345 Forest Cover Change. Science (80-.). 342, 850–853.
1346 https://doi.org/10.1126/science.1244693

1347 Harris, I., Jones, P.D., Osborn, T.J., Lister, D.H., 2014. Updated high-resolution grids of monthly
1348 climatic observations - the CRU TS3.10 Dataset. Int. J. Climatol. 34, 623–642.
1349 https://doi.org/10.1002/joc.3711

1350 Hawes, J.E., Peres, C.A., Riley, L.B., Hess, L.L., 2012. Landscape-scale variation in structure
1351 and biomass of Amazonian seasonally flooded and unflooded forests. For. Ecol. Manage.
1352 281, 163–176. https://doi.org/10.1016/j.foreco.2012.06.023

1353 Hess, L.L., Melack, J.M., Affonso, A.G., Barbosa, C., Gastil-Buhl, M., Novo, E.M.L.M., 2015.
1354 Wetlands of the Lowland Amazon Basin: Extent, Vegetative Cover, and Dual-season
1355 Inundated Area as Mapped with JERS-1 Synthetic Aperture Radar. Wetlands 35, 745–756.
1356 https://doi.org/10.1007/s13157-015-0666-y

1357 Hess, L.L., Melack, J.M., Novo, E.M.L.M., Barbosa, C.C.F., Gastil, M., 2003. Dual-season
1358 mapping of wetland inundation and vegetation for the central Amazon basin. Remote Sens.
1359 Environ. 87, 404–428. https://doi.org/10.1016/j.rse.2003.04.001

1360 Hoch, J.M., Haag, A. V., Van Dam, A., Winsemius, H.C., Van Beek, L.P.H., Bierkens, M.F.P.,
1361 2017. Assessing the impact of hydrodynamics on large-scale flood wave propagation: A
1362 case study for the Amazon Basin. Hydrol. Earth Syst. Sci. 21, 117–132.

https://doi.org/10.5194/hess-21-117-2017

Hu, S., Niu, Z., Chen, Y., 2017. Global Wetland Datasets: a Review. Wetlands 37, 807–817. https://doi.org/10.1007/s13157-017-0927-z

Jardim, C.M., Nardoto, G.B., de Lima, A.C.B., de Jesus Silva, R., Schor, T., de Oliveira, J.A., Martinelli, L.A., 2020. The influence of seasonal river flooding in food consumption of riverine dwellers in the central Amazon region: an isotopic approach. Archaeol. Anthropol. Sci. 12. https://doi.org/10.1007/s12520-020-01172-5

Jensen, K., Mcdonald, K., 2019. Surface Water Microwave Product Series Version 3: A Near-Real Time and 25-Year Historical Global Inundated Area Fraction Time Series From Active and Passive Microwave Remote Sensing. IEEE Geosci. Remote Sens. Lett. 16, 1402–1406. https://doi.org/10.1109/lgrs.2019.2898779

Jensen, K., McDonald, K., Podest, E., Rodriguez-Alvarez, N., Horna, V., Steiner, N., 2018. Assessing L-Band GNSS-Reflectometry and Imaging Radar for Detecting Sub-Canopy Inundation Dynamics in a Tropical Wetlands Complex. Remote Sens. 10, 1431. https://doi.org/10.3390/rs10091431

Ji, X., Lesack, L.F.W., Melack, J.M., Wang, S., Riley, W.J., Shen, C., 2019. Seasonal and Interannual Patterns and Controls of Hydrological Fluxes in an Amazon Floodplain Lake With a Surface-Subsurface Process Model. Water Resour. Res. 55, 3056–3075. https://doi.org/10.1029/2018WR023897

Junk, W.J., Bayley, P.B., Sparks, R.E, 1989. The flood pulse concept in river-floodplain systems. Canadian special publication of fisheries and aquatic sciences, 106.1, 110-127.

1384 Junk, W.J., Furch, K., Limnologie, M., Tropenokologie, A., Plon, W.-, 1993. A general review
1385 of tropical South American floodplains. Wetl. Ecol. Manag. 2, 231–238.

1386 Junk, W.J., Piedade, M.T.F., Schöngart, J., Cohn-Haft, M., Adeney, J.M., Wittmann, F., 2011. A
1387 classification of major naturally-occurring amazonian lowland wetlands. Wetlands 31, 623–
1388 640. https://doi.org/10.1007/s13157-011-0190-7

1389 Lähteenoja, O., Reátegui, Y.R., Räsänen, M., Torres, D.D.C., Oinonen, M., Page, S., 2012. The
1390 large Amazonian peatland carbon sink in the subsiding Pastaza-Marañón foreland basin,
1391 Peru. Glob. Chang. Biol. 18, 164–178. https://doi.org/10.1111/j.1365-2486.2011.02504.x

1392 Langerwisch, F., Rost, S., Gerten, D., Poulter, B., Rammig, A., Cramer, W., 2013. Potential
1393 effects of climate change on inundation patterns in the Amazon Basin. Hydrol. Earth Syst.
1394 Sci. 17, 2247–2262. https://doi.org/10.5194/hess-17-2247-2013

1395 Langill, J.C., Abizaid, C., 2020. What is a bad flood? Local perspectives of extreme floods in the
1396 Peruvian Amazon. Ambio 49, 1423–1436. https://doi.org/10.1007/s13280-019-01278-8

1397 Latrubesse, E.M., 2012. Amazon lakes, in: Encyclopedia of Earth Sciences Series.
1398 https://doi.org/10.1007/978-1-4020-4410-6_36

1399 Lauerwald, R., Regnier, P., Camino-Serrano, M., Guenet, B., Guimberteau, M., Ducharne, A.,
1400 Polcher, J., Ciais, P., 2017. ORCHILEAK (revision 3875): a new model branch to simulate
1401 carbon transfers along the terrestrial–aquatic continuum of the Amazon basin. Geosci.
1402 Model Dev. 10, 3821–3859. https://doi.org/10.5194/gmd-10-3821-2017

1403 Lehner, B., Döll, P., 2004. Development and validation of a global database of lakes, reservoirs

and wetlands. J. Hydrol. 296, 1–22. https://doi.org/10.1016/j.jhydrol.2004.03.028

Lehner, B., Grill, G., 2013. Global river hydrography and network routing: Baseline data and new approaches to study the world's large river systems. Hydrol. Process. https://doi.org/10.1002/hyp.9740

Lesack, L.F.W., Melack, J.M., 1995. Flooding Hydrology and Mixture Dynamics of Lake Water Derived from Multiple Sources in an Amazon Floodplain Lake. Water Resour. Res. 31, 329–345. https://doi.org/10.1029/94WR02271

Li, D., Lu, D., Moran, E., da Silva, R.F.B., 2020. Examining water area changes accompanying dam construction in the Madeira River in the Brazilian Amazon. Water (Switzerland) 12. https://doi.org/10.3390/w12071921

Lobón-Cerviá, J., Hess, L.L., Melack, J.M., Araujo-Lima, C.A.R.M., 2015. The importance of forest cover for fish richness and abundance on the Amazon floodplain. Hydrobiologia 750, 245–255. https://doi.org/10.1007/s10750-014-2040-0

Luize, B.G., Silva, T.S.F., Wittmann, F., Assis, R.L., Venticinque, E.M., 2015. Effects of the Flooding Gradient on Tree Community Diversity in Várzea Forests of the Purus River, Central Amazon, Brazil. Biotropica 47, 137–142. https://doi.org/10.1111/btp.12203

Luo, X., Li, H.-Y., Leung, L.R., Tesfa, T.K., Getirana, A., Papa, F., Hess, L.L., 2017. Modeling surface water dynamics in the Amazon Basin using MOSART-Inundation v1.0: impacts of geomorphological parameters and river flow representation. Geosci. Model Dev. 10, 1233–1259. https://doi.org/10.5194/gmd-10-1233-2017

1424 Mansur, A. V., Brondízio, E.S., Roy, S., Hetrick, S., Vogt, N.D., Newton, A., 2016. An
1425 assessment of urban vulnerability in the Amazon Delta and Estuary: a multi-criterion index
1426 of flood exposure, socio-economic conditions and infrastructure. Sustain. Sci. 11, 625–643.
1427 https://doi.org/10.1007/s11625-016-0355-7

1428 Martinez, J.M., Le Toan, T., 2007. Mapping of flood dynamics and spatial distribution of
1429 vegetation in the Amazon floodplain using multitemporal SAR data. Remote Sens. Environ.
1430 108, 209–223. https://doi.org/10.1016/j.rse.2006.11.012

1431 Martínez-Espinosa, C., Sauvage, S., Al Bitar, A., Green, P. A., Vörösmarty, C. J., Sánchez-
1432 Pérez, J. M. (2020). Denitrification in wetlands: A review towards a quantification at global
1433 scale. Science of the total environment 754, 142398.
1434 https://doi.org/10.1016/j.scitotenv.2020.142398

1435 Matthews, E., Fung, I., 1987. Methane emission from natural wetlands: Global distribution, area,
1436 and environmental characteristics of sources. Global Biogeochem. Cycles 1, 61–86.
1437 https://doi.org/10.1029/GB001i001p00061

1438 Melack, J.M., 2016. Aquatic Ecosystems, in: Ecological Studies. pp. 119–148.
1439 https://doi.org/10.1007/978-3-662-49902-3_7

1440 Melack, J.M., Coe, M.T., 2021. Amazon floodplain hydrology and implications for aquatic
1441 conservation. Aquat. Conserv. Mar. Freshw. Ecosyst. 1029–1040.
1442 https://doi.org/10.1002/aqc.3558

1443 Melack, J.M., Forsberg, B.R., 2001. Biogeochemistry of Amazon Floodplain, in: McClain, M.E.,
1444 Victoria, R., Richey, J.E. (Eds.), The Biogeochemistry of the Amazon Basin. Oxford

University Press, New York, USA.

Melack, J.M., Hess, L.L., 2010. Remote Sensing of the Distribution and Extent of Wetlands in the Amazon Basin, in: Amazonian Floodplain Forests. pp. 43–59. https://doi.org/10.1007/978-90-481-8725-6_3

Melack, J.M., Hess, L.L., Gastil, M., Forsberg, B.R., Hamilton, S.K., Lima, I.B.T., Novo, E.M.L.M., 2004. Regionalization of methane emissions in the Amazon Basin with microwave remote sensing. Glob. Chang. Biol. 10, 530–544. https://doi.org/10.1111/j.1365-2486.2004.00763.x

Meyer Oliveira, A., Fleischmann, A., Paiva, R., 2020. On the contribution of remote sensing-based calibration to model multiple hydrological variables. J. Hydrol. https://doi.org/10.1016/j.jhydrol.2021.126184

Miguez-Macho, G., Fan, Y., 2012. The role of groundwater in the Amazon water cycle: 1. Influence on seasonal streamflow, flooding and wetlands. J. Geophys. Res. Atmos. 117, 1–30. https://doi.org/10.1029/2012JD017539

Nardi, F., Annis, A., Di Baldassarre, G., Vivoni, E.R., Grimaldi, S., 2019. GFPLAIN250m, a global high-resolution dataset of Earth's floodplains. Sci. Data 6, 180309. https://doi.org/10.1038/sdata.2018.309

O'Loughlin, F.E., Paiva, R.C.D., Durand, M., Alsdorf, D.E., Bates, P.D., 2016. A multi-sensor approach towards a global vegetation corrected SRTM DEM product. Remote Sens. Environ. 182, 49–59. https://doi.org/10.1016/j.rse.2016.04.018

Ovando, A., Martinez, J.M., Tomasella, J., Rodriguez, D.A., von Randow, C., 2018. Multi-temporal flood mapping and satellite altimetry used to evaluate the flood dynamics of the Bolivian Amazon wetlands. Int. J. Appl. Earth Obs. Geoinf. 69, 27–40. https://doi.org/10.1016/j.jag.2018.02.013

Ovando, A., Tomasella, J., Rodriguez, D.A., Martinez, J.M., Siqueira-Junior, J.L., Pinto, G.L.N., Passy, P., Vauchel, P., Noriega, L., von Randow, C., 2016. Extreme flood events in the Bolivian Amazon wetlands. J. Hydrol. Reg. Stud. 5, 293–308. https://doi.org/10.1016/j.ejrh.2015.11.004

Paca, V.H. da M., Espinoza-Dávalos, G.E., Hessels, T.M., Moreira, D.M., Comair, G.F., Bastiaanssen, W.G.M., 2019. The spatial variability of actual evapotranspiration across the Amazon River Basin based on remote sensing products validated with flux towers. Ecol. Process. 8, 6. https://doi.org/10.1186/s13717-019-0158-8

Paiva, R., Buarque, D.C., Collischonn, W., Bonnet, M.P., Frappart, F., Calmant, S., Bulhões Mendes, C.A., 2013. Large-scale hydrologic and hydrodynamic modeling of the Amazon River basin. Water Resour. Res. 49, 1226–1243. https://doi.org/10.1002/wrcr.20067

Pangala, S.R., Enrich-Prast, A., Basso, L.S., Peixoto, R.B., Bastviken, D., Hornibrook, E.R.C., Gatti, L. V., Marotta, H., Calazans, L.S.B., Sakuragui, C.M., Bastos, W.R., Malm, O., Gloor, E., Miller, J.B., Gauci, V., 2017. Large emissions from floodplain trees close the Amazon methane budget. Nature 552, 230–234. https://doi.org/10.1038/nature24639

Papa, F., J.-F. Crétaux, M. Grippa, E. Robert, M. Trigg, R. Tshimanga, B. Kitambo, A. Paris, A. Carr, A.S. Fleischmann, M. de Fleury, P.G. Gbetkom, B. Calmettes, Calmant, S., 2022.

Water Resources in Africa under Global Change: Monitoring Surface Waters from Space. Surveys in Geophysics. https://doi.org/10.1007/s10712-022-09700-9

Papa, F., and F. Frappart (2021), Surface Water Storage in Rivers and Wetlands Derived from Satellite Observations: A Review of Current Advances and Future Opportunities for Hydrological Sciences, Remote Sensing, 13(20), 4162, doi:10.3390/rs13204162

Papa, F., Güntner, A., Frappart, F., Prigent, C., Rossow, W.B., 2008. Variations of surface water extent and water storage in large river basins: A comparison of different global data sources. Geophys. Res. Lett. 35, L11401. https://doi.org/10.1029/2008GL033857

Papa, F., Prigent, C., Aires, F., Jimenez, C., Rossow, W.B., Matthews, E., 2010. Interannual variability of surface water extent at the global scale, 1993–2004. J. Geophys. Res. 115, D12111. https://doi.org/10.1029/2009JD012674

Park, E., Latrubesse, E.M., 2017. The hydro-geomorphologic complexity of the lower Amazon River floodplain and hydrological connectivity assessed by remote sensing and field control. Remote Sens. Environ. 198, 321–332. https://doi.org/10.1016/j.rse.2017.06.021

Park, E., Latrubesse, E.M., 2019. A geomorphological assessment of wash-load sediment fluxes and floodplain sediment sinks along the lower Amazon River. Geology 47, 403–406. https://doi.org/10.1130/G45769.1

Parrens, M., Al Bitar, A., Frappart, F., Papa, F., Calmant, S., Crétaux, J.-F., Wigneron, J.-P., Kerr, Y., 2017. Mapping Dynamic Water Fraction under the Tropical Rain Forests of the Amazonian Basin from SMOS Brightness Temperatures. Water 9, 350. https://doi.org/10.3390/w9050350

Parrens, M., Bitar, A. Al, Frappart, F., Paiva, R., Wongchuig, S., Papa, F., Yamasaki, D., Kerr, Y., 2019. High resolution mapping of inundation area in the Amazon basin from a combination of L-band passive microwave, optical and radar datasets. Int. J. Appl. Earth Obs. Geoinf. 81, 58–71. https://doi.org/10.1016/j.jag.2019.04.011

Pekel, J., Cottam, A., Gorelick, N., Belward, A.S., 2016. High-resolution mapping of global surface water and its long-term changes. Nature 540, 418–422. https://doi.org/10.1038/nature20584

Pellet, V., Aires, F., Yamazaki, D., Papa, F., 2021. Coherent Satellite Monitoring of the Water Cycle Over the Amazon. Part 1: Methodology and Initial Evaluation. Water Resour. Res. 57, 1–21. https://doi.org/10.1029/2020wr028647

Pham-Duc, B., Prigent, C., Aires, F., Papa, F., 2017. Comparisons of global terrestrial surface water datasets over 15 years. J. Hydrometeorol. 18, 993–1007. https://doi.org/10.1175/JHM-D-16-0206.1

Pickens, A.H., Hansen, M.C., Hancher, M., Stehman, S. V., Tyukavina, A., Potapov, P., Marroquin, B., Sherani, Z., 2020. Mapping and sampling to characterize global inland water dynamics from 1999 to 2018 with full Landsat time-series. Remote Sens. Environ. 243, 111792. https://doi.org/10.1016/j.rse.2020.111792

Pinel, S., Bonnet, M., S. Da Silva, J., Sampaio, T.C., Garnier, J., Catry, T., Calmant, S., Fragoso, C.R., Moreira, D., Motta Marques, D., Seyler, F., 2019. Flooding dynamics within an Amazonian floodplain: water circulation patterns and inundation duration. Water Resour. Res. 2019WR026081. https://doi.org/10.1029/2019WR026081

1528 Prigent, C., Jimenez, C., Bousquet, P., 2020. Satellite-Derived Global Surface Water Extent and
1529 Dynamics Over the Last 25 Years (GIEMS-2). J. Geophys. Res. Atmos. 125, 1–18.
1530 https://doi.org/10.1029/2019JD030711

1531 Prigent, C., Matthews, E., Aires, F., Rossow, W.B., 2001. Remote sensing of global wetland
1532 dynamics with multiple satellite data sets. Geophys. Res. Lett. 28, 4631–4634.
1533 https://doi.org/10.1029/2001GL013263

1534 Prigent, C., Papa, F., Aires, F., Rossow, W.B., Matthews, E., 2007. Global inundation dynamics
1535 inferred from multiple satellite observations, 1993-2000. J. Geophys. Res. Atmos. 112,
1536 1993–2000. https://doi.org/10.1029/2006JD007847

1537 Prigent, C., Rochetin, N., Aires, F., Defer, E., Grandpeix, J.-Y., Jimenez, C., Papa, F., 2011.
1538 Impact of the inundation occurrence on the deep convection at continental scale from
1539 satellite observations and modeling experiments. J. Geophys. Res. Atmos. 116, n/a-n/a.
1540 https://doi.org/10.1029/2011JD016311

1541 Reis, V., Hermoso, V., Hamilton, S.K., Bunn, S.E., Fluet-Chouinard, E., Venables, B., Linke, S.,
1542 2019. Characterizing seasonal dynamics of Amazonian wetlands for conservation and
1543 decision making. Aquat. Conserv. Mar. Freshw. Ecosyst. 29, 1073–1082.
1544 https://doi.org/10.1002/aqc.3051

1545 Reis, V., Hermoso, V., Hamilton, S.K., Bunn, S.E., Linke, S., 2019b. Conservation planning for
1546 river-wetland mosaics: A flexible spatial approach to integrate floodplain and upstream
1547 catchment connectivity. Biol. Conserv. 236, 356–365.
1548 https://doi.org/10.1016/j.biocon.2019.05.042

Rennó, C.D., Nobre, A.D., Cuartas, L.A., Soares, J.V., Hodnett, M.G., Tomasella, J., Waterloo, M.J., 2008. HAND, a new terrain descriptor using SRTM-DEM: Mapping terra-firme rainforest environments in Amazonia. Remote Sens. Environ. 112, 3469–3481. https://doi.org/10.1016/j.rse.2008.03.018

Renó, V.F., Novo, E.M.L.M., Suemitsu, C., Rennó, C.D., Silva, T.S.F., 2011. Assessment of deforestation in the Lower Amazon floodplain using historical Landsat MSS/TM imagery. Remote Sens. Environ. 115, 3446–3456. https://doi.org/10.1016/j.rse.2011.08.008

Resende, A.F. de, Schöngart, J., Streher, A.S., Ferreira-Ferreira, J., Piedade, M.T.F., Silva, T.S.F., 2019. Massive tree mortality from flood pulse disturbances in Amazonian floodplain forests: The collateral effects of hydropower production. Sci. Total Environ. 659, 587–598. https://doi.org/10.1016/j.scitotenv.2018.12.208

Restrepo A, J.D., Kettner, A.J., Robert Brakenridge, G., 2020. Monitoring water discharge and floodplain connectivity for the northern Andes utilizing satellite data: A tool for river planning and science-based decision-making. J. Hydrol. 586, 124887. https://doi.org/10.1016/j.jhydrol.2020.124887

Richey, J.E., Hedges, J.I., Devol, A.H., Quay, P.D., Victoria, R., Martinelli, L., Forsberg, B.R., 1990. Biogeochemistry of carbon in the Amazon River. Limnol. Oceanogr. 35, 352–371. https://doi.org/10.4319/lo.1990.35.2.0352

Richey, J.E., Melack, J.M., Aufdenkampe, A.K., Ballester, V.M., Hess, L.L., 2002. Outgassing from Amazonian rivers and wetlands as a large tropical source of atmospheric CO2. Nature 416, 617–620. https://doi.org/10.1038/416617a

Ringeval, B., Decharme, B., Piao, S.L., Ciais, P., Papa, F., de Noblet-Ducoudré, N., Prigent, C., Friedlingstein, P., Gouttevin, I., Koven, C., Ducharne, A., 2012. Modelling sub-grid wetland in the ORCHIDEE global land surface model: evaluation against river discharges and remotely sensed data. Geosci. Model Dev. 5, 941–962. https://doi.org/10.5194/gmd-5-941-2012

Ringeval, B., Houweling, S., van Bodegom, P.M., Spahni, R., van Beek, R., Joos, F., Röckmann, T., 2014. Methane emissions from floodplains in the Amazon Basin: challenges in developing a process-based model for global applications. Biogeosciences 11, 1519–1558. https://doi.org/10.5194/bg-11-1519-2014

Rodriguez-Alvarez, N., Podest, E., Jensen, K., McDonald, K.C., 2019. Classifying Inundation in a Tropical Wetlands Complex with GNSS-R. Remote Sens. 11, 1053. https://doi.org/10.3390/rs11091053

Rosenqvist, A., Forsberg, B.R., Pimentel, T., Rauste, Y.A., Richey, J.E., 2002. The use of spaceborne radar data to model inundation patterns and trace gas emissions in the central Amazon floodplain. Int. J. Remote Sens. 23, 1303–1328. https://doi.org/10.1080/01431160110092911

Rosenqvist, J., Rosenqvist, A., Jensen, K., McDonald, K., 2020. Mapping of Maximum and Minimum Inundation Extents in the Amazon Basin 2014–2017 with ALOS-2 PALSAR-2 ScanSAR Time-Series Data. Remote Sens. 12, 1326. https://doi.org/10.3390/rs12081326

Rosinger, A.Y., 2018. Household water insecurity after a historic flood: Diarrhea and dehydration in the Bolivian Amazon. Soc. Sci. Med. 197, 192–202.

https://doi.org/10.1016/j.socscimed.2017.12.016

Rossetti, D.F., Gribel, R., Rennó, C.D., Cohen, M.C.L., Moulatlet, G.M., Cordeiro, C.L. de O., Rodrigues, E. do S.F., 2017a. Late Holocene tectonic influence on hydrology and vegetation patterns in a northern Amazonian megafan. Catena 158, 121–130. https://doi.org/10.1016/j.catena.2017.06.022

Rossetti, D.F., Valeriano, M.M., Gribel, R., Cohen, M.C.L., Tatumi, S.H., Yee, M., 2017b. The imprint of Late Holocene tectonic reactivation on a megafan landscape in the northern Amazonian wetlands. Geomorphology 295, 406–418. https://doi.org/10.1016/j.geomorph.2017.07.026

Rudorff, C.M., Melack, J.M., Bates, P.D., 2014. Flooding dynamics on the lower Amazon floodplain: 1. Hydraulic controls on water elevation, inundation extent, and river-floodplain discharge. Water Resour. Res. 50, 619–634. https://doi.org/10.1002/2013WR014091

Ruf, C.S., Chew, C., Lang, T. et al. A New Paradigm in Earth Environmental Monitoring with the CYGNSS Small Satellite Constellation. Sci Rep 8, 8782 (2018). https://doi.org/10.1038/s41598-018-27127-4

Ruiz Agudelo, C.A., Mazzeo, N., Díaz, I., Barral, M.P., Piñeiro, G., Gadino, I., Roche, I., Acuña-Posada, R.J., 2020. Land use planning in the amazon basin: Challenges from resilience thinking. Ecol. Soc. 25. https://doi.org/10.5751/ES-11352-250108

Santos, J.O.S., Nelson, B.W., Giovannini, C.A., 1993. Corpos de areia sob leitos abandonados de grandes rios. Ciência Hoje 16, 22–25.

Santos, L.B.L., Carvalho, T., Anderson, L.O., Rudorff, C.M., Marchezini, V., Londe, L.R., Saito, S.M., 2017. An RS-GIS-Based ComprehensiveImpact Assessment of Floods—A Case Study in Madeira River, Western Brazilian Amazon. IEEE Geosci. Remote Sens. Lett. 14, 1614–1617. https://doi.org/10.1109/LGRS.2017.2726524

Santos, M.J., Medvigy, D., Silva Dias, M.A.F., Freitas, E.D., Kim, H., 2019. Seasonal Flooding Causes Intensification of the River Breeze in the Central Amazon. J. Geophys. Res. Atmos. 124, 5178–5197. https://doi.org/10.1029/2018JD029439

Saunois, M., Stavert, A.R., Poulter, B., Bousquet, P., Canadell, J.G., Jackson, R.B., Raymond, P.A., Dlugokencky, E.J., Houweling, S., Patra, P.K., Ciais, P., Arora, V.K., Bastviken, D., Bergamaschi, P., Blake, D.R., Brailsford, G., Bruhwiler, L., Carlson, K.M., Carrol, M., Castaldi, S., Chandra, N., Crevoisier, C., Crill, P.M., Covey, K., Curry, C.L., Etiope, G., Frankenberg, C., Gedney, N., Hegglin, M.I., Höglund-Isaksson, L., Hugelius, G., Ishizawa, M., Ito, A., Janssens-Maenhout, G., Jensen, K.M., Joos, F., Kleinen, T., Krummel, P.B., Langenfelds, R.L., Laruelle, G.G., Liu, L., Machida, T., Maksyutov, S., McDonald, K.C., McNorton, J., Miller, P.A., Melton, J.R., Morino, I., Müller, J., Murguia-Flores, F., Naik, V., Niwa, Y., Noce, S., O'Doherty, S., Parker, R.J., Peng, C., Peng, S., Peters, G.P., Prigent, C., Prinn, R., Ramonet, M., Regnier, P., Riley, W.J., Rosentreter, J.A., Segers, A., Simpson, I.J., Shi, H., Smith, S.J., Steele, L.P., Thornton, B.F., Tian, H., Tohjima, Y., Tubiello, F.N., Tsuruta, A., Viovy, N., Voulgarakis, A., Weber, T.S., van Weele, M., van der Werf, G.R., Weiss, R.F., Worthy, D., Wunch, D., Yin, Y., Yoshida, Y., Zhang, W., Zhang, Z., Zhao, Y., Zheng, B., Zhu, Qing, Zhu, Qiuan, Zhuang, Q., 2020. The Global Methane Budget 2000–2017. Earth Syst. Sci. Data 12, 1561–1623. https://doi.org/10.5194/essd-12-1561-2020

Schöngart, J., Wittmann, F., Faria de Resende, A., Assahira, C., Sousa Lobo, G., Rocha Duarte Neves, J., Rocha, M., Biem Mori, G., Costa Quaresma, A., Oreste Demarchi, L., Weiss Albuquerque, B., Oliveira Feitosa, Y., Silva Costa, G., Vieira Feitoza, G., Machado Durgante, F., Lopes, A., Trumbore, S.E., Sanna Freire Silva, T., Steege, H., Val, A.L., Junk, W.J., Piedade, M.T.F., 2021. The shadow of the Balbina dam: A synthesis of over 35 years of downstream impacts on floodplain forests in Central Amazonia. Aquat. Conserv. Mar. Freshw. Ecosyst. 31, 1117–1135. https://doi.org/10.1002/aqc.3526

Schroeder, R., McDonald, K., Chapman, B., Jensen, K., Podest, E., Tessler, Z., Bohn, T., Zimmermann, R., 2015. Development and Evaluation of a Multi-Year Fractional Surface Water Data Set Derived from Active/Passive Microwave Remote Sensing Data. Remote Sens. 7, 16688–16732. https://doi.org/10.3390/rs71215843

Schumann, G.J.P., Stampoulis, D., Smith, A.M., Sampson, C.C., Andreadis, K.M., Neal, J.C., Bates, P.D., 2016. Rethinking flood hazard at the global scale. Geophys. Res. Lett. 43, 10,249-10,256. https://doi.org/10.1002/2016GL070260

Silva, M.V., Paris, A., Calmant, S., Cândido, L.A., Silva, J.S. da, 2018. Relationships between Pacific and Atlantic ocean sea surface temperatures and water levels from satellite altimetry data in the Amazon rivers. Brazilian Journal of Water Resources 23. https://doi.org/10.1590/2318-0331.231820170148

Silva, T.S.F., Melack, J.M., Novo, E.M.L.M., 2013. Responses of aquatic macrophyte cover and productivity to flooding variability on the Amazon floodplain. Glob. Chang. Biol. 19, 3379-3389. https://doi.org/10.1111/gcb.12308

Sippel, S.J., Hamilton, S.K., Melack, J.M., 1992. Inundation area and morphometry of lakes on the Amazon River floodplain, Brazil. Arch. Hydrobiol 123, 385–400.

Sippel, S.J., Hamilton, S.K., Melack, J.M., Novo, E.M.M., 1998. Passive microwave observations of inundation area and the area/stage relation in the amazon river floodplain. Int. J. Remote Sens. 19, 3055–3074. https://doi.org/10.1080/014311698214181

Siqueira, V.A., Paiva, R.C.D., Fleischmann, A.S., Fan, F.M., Ruhoff, A.L., Pontes, P.R.M., Paris, A., Calmant, S., Collischonn, W., 2018. Toward continental hydrologic–hydrodynamic modeling in South America. Hydrol. Earth Syst. Sci. 22, 4815–4842. https://doi.org/10.5194/hess-22-4815-2018

Sorribas, M.V., Paiva, R.C.D., Melack, J.M., Bravo, J.M., Jones, C., Carvalho, L., Beighley, E., Forsberg, B., Costa, M.H., 2016. Projections of climate change effects on discharge and inundation in the Amazon basin. Clim. Change 136, 555–570. https://doi.org/10.1007/s10584-016-1640-2

Souza, C.M., Kirchhoff, F.T., Oliveira, B.C., Ribeiro, J.G., Sales, M.H., 2019. Long-term annual surface water change in the Brazilian Amazon Biome: Potential links with deforestation, infrastructure development and climate change. Water (Switzerland) 11, 566. https://doi.org/10.3390/w11030566

Staver, A.C., Archibald, S., Levin, S.A., 2011. The Global Extent and Determinants of Savanna and Forest as Alternative Biome States. Science (80-.). 334, 230–232. https://doi.org/10.1126/science.1210465

Taylor, C.M., Prigent, C., Dadson, S.J., 2018. Mesoscale rainfall patterns observed around

wetlands in sub-Saharan Africa. Q. J. R. Meteorol. Soc. 144, 2118–2132. https://doi.org/10.1002/qj.3311

Towner, J., Cloke, H.L., Zsoter, E., Flamig, Z., Hoch, J.M., Bazo, J., Coughlan de Perez, E., Stephens, E.M., 2019. Assessing the performance of global hydrological models for capturing peak river flows in the Amazon basin. Hydrol. Earth Syst. Sci. 23, 3057–3080. https://doi.org/10.5194/hess-23-3057-2019

Trigg, M.A., Birch, C.E., Neal, J.C., Bates, P.D., Smith, A., Sampson, C.C., Yamazaki, D., Hirabayashi, Y., Pappenberger, F., Dutra, E., Ward, P.J., Winsemius, H.C., Salamon, P., Dottori, F., Rudari, R., Kappes, M.S., Simpson, A.L., Hadzilacos, G., Fewtrell, T.J., 2016. The credibility challenge for global fluvial flood risk analysis. Environ. Res. Lett. 11, 094014. https://doi.org/10.1088/1748-9326/11/9/094014

Trigg, M.A., Wilson, M.D., Bates, P.D., Horritt, M.S., Alsdorf, D.E., Forsberg, B.R., Vega, M.C., 2009. Amazon flood wave hydraulics. J. Hydrol. 374, 92–105. https://doi.org/10.1016/j.jhydrol.2009.06.004

Ward, N.D., Bianchi, T.S., Medeiros, P.M., Seidel, M., Richey, J.E., Keil, R.G., Sawakuchi, H.O., 2017. Where Carbon Goes When Water Flows: Carbon Cycling across the Aquatic Continuum. Front. Mar. Sci. 4, 1–27. https://doi.org/10.3389/fmars.2017.00007

Wilson, M.D., Bates, P., Alsdorf, D., Forsberg, B., Horritt, M., Melack, J., Frappart, F., Famiglietti, J., 2007. Modeling large-scale inundation of Amazonian seasonally flooded wetlands. Geophys. Res. Lett. 34, 4–9. https://doi.org/10.1029/2007GL030156

Wongchuig, S.C., Paiva, R.C.D. de, Espinoza, J.C., Collischonn, W., 2017. Multi-decadal

Hydrological Retrospective: Case study of Amazon floods and droughts. J. Hydrol. 549, 667–684. https://doi.org/10.1016/j.jhydrol.2017.04.019

Wongchuig, S.C., de Paiva, R.C.D., Siqueira, V., Collischonn, W., 2019. Hydrological reanalysis across the 20th century: A case study of the Amazon Basin. J. Hydrol. 570, 755–773. https://doi.org/10.1016/j.jhydrol.2019.01.025

Wongchuig, S.C., Paiva, R.C.D., Biancamaria, S., Collischonn, W., 2020. Assimilation of future SWOT-based river elevations, surface extent observations and discharge estimations into uncertain global hydrological models. J. Hydrol. 590, 125473. https://doi.org/10.1016/j.jhydrol.2020.125473

Wu, J., Lakshmi, V., Wang, D., Lin, P., Pan, M., Cai, X., Wood, E.F., Zeng, Z., 2020. The Reliability of Global Remote Sensing Evapotranspiration Products over Amazon. Remote Sens. 12, 2211. https://doi.org/10.3390/rs12142211

Yamazaki, D., Ikeshima, D., Tawatari, R., Yamaguchi, T., O'Loughlin, F., Neal, J.C., Sampson, C.C., Kanae, S., Bates, P.D., 2017. A high-accuracy map of global terrain elevations. Geophys. Res. Lett. https://doi.org/10.1002/2017GL072874

Yamazaki, D., Kanae, S., Kim, H., Oki, T., 2011. A physically based description of floodplain inundation dynamics in a global river routing model. Water Resour. Res. 47, 1–21. https://doi.org/10.1029/2010WR009726

Yamazaki, D., Sato, T., Kanae, S., Hirabayashi, Y., Bates, P.D., 2014. Regional flood dynamics in a bifurcating mega delta simulated in a global river model. Geophys. Res. Lett. 41, 3127–3135. https://doi.org/10.1002/2014GL059744

Yamazaki, D., Trigg, M.A., Ikeshima, D., 2015. Development of a global ~90m water body map using multi-temporal Landsat images. Remote Sens. Environ. 171, 337–351. https://doi.org/10.1016/j.rse.2015.10.014

Zhang, Z., Poulter, B., Fluet-Chouinard, E., Jensen, K., McDonald, K., Hugelius, G., Gumbricht, T., Carroll, M., Prigent, C., Bartsch, A., 2020. Development and evaluation of the global Wetland Area and Dynamics for Methane Modeling dataset (WAD2M). Earth Syst. Sci. Data in review, 1–50. https://doi.org/10.5194/essd-2020-262

Zhou, X., Prigent, C., Yamazaki, D., 2021. Toward improved comparisons between land-surface-water-area estimates from a global river model and satellite observations. Water Resour. Res. 57, e2020WR029256. https://doi.org/10.1029/2020WR029256

Zubieta, R., Getirana, A., Espinoza, J.C., Lavado, W., 2015. Impacts of satellite-based precipitation datasets on rainfall-runoff modeling of the Western Amazon basin of Peru and Ecuador. J. Hydrol. 528, 599–612. https://doi.org/10.1016/j.jhydrol.2015.06.064

Zubieta, R., Getirana, A., Espinoza, J.C., Lavado-Casimiro, W., Aragon, L., 2017. Hydrological modeling of the Peruvian-Ecuadorian Amazon Basin using GPM-IMERG satellite-based precipitation dataset. Hydrol. Earth Syst. Sci. 21, 3543–3555. https://doi.org/10.5194/hess-21-3543-2017

Zubieta, R., Saavedra, M., Espinoza, J.C., Ronchail, J., Sulca, J., Drapeau, G., Martin-Vide, J., 2019. Assessing precipitation concentration in the Amazon basin from different satellite-based data sets. Int. J. Climatol. 39, 3171–3187. https://doi.org/10.1002/joc.6009

Supplementary Material

Table S1. List of additional studies that mapped inundation in the Amazon, which were not included in the article analysis because of redundancy with the used datasets, or data unavailability.

	Reference	Dataset name / Type	Spatial. resolution	Temporal resolution	Time period	Region	Type of inundation captured
1	Aires et al. (2013)	GIEMS + downscaling with SAR	500 m	Monthly	1993-2007	Central Amazon	All
2	Belger et al. (2011)	Radarsat-1 / C-band SAR	25 m	Irregular	2004-2005	Cuini and Itu (Negro basin)	All
3	Bonnet et al. (2008)	Hydrological model		Daily	1997-2003	Curuai	All
4	Canisius et al., 2019)	Radarsat-2 / C-band SAR	2.5-2.6 m	Irregular	2014-2016	Lower Amazon river	All
5	Fleischmann et al. (2020)	MGB / Hydrological-hydraulic model	4 km	Daily	1999-2015	Negro River basin	All
6	Frappart et al. (2005)	JERS-1 / L-band SAR	90 m	Static (high and low water)	1995-1996	Negro River basin	All

7	Getirana et al. (2012)	HYMAP / Hydrological model		Daily	1986–2006	Negro River basin	All
8	Guimberteau et al. (2012)	ORCHIDEE / Hydrological model	0.5 degrees	Daily	1980–2000	Basin	All
9	Hawes et al. (2012)	ALOS-PALSAR / L-band SAR	100 m	Irregular	2006-2009	Juruá floodplain	All
10	Hoch et al. (2017)	PCR-GLOBWB / Hydraulic model	30 arcmin	Daily	1985-1990	Central Amazon	All
11	Langerwisch et al. (2013)	LPJmL / Hydrological model	0.5 degrees	Monthly	1961-1990	Basin	All
12	Lauerwald et al. (2017)	ORCHIDEE-ORCHILEAK / Land surface model	0.5 degrees	Daily	1980–2000	Basin	All
13	Lesack and Melack (1995)	In situ data	-	-	-	Lake Calado	All
14	Li et al. (2020)	Landsat (Mapbiomas)	30 m	Annual	1985-2019	Madeira river close to Santo Antônio and Jirau dams	All
15	Luo et al. (2017)	MOSART / Hydraulic model	-	-	-	Basin	All
16	Martinez and Le Toan (2007)	JERS-1 / SAR	25 m	Irregular (21 images)	1993-1997	Curuai	All
17	Miguez-Macho and Fan (2012)	LEAF-Hydro-Flood / Hydrological-hydraulic model	~2 km	Daily	2000–2010	Basin	All

18	Meyer Oliveira et al. (2020)	ALOS-PALSAR / L-band SAR	100 m	Irregular	2006-2010	Purus River basin	All
19	Nardi et al. (2019)	GFPLAIN250m / geomorphic approach	250 m	Static	2002 (SRTM mission)	Basin	Floodplains
20	Paiva et al. (2013)	MGB / Hydrological-hydraulic model	500 m	Daily	1998-2010	Basin	All
21	Ringeval et al. (2012)	TOPMODEL - LSM / Hydrological model	1 degree	Monthly	1993–2004	Basin	All
22	Ringeval et al. (2014)	PCR-GLOBWB / Hydrological model	0.5 degrees	Daily	1979 - 2009	Basin	All
23	Rodriguez-Alvarez et al. (2019)	CYGNSS / GNSS-R	500 m - 7 km	Daily-14 days	2017	Pacaya-Samiria	All
24	Rosenqvist et al. (2002)	JERS-1 / L-band SAR	100 m	Irregular	1996-1997	Jaú river basin	All
25	Silva et al. (2013)	Radarsat-1 / C-band SAR	25 m	Irregular	2003 - 2005	Amazon river (Juruti - Monte alegre)	All
26	Sippel et al. (1992)	RADAMBRASIL / Side-looking Airborne Radar	0.25 degrees	Monthly	1979-1987	Amazon river in Brazil	All
27	Souza et al. (2019)	Landsat	30 m	Annual	1985-2017	Brazilian Amazon	Open water
28	Trigg et al. (2009)	LISFLOOD-FP and HEC-RAS / Hydraulic models	180 m / irregular	Daily	1995-1997	Solimões River (Itapeua - Manaus)	All
29	Wilson et al. (2007)	LISFLOOD-FP / Hydraulic model	270 m	Daily	1995-1997	Solimões River (Itapeua - Manaus)	All
30	Fassoni-Andrade et al., 2019	MODIS	250 m	8-Days	2003-2017	Central Amazon	Open water

1746

1747 Table S2. Main characteristics of the assessed wetlands.

	Name	Location	Characteristics
1	Curuai floodplain	Lower Amazon River	Shallow lakes with high suspended sediment concentrations
2	Janauacá floodplain	Middle Amazon River	Ria lake and "várzea" environments (white-water floodplains)
3	Uatumã floodplain	300-km reach between Balbina dam and the confluence with the Amazon River	Black-water floodplain
4	Mamirauá Reserve	Confluence between Solimões and Japurá rivers	Mosaic of chavascal, herbaceous, and low and high várzea vegetation
5	Purus floodplain	Purus River	Large floodplain to river width ratio
6	Pacaya-Samiria wetlands	Upper Solimões River	Flooded forests, palm swamps and peatlands
7	Llanos de Moxos floodable savannas	Upper Madeira River basin	Interfluvial areas among Beni, Mamoré and Madre de Dios rivers
8	Negro savannas	Negro-Branco interfluvial area	Regional neotectonic depressions
9	Roraima savannas	Smaller river floodplains interspersed with areas subject to flooding by local rainfall in the upper Branco River basin	Poorly drained interfluvial savannas

1748

1749 Table S3. Comparison metrics - Pearson correlation (R) and normalized root mean square error (nRMSD) for time
1750 series, and Fit metric for the spatial analysis of maximum observed inundation area for all datasets against the

subregional estimates for individual wetland complexes: Curuai (Arnesen et al., 2013), Uatumã (Resende et al., 2019), Janauacá (Pinel et al., 2019), Mamirauá (Ferreira-Ferreira et al., 2015), Pacaya-Samiria (Jensen et al., 2020), Llanos de Moxos (Ovando et al., 2016) and Lower Amazon (Park et al., 2019). Four additional subregional datasets were compared to the local ones mentioned above: Curuai LISFLOOD-FP model (Rudorff et al., 2014), Janauacá hydrological model (Bonnet et al., 2017), Janauacá TELEMAC-2D model (Pinel et al., 2019), and Llanos de Moxos ALOS-PALSAR (Ovando et al., 2016). The Fit metric was applied by converting all maps to 1 km, considering a pixel with inundation fraction higher than 50% as inundated.

	Dataset	-	Curuai			Uatumã	Janauacá			Mamirauá	Pacaya-Samiria			Llanos de Moxos			Lower Amazon
	-	Period	2006-2010			2006-2011	2007-2011			2007-2010	2014-2018			2001-2014			2000-2020
			R	nRMSD	Fit	Fit	R	nRMSD	Fit	Fit	R	nRMSD	Fit	R	nRMSD	Fit	Fit
Other subregional datasets	Curuai-Model	1994-2015	0.82	12%	0.86	-	-	-	-	-	-	-	-	-	-	-	-
	Janauacá-Bonnet	2006-2019	-	-	-	-	0.75	25%	0.49	-	-	-	-	-	-	-	-
	Janauacá-Pinel	2006-2015	-	-	-	-	0.57	17%	0.82	-	-	-	-	-	-	-	-
	Llanos de Moxos - ALOS	2006-2010	-	-	-	-	-	-	-	-	-	-	-	0.52	99%	0.33	-
Multiple datasets at coarse resolution	GIEMS-2	1992-2015	0.96	21%	-	-	0.78	157%	-	-	0.88	68%	-	0.91	85%	-	-
	SWAMPS	2000-2020	0.91	2%	-	-	0.8	38%	-	-	0.52	74%	-	0.92	171%	-	-
	WAD2M	2000-2018	0.9	82%	-	-	0.79	63%	-	-	0.46	2%	-	0.9	123%	-	-
Multiple datasets at high	GIEMS-D3	1993-2007	-	-	0.92	0.61	-	-	0.80	0.81	-	-	0.14	-	-	0.44	0.45
	CIFOR	2011	-	-	0.91	0.39	-	-	0.24	0.33	-	-	0.55	-	-	0.30	0.69

resolution	ESA-CCI	1992-2015	-	-	0.76	0.40	-	-	0.40	0.70	-	-	0.36	-	-	0.14	0.69
	GIEMS-D15	1993-2004	-	-	0.92	0.58	-	-	0.68	0.59	-	-	0.51	-	-	0.38	0.46
	GLWD	1992-2004	-	-	0.88	0.45	-	-	0.79	0.93	-	-	0.63	-	-	0.08	0.51
	SWAF-HR	2010-2019	-	-	0.95	0.64	-	-	0.63	0.71	0.66	73%	0.22	0.75	213%	0.39	0.57
Hydro-logical models	THMB	1961-2013	0.72	62%	-	-	0.73	73%	-	-	-	-	-	0.54	7%	-	-
	CaMa-Flood	1980-2014	0.80	11%	0.97	0.73	0.68	111%	0.88	0.83	-	-	0.49	0.82	218%	0.28	0.58
	MGB	1980-2014	0.83	7%	0.96	0.58	0.64	293%	0.82	0.93	-	-	0.52	0.91	26%	0.19	0.52
Optical sensors	G3WBM	1990-2010	-	-	0.64	0.29	-	-	0.19	0.14	-	-	0.03	-	-	0.04	0.59
	GLAD	1999-2018	-	-	0.84	0.39	-	-	0.30	0.20	-	-	0.04	-	-	0.16	0.78
	GSWO	1984-2019	-	-	0.75	0.31	-	-	0.21	0.17	-	-	0.04	-	-	0.09	0.68
SAR	Hess	1995-1996	-	-	0.96	0.47	-	-	0.28	0.98	-	-	0.48	-	-	0.47	0.69
	Chapman	2006-2011	-	-	0.65	0.27	-	-	0.22	0.68	-	-	0.28	-	-	0.24	0.50
	Rosenqvist	2014-2018	-	-	0.59	0.34	-	-	0.59	0.98	-	-	0.64	-	-	0.19	0.48

Table S4. Long-term minimum inundation areas (km²) for 11 wetland complexes (up to three datasets per complex) and the 18 basin-scale datasets. The local-scale values refer to the following datasets, in this order (comma-separated values relate to areas with more than one dataset available) : Curuai - ALOS (Arnesen et al., 2013) and LISFLOOD-FP model (Rudorff et al., 2014); Uatumã - ALOS (Resende et al., 2019); Janauacá - ALOS (Pinel et al., 2019), hydrologic model (Bonnet et al., 2017) and TELEMAC-2D model (Pinel et al., 2019); Mamirauá - ALOS (Ferreira-Ferreira et al., 2015); Pacaya-Samiria - ALOS-2 PALSAR-2 (Jensen et al., 2020); Llanos de Moxos - MODIS (Ovando et al., 2016) and ALOS (Ovando et al., 2016); and lower Amazon - MODIS (Park et al., 2019). Average, standard deviation (S.D.) and coefficient of variation (CV) are presented for each area in the last row.

	Dataset	Curuai	Uatumã	Janauacá	Mamirauá	Pacaya-Samiria	Llanos de Moxos	Lower Amazon	Amazon mainstem	Purus	Roraima savannas	Negro savannas
	Local	1690, 1278	-	108, 38, 18	715	3824	1014, 3962	17797				
Multiple datasets at coarse resolution	GIEMS-2	995	263	183	1117	1578	500	19717	26807	349	0	0
	SWAMPS	2840	479	197	790	4433	24622	38345	53256	3492	309	6375
	WAD2M	403	97	97	633	20421	31713	14728	29932	4240	258	10443
Multiple datasets at high resolution	GIEMS-D3	2712	861	151	1115	2731	8375	33253	44853	2696	383	146
	CIFOR	-	-	-	-	-	-	-	-	-	-	-
	ESA-CCI	-	-	-	-	-	-	-	-	-	-	-
	GIEMS-D15	3942	1265	116	1077	3409	15074	44277	59066	3401	2966	2622
	GLWD	-	-	-	-	-	-	-	-	-	-	-
	SWAF-HR	1502	544	69	469	215	8304	20944	30242	784	0	3
Hydrological model	THMB	487	38	1	266	5349	7172	6708	18099	5596	383	195
	CaMa-Flood	2741	861	184	1135	8269	17776	31569	45848	4128	1001	672
	MGB	3005	212	0	587	6101	4508	21333	32073	1769	226	35
Optical sensors	G3WBM	-	-	-	-	-	-	-	-	-	-	-
	GLAD	474	77	8	288	514	1513	6243	9857	335	13	20
	GSWO	736	345	10	314	401	2934	11908	16428	735	117	2
Synthetic Aperture Radar	Hess	2770	584	106	1756	32107	56337	28981	54493	7061	1217	6084
	Chapman	1894	385	68	866	6775	10090	18413	28539	2951	1025	2843
	Rosenqvist	1514	313	49	422	1077	4566	13413	19512	575	60	5
	Average	1858	452	89	774	6670	13820	22131	33500	2722	568	2103
	S.D.	1148	350	71	430	8978	15190	11637	15551	2094	801	3285
	CV	0.62	0.77	0.80	0.56	1.35	1.10	0.53	0.46	0.77	1.41	1.56

1767

1768

1769

1770

1771

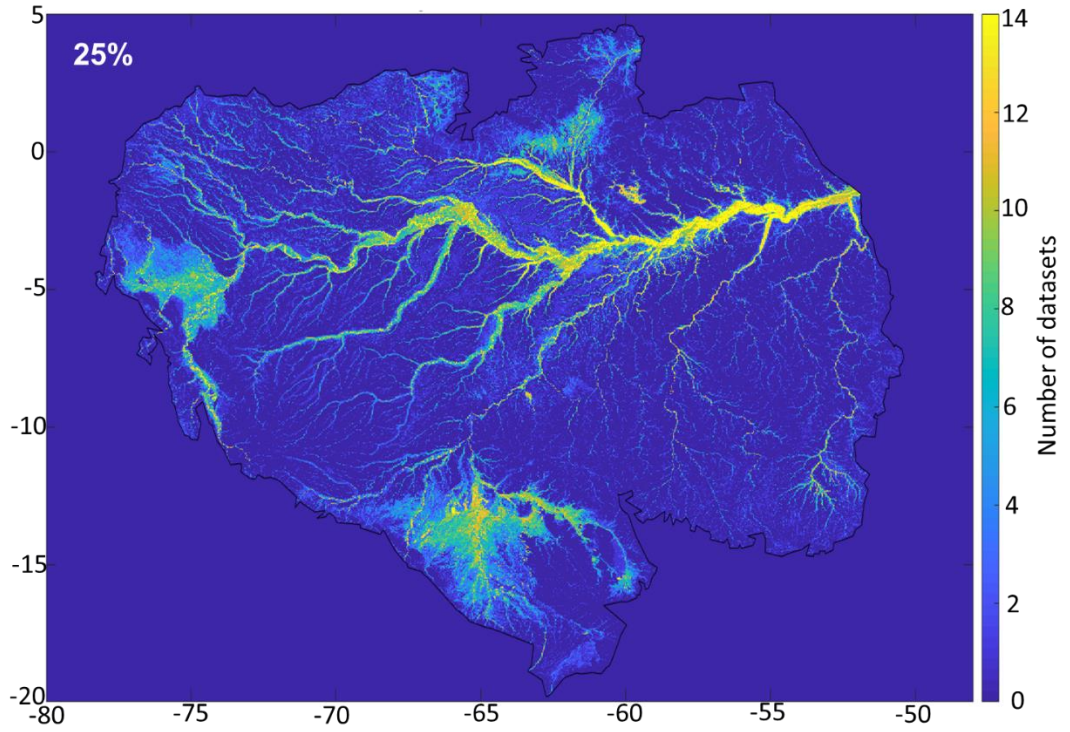

1772

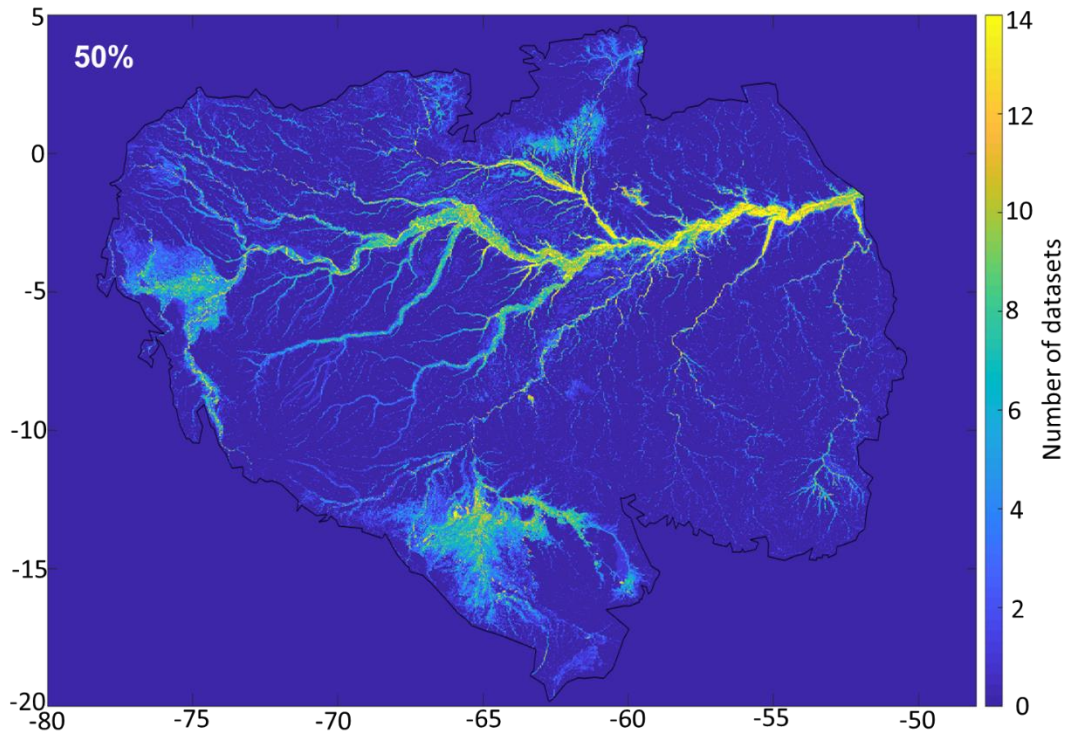

1773

1774 Figure S1. Sensitivity of the fraction used to define a flooded 1km pixel (25% and 50%).

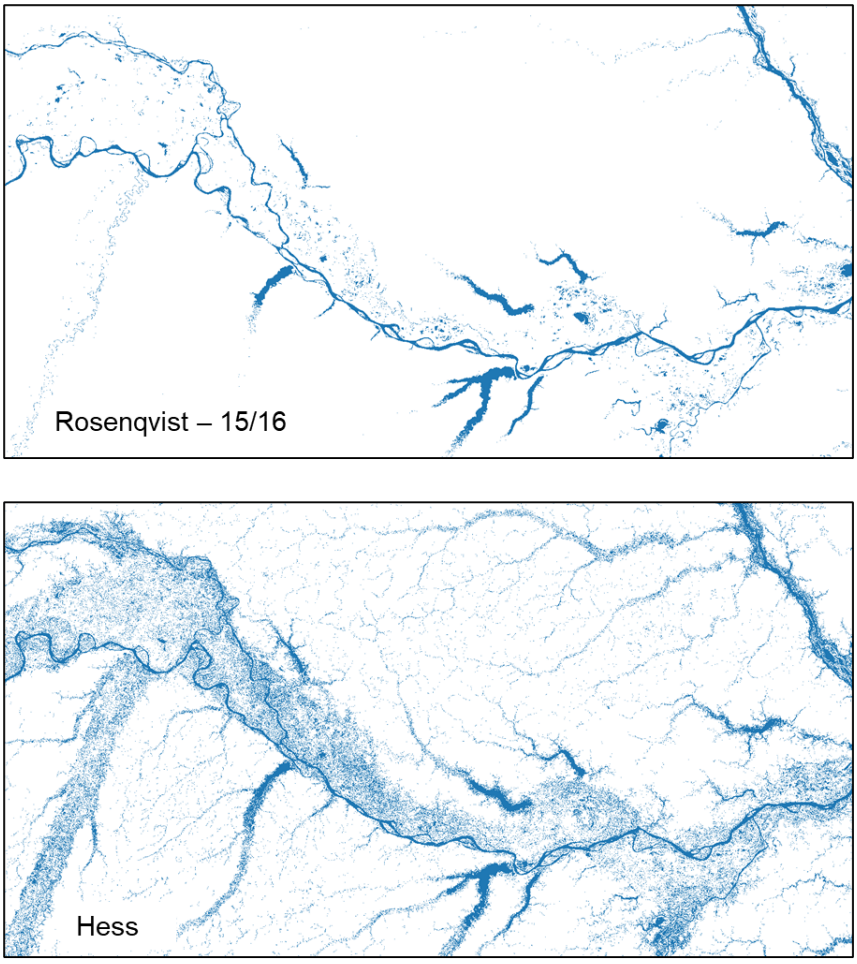

Figure S2. Minimum inundation extent for the central Amazon River, as estimated by the Rosenqvist (years 2015-2016) and Hess (1995) datasets.

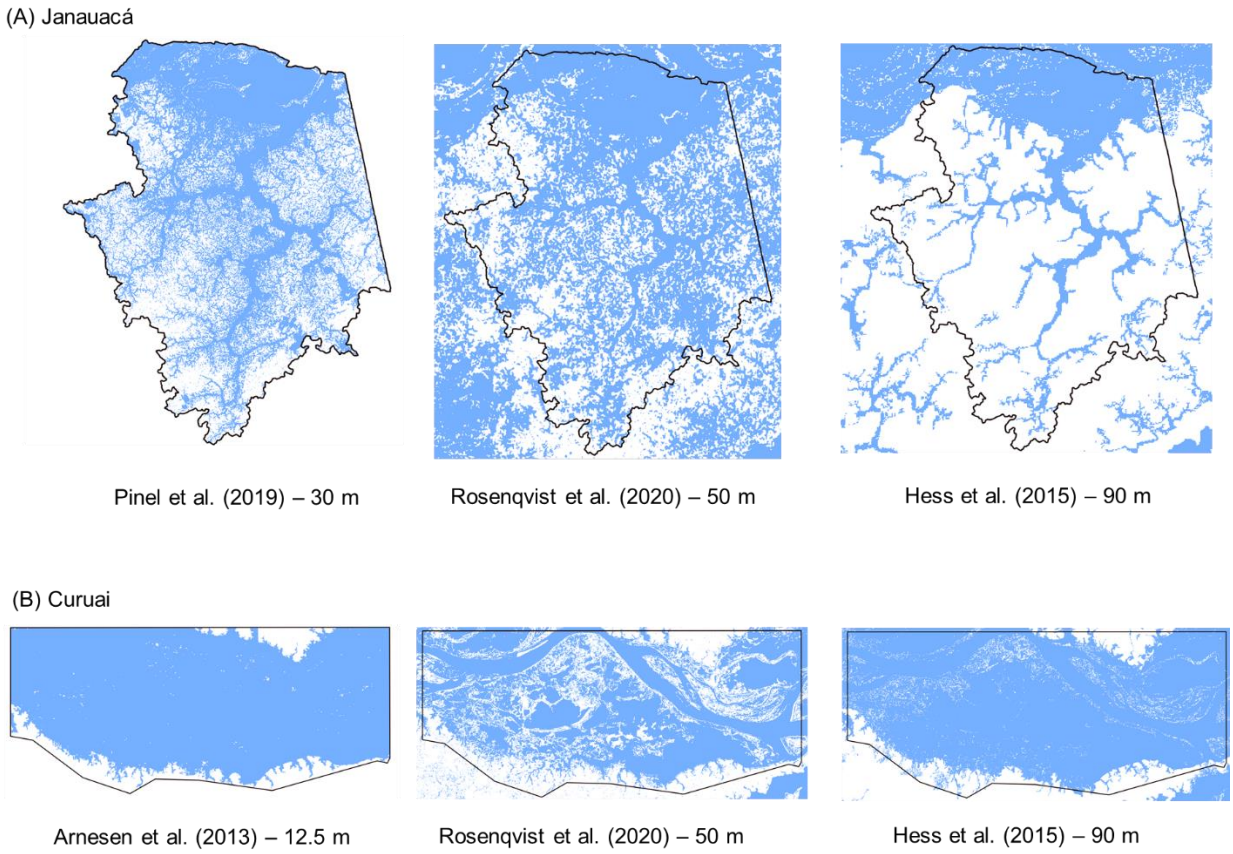

Figure S3. Comparison between the long-term maximum inundation for subregional validation locations (Pinel and Arnesen datasets) as well as the Rosenqvist and Hess datasets for the (a) Janauacá and (b) Curuai areas. The polygons refer to the area used to extract the values presented in Tables 3, S3 and S4. The spatial resolution of each dataset is noted.

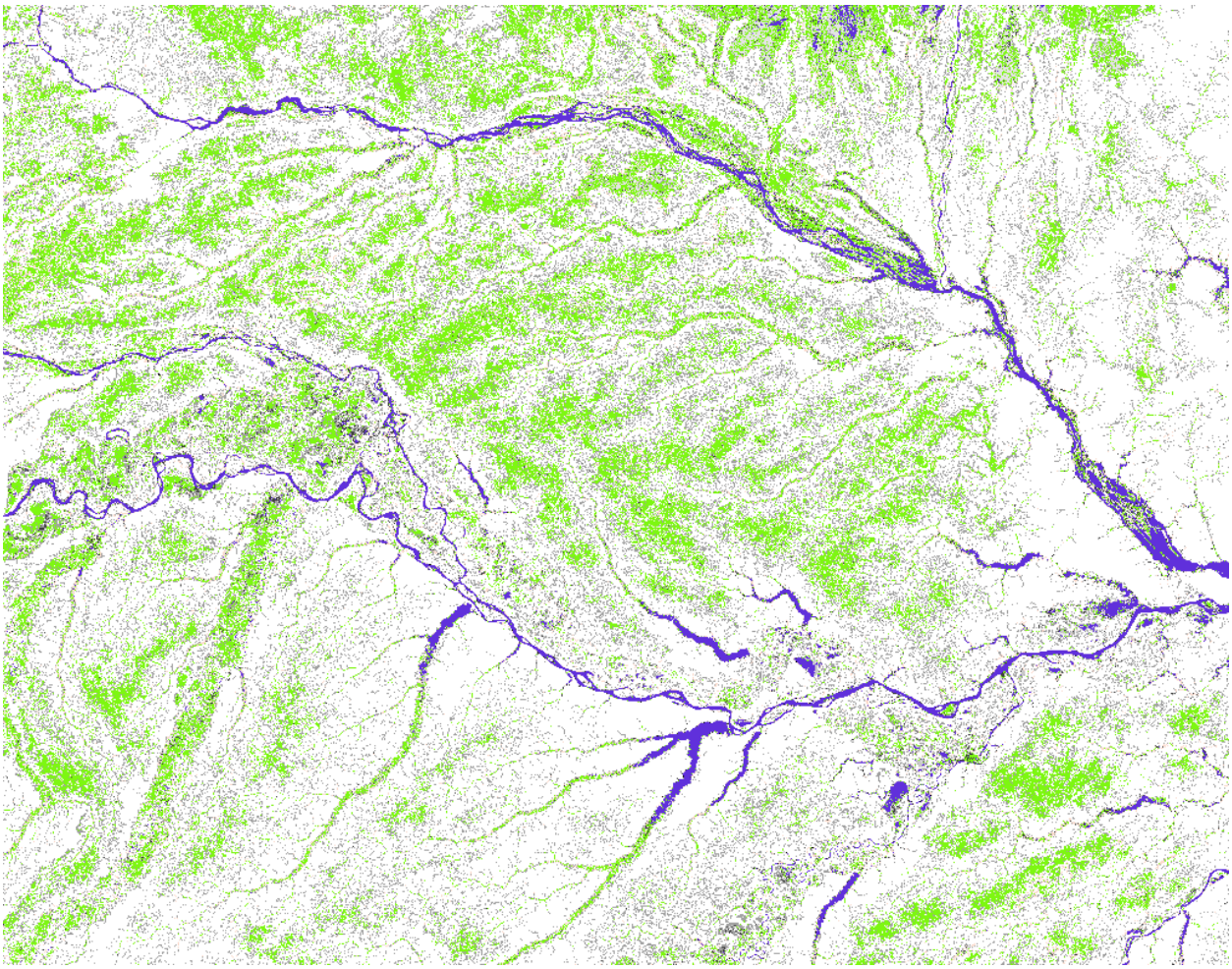

Figure S4. Estimation of wetland areas by Gumbricht et al. (2017) across the central Amazon River basin. Green pixels relate to the "swamps (incl. bogs)" category, which is defined as "Wet all year around, but not necessarily inundated."

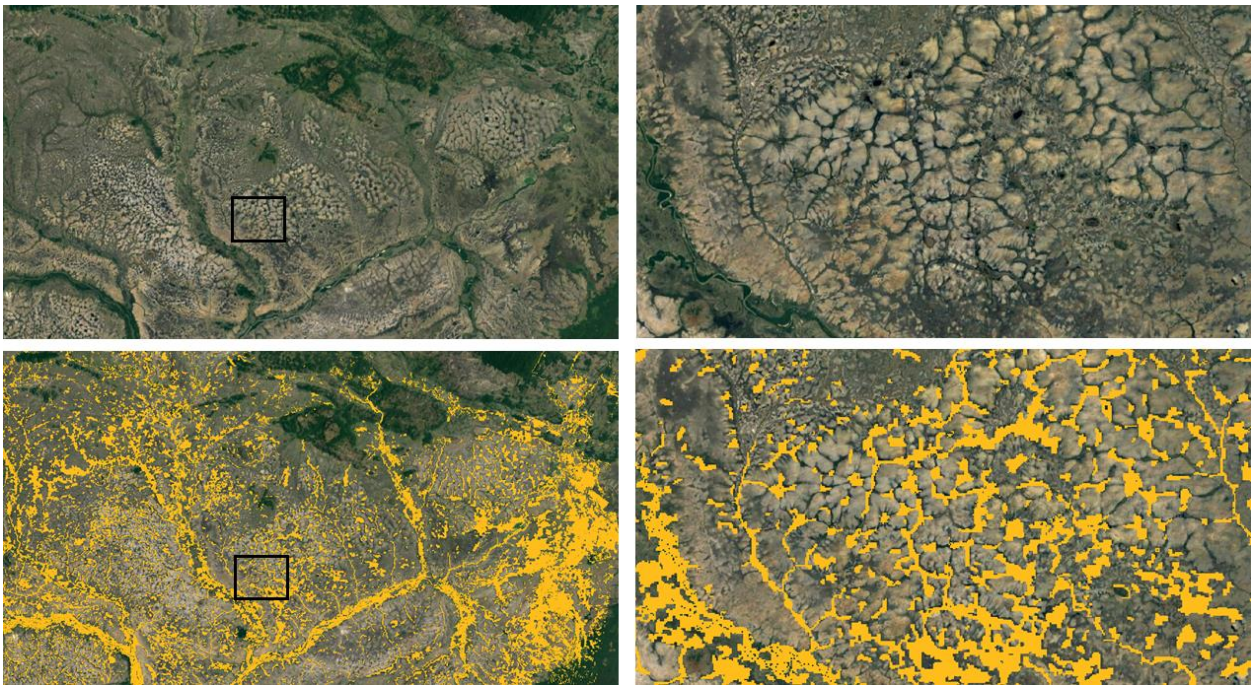

Fig S5. Roraima wetlands. Above: Google Earth imagery. Below: Hess SAR classification of floodable areas (at large scale in the left, and detailed scale in the right), displayed as orange areas.

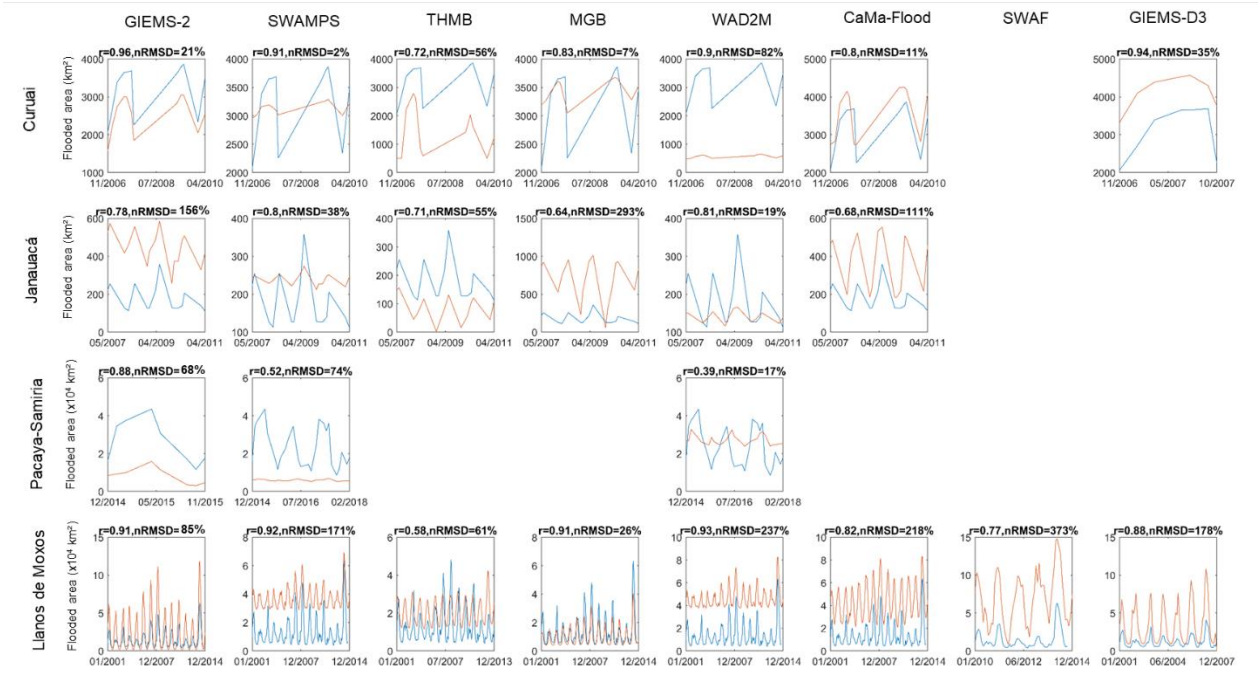

Fig S6. Inundation time series for the four wetlands with available datasets, and for the eight basin-scale dynamic datasets (GIEMS-2, SWAMPS, THMB, MGB, WAD2M, CaMa-Flood, SWAF-HR and GIEMS-D3). The subplots that are empty refer to areas where the basin-scale dataset time spans did not overlap with the subregional dataset ones. The subregional dataset is displayed in blue, and each of the basin-scale datasets in red.